PROTEIN ASSOCIATION IN LIVING CELLS USING FRET SPECTROMETRY: APPLICATION TO G-PROTEIN COUPLED RECEPTORS

by

Suparna Patowary

A Dissertation Submitted in

Partial Fulfillment of the

Requirements for the Degree of

Doctor of Philosophy

in Physics

at

The University of Wisconsin-Milwaukee

December 2013

ABSTRACT

PROTEIN ASSOCIATION IN LIVING CELLS USING FRET SPECTROMETRY: APPLICATION TO G-PROTEIN COUPLED RECEPTORS

by

Suparna Patowary

The University of Wisconsin-Milwaukee, 2013
Under the Supervision of Professor Valerică Raicu

Recent advancements in fluorescence microscopy coupled with newly developed fluorescent tags have transformed Fluorescence (Förster) Resonance Energy Transfer (FRET) into a powerful tool studying *in vivo* molecular interactions with improved spatial (angstrom) resolution. Though widely used to study protein-protein interactions, generalizing and testing the FRET theory for oligomeric complexes containing multiple donors and acceptors has only become possible in recent years. Therefore, many aspects of it are yet unexplored.

In this work, we tested the kinetic theory of FRET using linked fluorescent proteins located in the cytoplasm or at the plasma membrane. We used a novel method developed in our lab that combines an optical micro-spectroscope (OptiMiS) with a simple kinetic theory of FRET that relates the number and relative disposition of monomers within an oligomer to the measured FRET efficiency in terms of the pair-wise FRET efficiencies for an individual donor-acceptor pair in the oligomer. Using this

framework, we showed that the measured FRET efficiencies of obligate trimers and tetramers in living cells are correctly predicted by the kinetic theory of FRET.

The method was then used to study the oligomerization of G-protein coupled receptors (GPCRs), which are cell surface signaling proteins that constitute a large family of drug targets. The literature on GPCR homo-oligomerization encompasses conflicting views that range from interpretations that GPCRs must be monomeric, through comparatively newer proposals that they exist as dimers or higher-order oligomers, to suggestions that such quaternary structures are rather ephemeral or merely accidental and may serve no functional purpose. We used a novel FRET framework together with Optical Micro Spectroscopy (OptiMiS) technology and controlled expression of energy donor-tagged species of muscarinic M_3 acetylcholine receptor, a GPCR of interest, to show that M_3R exists as stable dimeric complexes at the plasma membrane, a large fraction of which interacts dynamically to form tetramers without the presence of trimers, pentamers, hexamers, etc. This was also supported by co-immunoprecipitation of receptors synthesized at distinct times. Based on these findings, we proposed a conceptual model that may reconcile the conflicting literature views on the quaternary structure of GPCRs.

Dedicated, sincerely

to

my parents and husband

Table of Contents

List of Figures

List of Tables

Acknowledgements

I take the privilege to express my deepest appreciation and thanks to everyone whose immense support and love made this dissertation a reality. Foremost, I would like to thank my advisor Prof. Valerică Raicu whose continued support, excellent guidance and advice along with being very protective and caring to me throughout my PhD helped in my multilateral growth. Though I started as an experimentalist in his group, his confidence on me helped me to overcome my fear of computer simulations. His trust and confidence in me let me experience and learn a very expensive and sophisticated instrument, OptiMiS, that boosted up my confidence and interest for technology development in optics. I would also like to express my deepest gratitude to him for his invaluable time and suggestions while writing dissertation.

I also want to express my sincere thanks to all my committee members, Prof. Julie A. Oliver, Prof. Marius Schmidt, Prof. Marija Gajdardziska-Josifovska and Prof. Dilano K. Saldin, for their valued time, suggestions, discussions and thoughtful criticisms that have helped me to improve my dissertation. Also, I take pleasure to thank Prof. Julie A. Oliver whose immense help, support, guidance and training made it possible for me to learn and execute all necessary biological research for this dissertation.

Our collaborators at the University of Glasgow, Prof. Graeme Milligan and Dr. Elisa Alvarez-Curto, the University of Toronto, Prof. James W. Wells and Dr. Luca F. Pisterzi, and Mayo Clinic, Arizona, Prof. Laurence J. Miller and Dr. Kaleeckal

Harikumar also contributed to this work by providing us with genetic constructs and cell lines as well as performing numerous biochemical assays. My sincere thanks go to them. Very importantly, I also thank the funding bodies, National Science Foundation (NSF) and Bradley Foundation, which provided major support towards the completion of this research.

I would also like to thank my senior colleague Dr. Michael Stoneman who helped me to learn, understand, and troubleshoot many facets of the experiments and their fine details. His time and help both in the experiments and dissertation writing was extremely valuable. I extend my sincere thanks to Dr. Gabriel Biener who never hesitated to spend time in helping me to understand Matlab, troubleshoot experiments, and make me learn about optical components and our system OptiMiS. It would have taken much time and effort for me to get exposed to the alignment and assembling of the optical instruments without his help. My special thanks and appreciation to my colleague and friend Jessica Holtz for her significant time in helping me for data analysis and volunteering in overnight and long run experiments.

Also I would like to thank all other current and former group members for their support and discussions while writing my dissertation that helped me to enhance my understanding towards this field of research. The positive attitudes and very cooperative behavior of everyone in the group provided an excellent healthy atmosphere for conducting research. My special thanks also go to our business specialist, Joan Baumgart

for her significant help with all the official and financial work, as well as her encouragement to me while writing my dissertation.

I am grateful to the faculty members in the Physics department at UW-Milwaukee with whom I took courses that helped me to strengthen the concepts in Physics and reshuffle many aspects of my background in physics. My great appreciations and thanks also go to our administrative staff, Steve Kennedy, Kate Valerius, Reba Sinha, Pamela Urban and Greg Baran for being very friendly and cooperative and also for their help wherever necessary.

Finally, my heartiest love, respect and thanks to my parents and siblings whose immense love, support, and confidence in me paved my way to successfully accomplish my goal. Lastly but most importantly, I would like to convey my deepest thanks to my husband Dr. Mukul Dubey who not only contributed to this dissertation with his suggestions in arranging and improving the text, making figures, and proofing the thesis, but also inspired and shared my final efforts despite the enormous pressures we were facing together.

Chapter 1 Overview of FRET theory and its practical application

Proteins are known to play a vital role in most biological processes inside a cell such as cell growth, gene expression, nutrient uptake, and intercellular communication (1). The specific activity of proteins and their particular cellular responses has long been a subject of intense discussions among researchers. The key aspects of protein functions include the understanding of protein sequence and structure, evolutionary history and conserved sequences, expression profile, post-translational modification, interaction with other proteins or proteins of their own type, and intracellular localization (1). Several techniques have been developed so far to study protein-protein interactions including high-throughput surface-based identification of interacting protein pairs (2) and *in vivo* protein interactions like co-immunoprecipitation, protein complementation assays (PCA) etc. These techniques, however, are limited in their capability of identifying specific protein interaction from among ~30,000 of proteins in a living cell (3). Techniques such as fluorescence spectroscopy and fluorescence imaging were found promising to investigate molecular association and protein-protein interactions in complex cellular environments due to the capability of tagging protein of interest with fluorescent markers (4-6). Fluorescence (Förster) resonance energy transfer (FRET) is one of the widely used methods that proved to be significantly useful in detecting molecular organization and protein-protein interaction both *in vivo* and *in vitro* (7-10). However, most of the FRET measurement techniques that use conventional fluorescence microscopy require sequential scans of emission wavelength, excitation wavelength, or both, making the measurements time consuming limiting their applicability to study protein dynamics (11-

13). A very promising method based on a spectrally resolved two-photon microscope (14) and a competent theory of FRET (12, 15) has recently been proposed that is proved to be successful in determination of protein complex size, configuration, and spatial distribution in single living cells (16-18). This approach can also open up potential pathways towards the understanding of dynamic cellular processes in living cells.

This thesis represents an effort of understanding the FRET theory coupled with the optical micro-spectroscopy (OptiMiS) as applied to multimeric complexes of fluorescent proteins, and use of the method to study the oligomerization of G-protein coupled receptors (GPCRs) in living cells. GPCRs are the largest group of membrane proteins that can be used as targets of many pharmaceutical drugs (19-22). As a first step, we used the OptiMiS developed in our lab and the theory proposed by V. Raicu (23) to validate FRET theory for multimeric complexes. Following the validation, we used this method to determine the quaternary organization of muscarinic acetylcholine receptor type 3, a GPCR of interest, responsible for various chronic diseases (24, 25). This chapter provides a brief overview on the historical development of FRET theory and its diverse application in a broad range of fields.

1.1 Energetic diagram representation of fluorescence and FRET

FRET, as the acronym stands for, is a phenomenon of non-radiative energy transfer between two molecules in close proximity (< 10 nm distance). The molecules involved in the energy transfer are usually fluorescent, though sometimes the energy is transferred from a fluorescent donor to a non-fluorescent acceptor (4, 26, 27). The unique advantage

of FRET is the capability to reveal the structure down to molecular scale (~ 10 nm) by overcoming the limit of optical resolution (~ 200 nm).

Most of the recent FRET experiments are designed to excite a donor by absorption of photons. Although the experimental details are relevant to how the donor is excited, the energy transfer rate is independent of it. Once the donor is in the excited state, it can lose its energy in three different ways: first, through emission of photons, second, via non-radiative decay and third, transferring energy non-radiatively to nearby fluorophores. The probability and the rate of de-excitation of the donor through any of the pathways depend on all the possible pathways through which the donor can emit its excitation energy to come to the ground state.

A schematic representation of light absorption and emission mechanism also known as Jablonski diagram was first given by A. Jablonski in 1935. Fig. 1.1 shows a classical Jablonski diagram illustrating FRET activity. S_{D0}, S_{D1}, and S_{D2} are the ground, first, and second electronic states of the donor and S_{A0}, S_{A1} are the ground state and the first excited states of acceptor respectively. The vibrational energy levels for each electronic state are represented by 0, 1, 2 etc. The first triplet state of the donor is represented by T_{D1}. The molecules can be in any of these vibrational energy states in an electronic energy level.

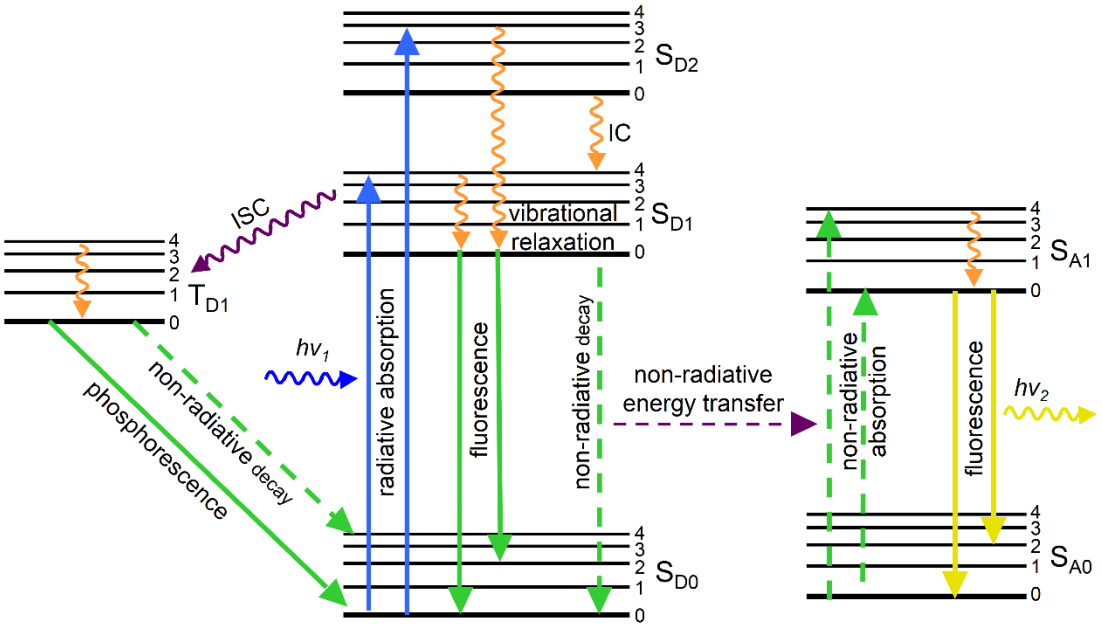

Figure 1.1: Jablonski diagram showing electronic transitions between energy levels. Incident light ($h\nu_1$) is shown by curly blue arrow. Black solid lines represent singlet (S_D for donor and S_A for acceptor) and triplet (T_D for donor) energy levels corresponding to donor molecule (D) and acceptor molecule (A). Absorption and emission transitions are shown by solid and dotted blue, green, and yellow lines. Curly orange and purple arrows show vibrational relaxations, internal conversion (IC) and intersystem crossing (ISC) respectively. The yellow curly arrow ($h\nu_2$) from acceptor (A) shows acceptor emission. FRET is shown by purple dotted arrow pointing from donor (D) to acceptor (A) as non-radiative energy transfer between donor and acceptor.

In most cases, the donor is excited from the lowest vibrational energy level of the ground state to the higher vibrational energy levels of S_{D1} or any higher energy states than S_{D1} by absorbing a photon. Depending on the energy separation between S_{D1} and the higher energy excited states, it can dissipate its energy through internal conversion (IC), or thermal relaxation to the thermally stable lowest vibrational energy level of S_{D1} within the time interval of 10^{-11} – 10^{-14} s. The donor molecules in lowest vibrational energy level of S_{D1} can lose its energy through various pathways, some of which are dependent on its molecular environment, e.g. proximity of the acceptors or quenchers and solvent interactions etc. The process of de-excitation of donor to the ground state through

emission of a photon is called fluorescence. The lifetime of an excited singlet state is 10^{-7} – 10^{-9} s and hence fluorescence can occur typically in 10^{-8} s. The donor molecule can also be de-excited to reach the ground state non-radiatively, converting all its energy into heat. Donors in their lowest excited singlet state (S_{D1}) can also undergo spin conversion process to the triplet state (T_{D1}) through the process known as intersystem crossing (ISC) that is less probable than the singlet-singlet process and can occur within the lifetime of fluorescence. Once the molecule is in the triplet state, it can undergo internal conversion (10^{-7}-10^{-9} s) to the lowest vibrational energy levels of triplet state. The reverse process ($T_{D1} \rightarrow S_{D1}$) is highly improbable since the energy difference between the lowest vibrational state of S_{D1} and the highest vibrational state of T_{D1} is larger than the internal conversion energy. The process of emission from T_{D1} to the ground state is called phosphorescence, which occur in the lifetime of the triplet state (10^{-4} – 10^{2} s). Donor molecule in the lowest vibrational energy state of T_{D1} can also undergo non-radiative de-excitation to the ground state. If another fluorophore (acceptor) molecule having excitation energy lower than the emission energy of the donor is in close proximity (< 10 nm) of the donor; the donor molecules can transfer its energy to nearby (acceptor) molecules through dipole-dipole coupling between the donor and the acceptor. In this process, the acceptor molecules get excited non-radiatively from the ground to the first excited state. Similar to the donor de-excitation process, the acceptor molecule de-excites to the lowest vibrational energy state of first excitation level via vibrational relaxation from where it can de-excite to the ground state by either photon emission or non-radiatively.

1.2 Elementary theory of FRET

1.2.1 Historical overview

Although the practical application of FRET occurred after Förster's quantum mechanical explanation of Resonance Energy Transfer (RET) introduced in 1946, the first experimental measurement of energy transfer between two molecules or atoms at a distance much greater than their radii was performed by Cario and Franck in 1922 (28). They observed emission from thallium atoms by exciting a mixture of mercury and thallium vapors at the excitation wavelength of mercury (253.6 nm), which was attributed to the excitation of the thallium atoms through energy transfer from the excited mercury atoms and was named as *"sensitized fluorescence"* (28). In 1928, Kallmann and London (29) proposed quantum mechanical theory to explain transfer of energy between interacting atoms at distance greater than their radii using second order perturbation calculations. They showed that the effective cross-section (q) of two interacting atoms is inversely proportional to the 2/3rd power of the difference in excitation energies (σ) between the two interacting atoms i.e., $q \propto \sigma^{-2/3}$ (28). Their theory was based on the assumption that the energy levels of interacting atoms were in resonance.

A classical model of energy transfer between interacting molecules in solution was first proposed by J. Perrin and F. Perrin, assuming the transition dipoles of the interacting molecules as Hertzian electric dipoles. They also assumed that, if the distance between two interacting molecules were sufficiently small, the energy transfer between the molecules can occur non-radiatively, which was termed as *"transfer d' activation"* (28). They concluded that the rate of energy transfer is proportional to $1/R^3$, R being the

distance between two interacting fluorophores, which is an order of magnitude higher than the experimentally observed distances between the fluorophores. The central assumption of Perrins' derivation, i.e. the condition for exact resonance between the two fluorophores, led to a large value of the distance between the fluorophores at which energy transfer may occur. Later, Förster in his work (30) showed that the resonance between the dipoles is not restricted to only one wavelength, because of the broadening of the energy levels in solution caused by the vibrational and collisional effects between the molecules. Following the principle of energy conservation between the states of energy transfer from a donor to an acceptor, the condition of resonance is limited to their overlapping spectra. Therefore, the probability of energy transfer between donor and acceptor depends on the overlap between the donor emission spectrum and acceptor excitation spectrum and thus is calculated by integrating the overlapping spectra of the donor's emission and the acceptor's absorption. Förster's theory agrees well with the measured distance between interacting molecules.

1.2.2 Perrins' classical model of energy transfer between two identical Hertzian dipoles

J. Perrin (31) gave the derivation of the interaction energy between two Hertzian dipoles based on the classical mechanics. F. Perrin extended his theory by developing a corresponding quantum mechanical approach (28, 32, 33).

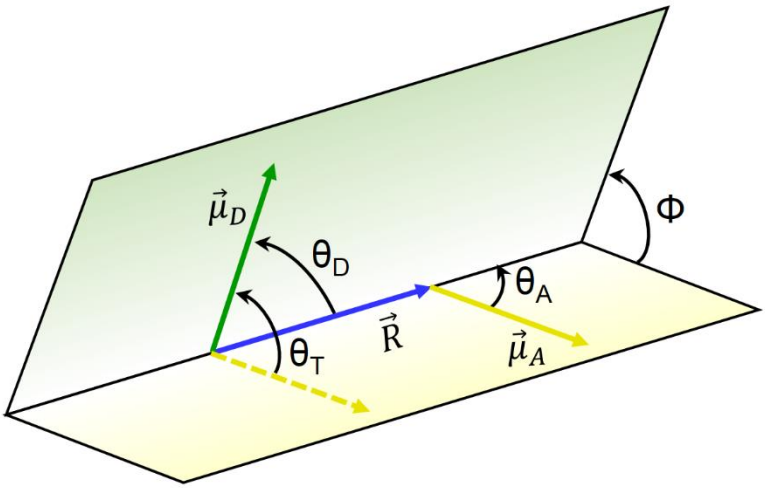

Figure 1.2: Parameterizing the orientations of donor and acceptor dipole moments. Dipole planes for donor and acceptor are shown in green and yellow making an angle Φ with each other. Green and yellow lines on the planes are dipole moments for donor and acceptor respectively; θ_D, θ_A are the angle between the separation vector $\hat{R}$ and dipole moment of D and A respectively and θ_T is the angle between dipole moment of D and A.

The classical model of J. Perrin considered two identical oscillating dipoles "Donor" (D) and "Acceptor" (A) with respective dipole moments $\vec{\mu}_D$ and $\vec{\mu}_A$, separated by a distance $\vec{R}$ as shown in Fig. 1.2. These correspond to the transition dipoles of the excited molecules. The electric field ($\vec{E}_D$) originating from the oscillating dipole 'D' in the near field zone can be written as:

$$\vec{E}_D = \frac{1}{n^2 R^3}\left[3\left(\vec{\mu}_D.\hat{R}\right)\hat{R} - \vec{\mu}_D\right] \tag{1.1}$$

where *n* is the refractive index of the medium. The interaction energy experienced by the dipole 'A' in the presence of the electric field $\vec{E}_D$ can thus be expressed as:

$$E_{int} = -\vec{\mu}_A . \vec{E}_D = \frac{1}{n^2 R^3}\left[(\vec{\mu}_D . \vec{\mu}_A) - 3(\vec{\mu}_D . \hat{R})(\vec{\mu}_A . \hat{R})\right] \quad (1.2)$$

For identical dipoles, $|\vec{\mu}_D| = |\vec{\mu}_A| = \mu$. Therefore, equation (1.2) can be written as:

$$E_{int} = \frac{\kappa \mu^2}{n^2 R^3} \quad (1.3)$$

where

$$\kappa = \left[(\hat{\mu}_D . \hat{\mu}_A) - 3(\hat{\mu}_D . \hat{R})(\hat{\mu}_A . \hat{R})\right] \quad (1.4)$$

is the orientation factor. Using Planck's 'old' quantum theory, equation (1.3) can be written as:

$$E_{int} = \frac{\kappa \mu^2}{n^2 R^3} = h\omega_{int} = \frac{\hbar}{\tau_{int}} \quad (1.5)$$

where, h is the Planck's constant, ω_{int} is the angular frequency corresponding to the interaction energy E_{int}, τ_{int} is the time period of the oscillating donor, and $\hbar = h/2$. Rearranging equation (1.5), the interaction time period can be expressed as:

$$\tau_{int} = \frac{\hbar n^2 R^3}{\kappa \mu^2} \quad (1.6)$$

For Hertzian oscillating dipole, the energy of the radiation and the radiation time constant can be written as (28, 34):

$$E_{rad} = \frac{\mu^2 \omega^3}{3c^3} \tag{1.7}$$

and

$$\tau_{rad} = \frac{3\hbar c^3}{\mu^2 \omega^3} \tag{1.8}$$

where ω is the frequency of the Hertzian donor oscillator and c is the speed of light. In order to calculate the distance R_0 between the oscillating dipoles at which the natural decay time of the oscillator is equal to the time of energy transfer i.e. $\tau_{rad} = \tau_{int}$ (28, 29), equations (1.6) and (1.8) give,

$$R_0^3 = \frac{3\kappa c^3}{n^2 \omega^3} = \frac{3\kappa}{n^2 (2\pi)^3} \lambda^3 \approx 0.01\lambda^3 \tag{1.9}$$

or, $R_0 = \frac{\lambda}{2\pi}$, using $c = \nu\lambda = \frac{\omega\lambda}{2\pi}$. At this distance between D and A, half of donor's energy that would have been emitted radiatively is transferred non-radiatively to the acceptor. This calculation of R_0 shows that the energy transfer from an oscillating donor to a stationary acceptor can take place at a distance comparable to the wavelength of the radiation (or light). For $\lambda = 600$ nm, the value of R_0 was found to be 120 nm which is an order of magnitude higher than the experimental value.

1.2.3 Förster's correction to Perrin's model

Förster pointed out that the large theoretical value of R_0 in Perrin's derivation was due to the assumption of exact resonance between the two interacting particles. In reality,

Förster stated, there exists an energy distribution for an ensemble of molecules in a solution, because of intramolecular and solvent interactions, which results in spectral broadening and should be accounted for carefully (26, 28). Because of this spectral broadening, the probability of exact resonance is very low since the emission spectra of the excited molecule and the absorption spectra of the unexcited molecule are different and have overlapping spectra only for a particular wavelength as shown in Fig 1.3 (a). Therefore, the condition of exact resonance will occur only for a very short period of time during the long time required for energy transfer (26).

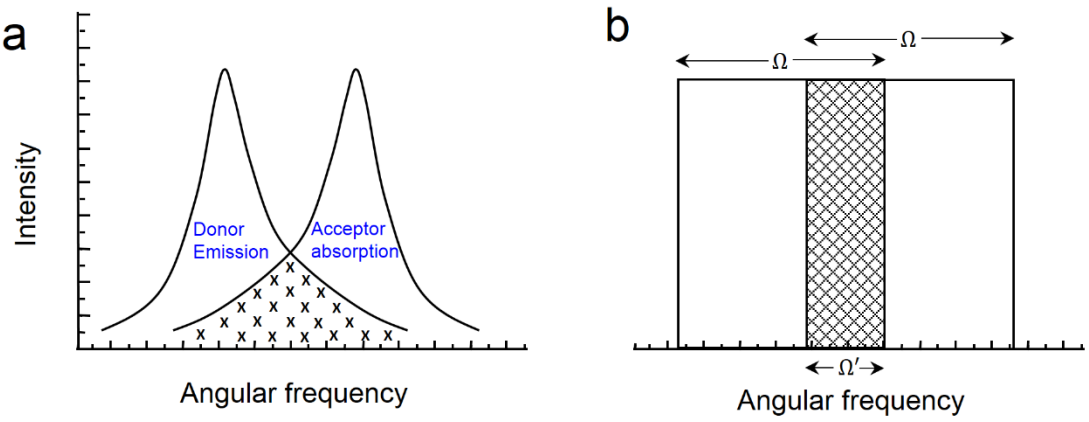

Figure 1.3: Spectral overlap between donor emission and acceptor absorption spectra. **(a)** Representative intensity vs. angular frequency plot for donor emission and acceptor absorption; hatched area in the plot shows overlapping spectra of donor and acceptor. **(b)** Areas under the spectral plot for donors and acceptors are represented by rectangles of angular frequency of width Ω; hatched area with angular frequency width Ω' shows the overlapping area corresponding to the overlapping area of **(a)**.

Förster calculated the time needed for energy transfer from D to A in terms of the probability of overlapping frequencies and probability of having simultaneously the same energies for the two fluorophores within the small interaction energy. Assuming same spectral width for both the fluorophores and considering Ω and Ω' to be the spectral

width and overlapping spectral width respectively (Fig 1.3 (b)) then the probability of spectral overlap of two fluorophores can be given as Ω'/Ω, while the probability of the bandwidth Ω falling within the narrow coupling bandwidth of $E_{int}/\hbar$, is given as $\frac{E_{int}}{\hbar\Omega}$. Hence, the simultaneous probability of occurrence of the above two independent events is $\frac{\Omega'}{\Omega}\frac{E_{int}}{\hbar\Omega}$ (35). Therefore the interaction energy is corrected to

$$E'_{int} = \left(\frac{\Omega'}{\Omega}\frac{E_{int}}{\hbar\Omega}\right)E_{int}. \tag{1.10}$$

Using equation (1.5) for E_{int}, Förster's correction to the dipole interaction time can be written as:

$$\tau'_{int} = \frac{\hbar^2 n^4 R^6}{\kappa^2 \mu^4}\frac{\Omega^2}{\Omega'}. \tag{1.11}$$

Hence, the distance at which the radiative energy is same as the non-radiative energy transfer, also termed as Förster distance, that is calculated using equation (1.8) and (1.11) as:

$$R_0^6 = \frac{3\kappa^2\mu^2 c^3}{\hbar n^4 \omega^3}\frac{\Omega'}{\Omega^2} = 9\left(\frac{\lambda}{2\pi}\right)^6 \frac{\kappa^2}{n^4}\frac{\Omega'}{\Omega^2}\frac{1}{\tau_{rad}} \tag{1.12}$$

giving $R_0 < \frac{0.1\lambda}{2\pi}$. For λ = 600 nm, R_0 ~ 10 nm. Equation (1.12) shows that Förster's interpretation of resonance in FRET along with the condition of spectral broadening considerably decreased the effective interaction distance between donor and acceptor. Förster also emphasized that even though the energy transfer via FRET occur by an

exchange of quanta, it is essentially a classical resonance effect (26). Förster later published the quantum mechanical derivation of R_0 and energy transfer rate using time-dependent probability of energy transfer (35), which is discussed in the next section.

1.2.4 Quantum mechanical treatment of FRET

Let us consider the energies of donor (D) and acceptor (A) in the ground and excited states are represented by E_D, E_A and E_D', E_A' respectively. The donor (D) is excited by absorption of a photon to the excited state of energy E_D' while acceptor is in its ground state, E_A. Due to FRET, the donor is de-excited to its ground state, E_D, by transferring its energy to the acceptor, which is brought to its first excited state, E_A'. Let the initial (before FRET) and final (after FRET) wave functions of the system be $\psi_{D'A}$ and $\psi_{DA'}$, respectively. If $\mathcal{H}_D$ and $\mathcal{H}_A$ are the unperturbed Hamiltonians of D and A, respectively, and E_{int} is their interaction energy, then the total Hamiltonian of the system can be expressed as:

$$\mathcal{H} = \mathcal{H}_D + \mathcal{H}_A + E_{int} \tag{1.13}$$

So far we know that the interaction between donor and acceptor via FRET is a very weak coupling; consequently, the interaction has negligible effect on their absorption and emission spectra, therefore, according to the time-dependent perturbation theory, the transition probability for a very large interaction time can be written as (36):

$$P(D'\,A \to D\,A') \simeq \lim_{t\to\infty} \iint \frac{1}{\hbar^2} \left|V_{D'A;DA'}\right|^2 \left|\frac{\sin\left(\frac{\Delta E t}{2\hbar}\right)}{\left(\frac{\Delta E t}{2\hbar}\right)}\right|^2 t^2 dE_D dE'_A$$
$$\simeq \iint \frac{t}{\hbar^2} \left|V_{D'A;DA'}\right|^2 \lim_{t\to\infty} \frac{\sin^2\left(\frac{\Delta E}{2\hbar} t\right)}{\left(\frac{\Delta E}{2\hbar}\right)^2 t} dE_D dE'_A \tag{1.14}$$

where

$$\Delta E = E'_A + E_D - E'_D - E_A \tag{1.15}$$

is the energy difference between the initial and the final state of the system. Using the definition of Dirac delta function $\lim_{t\to\infty} \frac{\sin^2 xt}{x^2 t} = \pi\delta(x)$ and $\delta(ax) = \delta(x)/a$, we can re-write equation (1.14) as:

$$P(D'\,A \to D\,A') = \frac{2\pi t}{\hbar} \iint \left|V_{D'A;DA'}\right|^2 \delta(\Delta E) dE_D dE'_A. \tag{1.16}$$

Since the energy lost by the donor due to de-excitation to the ground state is equal to the energy gained by the acceptor brought to its excited state, we can write

$$E = \frac{1}{2}[E'_D - E_D + E'_A - E_A)]. \tag{1.17}$$

Therefore, E'_A and E_D can be expressed as functions of E and ΔE.

Hence,

$$dE_D dE'_A = \frac{\partial(E, \Delta E)}{\partial(E_D, E'_A)} dE d(\Delta E) = \begin{vmatrix} \frac{\partial E}{\partial E_D} & \frac{\partial(\Delta E)}{\partial E_D} \\ \frac{\partial E}{\partial E'_A} & \frac{\partial(\Delta E)}{\partial E'_A} \end{vmatrix} dE d(\Delta E) \tag{1.18}$$

Using equations (1.15) and (1.17); the determinant in equation (1.18) becomes:

$$\begin{vmatrix} -\frac{1}{2} & -1 \\ \frac{1}{2} & -1 \end{vmatrix} = 1.$$

Therefore, equation (1.16) becomes:

$$\begin{aligned} P(D'\,A \to D\,A') &= \frac{2\pi t}{\hbar} \iint \left|V_{D'A;DA'}(E, \Delta E)\right|^2 \delta(\Delta E) dE d(\Delta E) \\ &= \frac{2\pi t}{\hbar} \int \left|V_{D'A;DA'}(E, 0)\right|^2 dE\,, \end{aligned} \tag{1.19}$$

where $V_{D'A;DA'}(E, 0) = V_{D'A;DA'}(E'_D, E_A;\ E_D, E'_A) = V_{D'A;DA'}(E'_D, E_A;\ E'_D - E, E_A + E)$

Let Φ_i and Φ'_i be the electronic wave functions and χ_i and χ'_i to be the vibrational wave functions of the fluorophores in their ground and excited states, respectively. Using the Born-Oppenheimer approximation, we can express the initial and final wave functions of the system in terms of electronic and vibrational components as:

$$\psi_{D'\,A}(E'_D, E_A) = \Phi'_D \Phi_A \chi'_D(E'_D) \chi_A(E_A) \tag{1.20}$$

$$\psi_{D\,A'}(E_D, E'_A) = \Phi_D \Phi'_A \chi_D(E'_D - E) \chi'_A(E_A + E) \tag{1.21}$$

Hence,

$$V_{D'A;DA'} = \langle \psi_{D\,A'}(E_D, E'_A)|E_{int}|\psi_{D'\,A}(E'_D, E_A)\rangle$$
$$= \langle \Phi_D \Phi'_A\,|E_{int}|\Phi'_D \Phi_A)\rangle\langle\chi_D(E'_D - E)|\chi'_D(E'_D)\rangle\langle\chi'_A(E_A + E)|\chi_A(E_A)\rangle \quad (1.22)$$
$$= WS_D(E'_D, E'_D - E)S_A(E_A, E_A + E)$$

where $W = \langle \Phi_D \Phi'_A\,|E_{int}|\Phi'_D \Phi_A)\rangle$ is the interaction energy matrix and $S_i(E_1, E_2) = \langle\chi'_i(E_2)|\chi_i(E_1)\rangle$ are the vibrational overlap integral. Using equation (1.3) for non-identical dipoles and inserting equation (1.21) in equation (1.19), the transition probability can be expressed as:

$$P(D'\,A \to D\,A') = \frac{2\pi t}{\hbar}\frac{\kappa^2\mu_D^2\mu_A^2}{n^4R^6}\int S_D^2(E'_D, E'_D - E)S_A^2(E_A, E_A + E)dE \quad (1.23)$$

Therefore, the rate of energy transfer can be expressed as:

$$\Gamma_{FRET} = \frac{2\pi}{\hbar}\frac{\kappa^2\mu_D^2\mu_A^2}{n^4R^6}\int S_D^2(E'_D, E'_D - E)S_A^2(E_A, E_A + E)dE \quad (1.24)$$

For fluorescence spectra $f(\nu)$ of D and A, we can consider

$$\int f(\nu)d\nu = 1. \quad (1.25)$$

Using the Boltzmann distribution for a continuous spectrum we can re-write equation (1.24) as:

$$\Gamma_{FRET} = \frac{2\pi}{\hbar}\frac{\kappa^2}{n^4R^6}\int\left[\mu_D^2\int g(E'_D)S_D^2(E'_D, E'_D - E)\,dE'_D\right].\left[\mu_A^2\int g(E_A)\,S_A^2(E_A, E_A+E)dE_A\right]\frac{d\nu}{\hbar} \tag{1.26}$$

where $g(E) = e^{-\beta E}$ is the Boltzmann factor of the fluorophore at thermal equilibrium and $\int g(E)\,dE = 1$. Now, we can define Einstein's A coefficient for spontaneous emission from the final state $|f\rangle$ to the initial state $|i\rangle$ in terms of the dipole moment as (37):

$$A_{fi} = \frac{2^5 n\pi^3\nu^3\left|\mu_{fi}\right|^2}{3c^3\hbar} = \frac{\int f(\nu)d\nu}{\tau_f} = \int d\nu\,\frac{2^5 n\pi^3\nu^3\mu^2}{3c^3\hbar}\int g\left(E_f\right)S_f^2(E_f, E_f - E)dE_f \tag{1.27}$$

where $\vec{\mu}_{fi} = \langle f|\vec{\mu}|i\rangle = \vec{\mu}S\left(E_f, E_i\right)$ is the transition dipole moment of the molecule for transition from the excited state $|f\rangle$ to the ground state $|i\rangle$ and can be defined as:

$$\vec{\mu} = -e\left\langle\Phi_f\middle|\vec{r}\middle|\Phi_i\right\rangle \tag{1.28}$$

where $|\Phi_i\rangle$ and $\left|\Phi_f\right\rangle$ are the electronic initial and final states of the molecule respectively, $S\left(E_f, E_i\right)$ is the Frank codon factor, and τ_f is the fluorescence lifetime of the molecule at the excited state $|f\rangle$. Therefore, using equation (1.27), we can express the equation for fluorescence spectrum in the frequency domain as:

$$f(\nu) = \frac{2^5 n\tau_f \pi^3 \nu^3 \mu^2}{3c^3\hbar} \int g(E_f)\, S_f^2(E_f, E_f - E) dE_f. \quad (1.29)$$

Again, the Beer-Lambert law gives (37):

$$\varepsilon(\nu) = \frac{2^2\pi^2\nu \left|\mu_{fi}\right|^2 N_A}{3000 \ln(10) n\hbar c} \quad (1.30)$$

where $\varepsilon(\nu)$ is the extinction coefficient of the molecule absorbing energy at frequency ν and N_A is the Avogadro's number. Using the definition of $\vec{\mu}_{fi}$ along with the Boltzmann factor we can write equation (1.30) for continuous distribution of energy as:

$$\int \varepsilon(\nu) d\nu = \int d\nu \frac{2^2\pi^2\nu\mu^2 N_A}{3000 \ln(10) n\hbar c} \int g(E_i)\, S_i^2(E_i, E_i + E) dE_i. \quad (1.31)$$

Equations (1.30) and (1.31) give,

$$\varepsilon(\nu) = \frac{2^2\pi^2\nu\mu^2 N_A}{3000 \ln(10) n\hbar c} \int g(E_i)\, S_i^2(E_i, E_i + E) dE_i. \quad (1.32)$$

Replacing E_D' with E_f in equation (1.29) and E_A with E_i in equation (1.32), equation (1.36) can be written as:

$$\Gamma_{FRET} = \frac{9000\kappa^2 \ln(10)\, c^4}{128\pi^5 n^4 \tau_{D'} N_A R^6} \int f_D(\nu) \varepsilon_A(\nu) \frac{d\nu}{\nu^4} = \frac{9000\kappa^2 \ln(10)\, c^4}{128\pi^5 n^4 \tau_{D'} N_A R^6} J(\nu) \quad (1.33)$$

where, $J(\nu) = \int f_D(\nu)\varepsilon_A(\nu)\frac{d\nu}{\nu^4}$ is defined as the *spectral overlap integral* (4) and τ_D, is the fluorescence lifetime of the donor. Since, in the absence of non-radiative emission of the donor, there is only one de-excitation pathway, therefore the fluorescence lifetime of the donor can be expressed as:

$$\tau_{D'} = \frac{1}{\Gamma^{r,D}} \tag{1.34}$$

and the quantum yield of the donor can be expressed as:

$$Q_D = \frac{\Gamma^{r,D}}{\Gamma^{r,D} + \Gamma^{nr,D}} = \frac{\Gamma^{r,D}}{\tau_D} \tag{1.35}$$

where τ_D is the life time of the donor which depends on both the radiative and the non-radiative energy transfer pathways. Equations (1.34) and (1.35) give:

$$\frac{1}{\tau_f} = \frac{Q_D}{\tau_D}. \tag{1.36}$$

Plugging equation (1.36) in equation (1.33) and assuming $R = R_0$, when $\Gamma_{FRET} = \Gamma^{r,D} + \Gamma^{nr,D} = \frac{1}{\tau_D}$, equation (1.33) can be written as:

$$R_0^6 = \frac{9000\kappa^2 \ln(10)\, Q_D c^4}{128\pi^5 n^4 N_A} J(\nu) \tag{1.37}$$

Using equations (1.36) and (1.37), equation (1.33) can also be written as:

$$\Gamma_{FRET} = \frac{1}{\tau_D}\left(\frac{R}{R_0}\right)^6 \tag{1.38}$$

1.2.5 Dependence of orientation factor on the energy transfer

The rate of energy transfer in FRET is also known to depend on the orientations of the interacting dipoles of donors and acceptors; hence, it is necessary to study the dependence of energy transfer rate on the orientation factor of the interacting dipoles of donors and acceptors. Using the symbols defined in Fig 1.2, the orientation factor (κ) as defined in equation (1.4) can also be expressed as:

$$\begin{aligned}\kappa^2 &= (\cos\theta_T - 3\cos\theta_D \cos\theta_A)^2 \\ &= (\sin\theta_D \sin\theta_A \cos\emptyset - 2\cos\theta_D \cos\theta_A)^2\end{aligned} \tag{1.39}$$

where the angle between dipole moment of D and A and can be defined as:

$$\cos\theta_T = \sin\theta_D \sin\theta_A \cos\emptyset + \cos\theta_D \cos\theta_A. \tag{1.40}$$

Dale et al. (38) correlated the possible range of orientation factors to the polarization of the dipoles by measuring the polarization of two randomly oriented dipoles, D, and A at a fixed distance between them. Based on their measurement of fluorescent anisotropy they calculated the possible range of κ^2. When the donor and acceptor dipoles are perpendicular to each other, equation gives $\kappa^2 = 0$ while for collinear transition dipoles, $\kappa^2 = 4$. In biological samples, there are always fluctuations in the positions of donors and acceptors as well as in their orientations because the

fluorophores are usually attached to the protein of interest via flexible linkers. Therefore, actual value of κ^2 is taken as 2/3, which is the average value of κ^2 over time, or ensemble. However, the assumption of $\kappa^2 = 2/3$ can lead to a maximum error of ~35% in the calculation of distance between the fluorophores (4). Clegg in 1996 (26) pointed out that the validity of the assumption for $\kappa^2 = 2/3$ depends on the experimental conditions and the information extracted from the experiments.

1.3 Applications of FRET

The nonlinear dependence of FRET efficiency on distance makes FRET a powerful technique to study the structure and dynamics of proteins and their interactions in living cells. Tagging suitable fluorophores at particular sites of the proteins of interest allows one to monitor protein-protein interactions. Technological advancements in the field of fluorescence microscopy have widened the scope of FRET applications, for example, to study the structure (39-41), oligomerization (16-18), conformational changes of macromolecules (42), interaction between macromolecules (7, 14, 42, 43), and biochemical events (44). NMR spectroscopy and high resolution X-ray crystallography are widely used in determining three dimensional structures of proteins and other biological macromolecules but are limited to non-living cells and, with a few notable exceptions, are not applicable to quaternary structure determinations, especially when the interactions are highly dynamic. Fluorescence microscopy, on the other hand, can be used to unveil both spatial and temporal information of molecular structures *in vivo* (43). We will review below only a few of the numerous applications of FRET.

1.3.1 Determination of structure, stoichiometry, and conformation of protein and nucleic acid complexes

FRET has attracted significant interest in the study of the structure, conformation, and stoichiometry of proteins and nucleic acids due to the difficulties in the crystallization of most of the membrane proteins. Additionally, the non-destructive nature of FRET technique makes it the most suitable method to study proteins in their natural environment. Cai et al. in 2007 revealed the structural organization and conformational changes of kinesin-1 motor proteins, which drives long-distance intracellular transport along microtubules (45). They showed that conformational changes from the inactive state to the active state of kinesin-1 are required to perform motor activation. Raicu et al. in 2009 (46) used spectrally resolved two-photon microscopy to determine the stoichiometry of alpha-receptor, Ste2p, where they tagged the receptors with GFP2/CFP as donor and YFP as acceptor and co-expressed in yeast cells. Based on the measured apparent FRET efficiencies and a theoretical model proposed by the authors, they found that Ste2p proteins form dimers.

Recently, Woz´niaka and coauthors quantitatively determined the unique 3D structure of DNA and its dependence on DNA bending using FRET (47). They used a Multiparameter Fluorescence Detection (MFD) method (48) to investigate 12 different base-pairs (bp) of a double stranded DNA helix ranging from 5 to 27 bp at the interval of every two bases. They labeled the bp using Alexa fluor 488 as the donor, and Cy5 as acceptor and calculated the orientation factors for each pair using molecular dynamics (MD) simulations. Using fluorescence lifetime as FRET analyzing method to calculate

distances between various donor-acceptor pairs in terms of measured FRET efficiencies, they were able to determine the bending and kinking of certain DNAs in all three dimensions in terms of various kink parameters as described by the authors.

1.3.2 Application of FRET based biosensors for protein kinases

Biosensors are devices used to detect structure, function, and composition of biomaterials. They are comprised of three essential components: i.e., the biomaterials, for example, enzymes, antibodies, etc.; the detector such as optical, piezoelectric, or electrochemical; and the electronics. The biosensor detector receives signal from biomaterials for sensing, the signal received by the detector is then amplified and transported to the appropriate device such as computer for display and analysis using associated electronics. Some of the commonly used commercial biosensors are blood glucose biosensors used for measuring blood glucose levels, canary in a cage used mostly by miners for detection of toxic gases, and DNA sensors for the detection of pathogenic and genetic diseases. With recent advances in biotechnology, biosensors are also used to study many complicated phenomena of protein kinases such as their activity, conformation, and regulation to name a few. Protein kinases play a critical role in signal transduction and coordination of complex cellular mechanism. By adding a phosphate group to the substrate proteins, they can change their functions by changing their activity, cellular location, or binding with other proteins. Modification in other proteins by kinases enzyme is realized through phosphorylation. Recently, FRET-based biosensors have been used for the detection of protein kinases to study kinase regulations in living cells both with spatial and temporal details. They are made by sandwiching a kinase-dependent

molecular switch between the FRET pair. The conformation of the molecular switch changes with phosphorylation. Thus monitoring FRET signal with time, kinase activity of the proteins can be monitored (49). Mizutani et al. in 2010 developed a novel biosensor called Pickles that enabled the evaluation of BCR-ABL kinase activity (50) in single living cells using FRET based techniques to diagnose chronic myeloid leukemia (CML) patients effectively and quickly (51).

1.3.3 SNP genotyping using FRET

Single nucleotide polymorphism (SNP) are considered as essential to the understanding of the genetic basis of complex diseases. It is thought that more than 300,000 SNPs will be required to understand whole genome association studies where 1.4 million SNPs have already been identified. SNP genotyping is thus one of the critical steps in the detection of SNPs. Several techniques, such as single strand conformation polymorphism (SSCP) and restriction fragment length polymorphism (RFLP), have the disadvantages of being expensive and involve multiple step processes. K. Takatasu et al. (52) in 2004 demonstrated a cost efficient technique for SNP genotyping using FRET. Their technique uses fluorescently labeled mononucleotides as universal FRET reagents instead of oligonucleotides thereby reducing time and cost of preparing fluorescently labelled oligonucleotides. In this technique a green dye, fluorescein and a red dye, cys5 with excitation/emission wavelengths of 494/517 and 650/667 nm respectively were used as donors and acceptors. PCR amplified genomic DNA was incubated with allele-specific primer in the presence of green and red dye-labeled mononucleotide and DNA polymerase. Their finding showed that, when DNA fragments contained the sequence

complementary to allele-specific primer, the extension of the primer with green and red-labeled mononucleotide occurred, resulting in red fluorescence emission due to FRET. But in the absence of the extension reaction of the primer, the DNA fragments are not complementary; hence, no FRET occurred. Thus SNP could be identified by measuring of the red fluorescence after extension reaction. In a similar work, L. Dahan et al. in 2013 (53) used Allele specific FRET probes for SNP detection in mRNA in living cells. In their work they proposed that FRET based probes can be very useful for SNP detection of live cells because FRET based probes allows to differentiate bound and unbound probes in living cells decreasing background which was considered as one of the major challenges in SNP detection.

1.3.4 Distribution and transport of lipids

Lipid molecules are known to be the modulators for a large number of biological processes and are thus by far an active field of research among cell biologists to understand the transport and distribution of lipids throughout the body. It is understood that the complex intracellular distribution of lipids are regulated by three general mechanisms namely vesicular transport, monomer transport, and lateral diffusion (54). Identification of the transport and distribution of lipids has been a difficult problem for which several techniques have been proposed so far. FRET is one of the promising successful techniques that have been applied for study of the transport mechanism of lipids. Nicholas and Pagano in 1982 (55) used FRET to study the vesicle transport of amphiphilic molecules such as phospholipids, fatty acids, and cholesterols. For the resonance energy transfer studies, they used 7-nitro-2,1,3-benzoxadiazol-4-yl (NBD) acyl

chain labeled lipids and Rhodamine B labeled phosphatidylethanolamine (N-Rh-PE) as donors and acceptors respectively to monitor the rate transfer between two populations of small vesicles. Their study showed that NBD-labeled lipids could be accurately predicted using diffusion of soluble monomers as a function of both donor and acceptor model. They also found that the rate constant for a given amphiphile depended on the lipid compositions and concentration ratios of the vesicles. Velden et al. in 2013 reported genetically encoded FRET sensor to study the bile acid transport in single living cells (56). Bile acids are known to play an essential role in the absorption of dietary fats and fat-soluble vitamins in intestines. Their findings showed that the bile acid FRET sensor was sensitive to a range of physiological and pathophysiological bile acid species easily targetable to different subcellular locations. They also demonstrated the reversible nature and suitability of FRET sensor to study both import and export of protein molecules. This application of FRET could be a significant step towards gaining the unique insight in the dynamics of bile acid transport and signaling.

1.3.5 Study of G-protein coupled receptors/ligand interactions

G-proteins coupled receptors (GPCRs) are the largest family of membrane-integrated proteins activated by ligands of varying size like small molecules, peptides, and even proteins. Study of activation of GPCRs with particular ligand to perform certain functions in cells is challenging. For many years, GPCRs have been considered to exist exclusively as monomers in the plasma membrane. Upon ligand binding, they are considered to change their conformations resulting in activation of the associated G-protein, further cascading the signal to a second messenger (57, 58). This view has been challenged in a

number of literatures showing that GPCRs can exist as a dimer and even as higher order oligomers (59-62). The measurements based on FRET techniques provide a potentially powerful way to study oligomeric/conformational changes in GPCRs upon ligand binding. The discovery and introduction of fluorescent ligands and their interactions with GPCRs have increased the capability of FRET based study of the detection and imaging of the receptors in their native environment (63, 64). Fluorescent ligand and GPCR interaction are now widely used for FRET measurements in two broad ways: (i) interaction between ligand and receptor for signaling cascade, and (ii) FRET between two labeled receptor-bound fluorescent ligands to investigate GPCRs both in transfected cells and native tissues (63). Trucatti et al. in 1996 demonstrated the possibility of measuring distances between ligand and receptor using different labeling sites on the receptor (64). Prior knowledge of the distance separating the ligand and receptor was critical to this study of ligand-receptor interaction. Another critical factor in the study of ligand-receptor interaction is that the fluorescent ligand labeling should not alter the pharmacology of the ligands owing to which Miller and co-workers performed several FRET studies using agonists and partial agonists. In their studies, they performed steady-state FRET measurements for various combinations of receptor-ligand complexes of cholecystokinin receptors (63, 65, 66). Their finding showed several distances over which the orientation of the ligand within the receptor can be determined. Additionally, similar studies performed on secretin receptors showed the possibility to determine structural constraints that allow modeling of extracellular ligand-receptor interactions (67). Lohse et al. (63) demonstrated the ligand-receptor interaction in dynamic cellular environment. Their finding showed both slow and fast components in receptor-ligand binding processes

where the slow component was attributed to receptor activation, and the fast component to simple bimolecular interaction between ligand and receptor respectively. Ilien et al. (68) developed 96-well assay for binding of unlabeled ligands using dynamic interaction studies in the muscarinic M_1-acetylcholine receptor. Later, in 2009 Ilien et al. further used dynamic interaction studies on M_1-acetylcholine receptor to demonstrate two-step binding process for small ligands to class A GPCRs (69). Albizu et al. (70) proposed a novel technique based on FRET measurement between two differently labeled fluorescent ligands to study receptor oligomerization in native tissues. Their finding showed the existence of homo- and hetero-oligomeric receptors both in transfected cells and native tissues. They also showed the existence of oxytocin receptor oligomers in mammary glands. The study of receptor-ligand interactions is continually advancing showing great applications of FRET in the study of cellular mechanisms in their complex environments. In the most recent development, Leyris et al. (71) used the combination of fluorescent ligands and N-terminally fused SNAP-tag GPCRs with a lanthanide based fluorophore substrate for SNAP-tag labeling that was found to reduce significantly the signal-to-noise ratio in Time Resolved-FRET measurements that can be used for high-throughput screening.

1.3.6 Other applications of FRET

It can be seen from above discussions that FRET is an important tool for the study of biological processes which not only helps in understanding various physiological processes, but can also be helpful in future drug developments. In a recent study, Rajagopal et al. (72) developed a super color-coding method for large scale multiplexing

of biochemical assays using standard fluorescence. Multiplexing is the simultaneous amplification of two or more DNA targets in a single reaction vessel, and is carried out using uniquely labeled probes for each target for gene detection. The available techniques are known to detect a maximum of 4 - 6 genes (73). However, the method developed by Rajagopal et al. has the capability to predict theoretically unlimited number of independent targets with any combination of biochemical assays in a reaction vessel. The method provided easy access to 12-plex assays compared to 4-plex assays that are currently being used. It was proposed that the theory when combined with FRET can further help in expanding the encoding set that can increase the number of gene detection in a large combination of biochemical assays.

Apart from biological applications, FRET also finds its application in diverse fields such as electronics, nanotechnology, as well as optical, electron, and mass spectroscopy and photographic processes. Coffey et al. (74) proposed a mechanism of long-range FRET-based charge transfer from a donor to acceptor in organic solar cells that were otherwise understood to be mainly governed by charge diffusion process which can better help to understand and improve the solar cell performance in certain types of solar cells. Bose et al. (75) for the first time performed time-resolved cryogenic FRET in densely packed quantum dot films using single photon counting set up. Their finding showed 94% energy transfer efficiency for donor dots showing a promising step towards photovoltaic and quantum communication. Kelley et al. (76) developed zinc chlorophyll derivative that can mimic the photosynthetic process. They found the FRET as an additional energy transfer mechanism to already known ultrafast energy transfer process

existing within cyclic self-assembled chlorophyll tetramers that can help to improve the charge transfer process and hence the efficiency of solar cells. Halivni et al. (77) presented a detailed study on the effect of nanoparticle dimensionality on FRET in nanoparticle-dye conjugated system. Their investigation showed that both the size and the geometry of nano-dimensional system can affect the FRET efficiency significantly. The results can be found promising in using FRET for a wide variety of applications based on nanomaterials such as bio-sensing, spectroscopy, and energy harvesting materials. Lee et al. (78) studied the dynamics of multilayer DNA films using FRET. The DNA films were assembled on silica particles with alternating layers of homopolymeric diblocks (Poly A15G15 and Poly T15C15) with fluorophore, TAMRA (Poly A15G15-TAMRA) and quencher, BHQ2 (Poly T15C15-BHQ2). Their study showed rearrangements in DNA films confirming the dynamics through spontaneous hybridization and are considered to have significant applications in drug discovery and bio-sensing. Busch et al. (79) reported an *in vivo* spectral multiplexing approach for imaging of different disease-related biomarkers using near infra-red FRET imaging. The technique finds its relevance in imaging multiple disease causing molecules *in vivo* instead of just one molecule. They demonstrated the success of their method by showing FRET measurements on coupled fluorophores DY-682 and DY-505 as donors and DY-782 as acceptors along with the antibody IgG. Their technique can be particularly useful in the identification of several pathological conditions such as inflammation, cancer, and neurodegenerative diseases. Wang et al. (80) proposed the use of the photoacoustic microscopy technique for imaging of FRET that produces heat and acoustic waves. Their study showed increased penetration depth for FRET imaging compared to confocal microscopy along with the

benefits of three-dimensional imaging with scalable resolution. Their technique can be particularly useful as a biomedical tools for *in vivo* FRET studies. Liu et al. (81) proposed a highly sensitive and selective technique for cysteine detection in FAM (carboxyfluorocein) tagged single stranded DNA (ssDNA) and graphene oxide using FRET. They showed significant fluorescence quenching due to FRET in non-covalently assembled FAM-ssDNA and graphene oxide. A decrease in fluorescent intensity was found with the increase in cysteine concentration improving the sensitivity for cysteine detection in DNA.

References:

1. Phizicky EM & Fields S (1995). Protein-protein interactions: Methods for detection and analysis. *Microbiol Rev* 59(1):94-123.

2. Zhu H, et al. (2001). Global analysis of protein activities using proteome chips. *Science* 293(5537):2101-2105.

3. Yan Y & Marriott G (2003). Analysis of protein interactions using fluorescence technologies. *Curr Opin Chem Biol* 7(5):635-640.

4. Lakowicz JR (2006). Principles of fluorescence spectroscopy (Springer, New York).

5. Brown MP & Royer C (1997). Fluorescence spectroscopy as a tool to investigate protein interactions. *Curr Opin Biotechnol* 8(1):45-49.

6. Weiss S (1999). Fluorescence spectroscopy of single biomolecules. *Science* 283(5408):1676-1683.

7. Parsons M, Vojnovic B & Ameer-Beg S (2004). Imaging protein-protein interactions in cell motility using fluorescence resonance energy transfer (fret). *Biochem Soc Trans* 32(Pt3):431-433.

8. Lleres D, Swift S & Lamond AI (2007). Detecting protein-protein interactions in vivo with fret using multiphoton fluorescence lifetime imaging microscopy (flim). *Curr Protoc Cytom* Chapter 12:Unit12 10.

9. Ai HW, Hazelwood KL, Davidson MW & Campbell RE (2008). Fluorescent protein fret pairs for ratiometric imaging of dual biosensors. *Nature Methods* 5(5):401-403.

10. You X, et al. (2006). Intracellular protein interaction mapping with fret hybrids. *Proc Natl Acad Sci U S A* 103(49):18458-18463.

11. Hillger F, Nettels D, Dorsch S & Schuler B (2007). Detection and analysis of protein aggregation with confocal single molecule fluorescence spectroscopy. *J Fluoresc* 17(6):759-765.

12. Raicu V (2010). Fret-based determination of protein complex structure at nanometer length scale in living cells. Nanoscopy and multidimensional optical fluorescence microscopy, ed Diaspro A (CRC Press, Boca Raton).

13. Piston DW & Kremers GJ (2007). Fluorescent protein fret: The good, the bad and the ugly. *Trends Biochem Sci* 32(9):407-414.

14. Raicu V, et al. (2009). Determination of supramolecular structure and spatial distribution of protein complexes in living cells. *Nature Photon* 3(2):107-113.

15. Raicu V, Fung R, Melnichuk M, Chaturvedi A & Gillman D (2007) Combined spectrally-resolved multiphoton microscopy and transmission microscopy employing a high-sensitivity electron-multiplying ccd camera. *Proc SPIE*, eds Periasamy A & So PTC, p 64420M.

16. Patowary S, et al. (2013). The muscarinic m3 acetylcholine receptor exists as two differently sized complexes at the plasma membrane. *Biochem J* 452(2):303-312.

17. Singh DR, et al. (2013). Determination of the quaternary structure of a bacterial atp-binding cassette (abc) transporter in living cells. *Integr Biol* 5(2):312-323.

18. Pisterzi LF, et al. (2010). Oligomeric size of the m2 muscarinic receptor in live cells as determined by quantitative fluorescence resonance energy transfer. *J Biol Chem* 285(22):16723-16738.

19. Lappano R & Maggiolini M (2011). G protein-coupled receptors: Novel targets for drug discovery in cancer. *Nat Rev Drug Discov* 10(1):47-60.

20. George SR, O'Dowd BF & Lee SP (2002). G-protein-coupled receptor oligomerization and its potential for drug discovery. *Nature Reviews Drug Discovery* 1(10):808-820.

21. Kroeze WK, Sheffler DJ & Roth BL (2003). G-protein-coupled receptors at a glance. *J Cell Sci* 116(Pt 24):4867-4869.

22. Lundstrom K (2009). An overview on gpcrs and drug discovery: Structure-based drug design and structural biology on gpcrs. *Methods Mol Biol* 552:51-66.

23. Raicu V (2007). Efficiency of resonance energy transfer in homo-oligomeric complexes of proteins. *J Biol Phys* 33(2):109-127.

24. He J, et al. (2012). The role of muscarinic acetylcholine receptor type 3 polypeptide (m3rp205-220) antibody in the saliva of patients with primary sjogren's syndrome. *Clin Exp Rheumatol* 30(3):322-326.

25. Wess J (2004). Muscarinic acetylcholine receptor knockout mice: Novel phenotypes and clinical implications. *Annu Rev Pharmacol Toxicol* 44:423-450.

26. Clegg RM (1996). Fluorescence resonance energy transfer. Fluorescence imaging spectroscopy and microscopy, eds Wang XF & Herman B (Wiley-Interscience, New York), Vol 137.

27. Berney C & Danuser G (2003). Fret or no fret: A quantitative comparison. *Biophys J* 84(6):3992-4010.

28. Clegg RM (2006). The history of fret: From conception through the labors of birth Reviews in fluorescence, ed Chris D. Geddes JRL (Springer), pp 1-45.

29. London HKaF (1928). Uber quantenmechanische energieiibertragungen zwischen atomaren systemen. *Z Physik Chem* B(2):207-243.

30. Förster T (1946). Energiewanderung und fluoreszenz. *Naturwissenschaften* 33(6):166-177.

31. Perrin J (1927). Fluorescence et induction moleculaire par resonance. *CR Hebd Seances Acad Sci* 184:1097-1100.

32. Perrin F (1932). Theorie quantique des transferts d'activation entre molecules de meme espece. Cas des solutions fluorescentes. *Ann Chim Phys* 17::283-314.

33. Perrin F (1933). Interaction entre atomes normal et activite. Transferts d'activitation. Formation d'une molecule activitee. *Ann Institut Poincare* 3::279-318.

34. Jackson JD (1998). Classical electrodynamics (John Wiley and Sons, Inc, New York) Third Ed.

35. Forster T (1948). Zwischenmolekulare energiewanderung und fluoreszenz. *Ann Phys* 2:55-75.

36. Shankar R (2007). Principles of quantum mechanics (Springer) Second Ed.

37. Singh DR (2012). Investigation of the quaternary structure of an abc transporter in living cells using spectrally resolved resonance energy transfer. Doctor of Philosophy (University of Wisconsin-Milwaukee).

38. Dale RE, Eisinger J & Blumberg WE (1979). The orientational freedom of molecular probes. The orientation factor in intramolecular energy transfer. *Biophys J* 26(2):161-193.

39. E Haas MW, E Katchalski-Katzir and I Z Steinberg (1975). Distribution of end-to-end distances of oligopeptides in solution as estimated by energy transfer. *Proc Natl Acad Sci U S A* 72(5):1807–1811.

40. Lakowicz JR, et al. (1990). Conformational distributions of melittin in water/methanol mixtures from frequency-domain measurements of nonradiative energy transfer. *Biophys Chem* 36(2):99-115.

41. Chapman ER, Alexander K, Vorherr T, Carafoli E & Storm DR (1992). Fluorescence energy transfer analysis of calmodulin-peptide complexes. *Biochemistry* 31(51):12819-12825.

42. Heyduk T (2002). Measuring protein conformational changes by fret/lret. *Curr Opin Biotechnol* 13(4):292-296.

43. Truong K & Ikura M (2001). The use of fret imaging microscopy to detect protein-protein interactions and protein conformational changes in vivo. *Curr Opin Struct Biol* 11(5):573-578.

44. Bunt G & Wouters FS (2004). Visualization of molecular activities inside living cells with fluorescent labels. *Int Rev Cytol* 237:205-277.

45. Cai D, Hoppe AD, Swanson JA & Verhey KJ (2007). Kinesin-1 structural organization and conformational changes revealed by fret stoichiometry in live cells. *J Cell Biol* 176(1):51-63.

46. Raicu V, Jansma DB, Miller RJ & Friesen JD (2005). Protein interaction quantified in vivo by spectrally resolved fluorescence resonance energy transfer. *Biochem J* 385(Pt 1):265-277.

47. Wozniak AK, Schroder GF, Grubmuller H, Seidel CA & Oesterhelt F (2008). Single-molecule fret measures bends and kinks in DNA. *Proc Natl Acad Sci U S A* 105(47):18337-18342.

48. Widengren J, et al. (2006). Single-molecule detection and identification of multiple species by multiparameter fluorescence detection. *Anal Chem* 78(6):2039-2050.

49. Zhang J & Allen MD (2007). Fret-based biosensors for protein kinases: Illuminating the kinome. *Mol Biosyst* 3(11):759-765.

50. An X, et al. (2010). Bcr-abl tyrosine kinase inhibitors in the treatment of philadelphia chromosome positive chronic myeloid leukemia: A review. *Leuk Res* 34(10):1255-1268.

51. Mizutani T, et al. (2010). A novel fret-based biosensor for the measurement of bcr-abl activity and its response to drugs in living cells. *Clin Cancer Res* 16(15):3964-3975.

52. Takatsu K, Yokomaku T, Kurata S & Kanagawa T (2004). A new approach to snp genotyping with fluorescently labeled mononucleotides. *Nucleic Acids Res* 32(7):e60.

53. Dahan L HL, Kedmi R, Behlke MA, Peer D (2013). Snp detection in mrna in living cells using allele specific fret probes. *Plos One* 8(9).

54. Sleight RG (1987). Intracellular lipid transport in eukaryotes. *Annu Rev Physiol* 49:193-208.

55. Nichols JW & Pagano RE (1982). Use of resonance energy transfer to study the kinetics of amphiphile transfer between vesicles. *Biochemistry* 21(8):1720-1726.

56. van der Velden LM, et al. (2013). Monitoring bile acid transport in single living cells using a genetically encoded forster resonance energy transfer sensor. *Hepatology* 57(2):740-752.

57. Lefkowitz RJ (2004). Historical review: A brief history and personal retrospective of seven-transmembrane receptors. *Trends Pharmacol Sci* 25(8):413-422.

58. Smith NJ & Milligan G (2010). Allostery at g protein-coupled receptor homo- and heteromers: Uncharted pharmacological landscapes. *Pharmacol Rev* 62(4):701-725.

59. Milligan G (2004). G protein-coupled receptor dimerization: Function and ligand pharmacology. *Mol Pharmacol* 66(1):1-7.

60. Milligan G (2006). G-protein-coupled receptor heterodimers: Pharmacology, function and relevance to drug discovery. *Drug Discov Today* 11(11-12):541-549.

61. Milligan G (2008). A day in the life of a g protein-coupled receptor: The contribution to function of g protein-coupled receptor dimerization. *Br J Pharmacol* 153 Suppl 1:S216-229.

62. Palczewski K (2010). Oligomeric forms of g protein-coupled receptors (gpcrs). *Trends Biochem Sci* 35(11):595-600.

63. Lohse MJ, Nuber S & Hoffmann C (2012). Fluorescence/bioluminescence resonance energy transfer techniques to study g-protein-coupled receptor activation and signaling. *Pharmacol Rev* 64(2):299-336.

64. Turcatti G, et al. (1996). Probing the structure and function of the tachykinin neurokinin-2 receptor through biosynthetic incorporation of fluorescent amino acids at specific sites. *Journal of Biological Chemistry* 271(33):19991-19998.

65. Harikumar KG, Gao F, Pinon DI & Miller LJ (2008). Use of multidimensional fluorescence resonance energy transfer to establish the orientation of cholecystokinin docked at the type a cholecystokinin receptor. *Biochemistry* 47(36):9574-9581.

66. Harikumar KG & Miller LJ (2005). Fluorescence resonance energy transfer analysis of the antagonist- and partial agonist-occupied states of the cholecystokinin receptor. *Journal of Biological Chemistry* 280(19):18631-18635.

67. Harikumar KG, et al. (2007). Fluorescence resonance energy transfer analysis of secretin docking to its receptor: Mapping distances between residues distributed throughout the ligand pharmacophore and distinct receptor residues. *Journal of Biological Chemistry* 282(45):32834-32843.

68. Ilien B, et al. (2003). Fluorescence resonance energy transfer to probe human m1 muscarinic receptor structure and drug binding properties. *J Neurochem* 85(3):768-778.

69. Ilien B, et al. (2009). Pirenzepine promotes the dimerization of muscarinic m1 receptors through a three-step binding process. *Journal of Biological Chemistry* 284(29):19533-19543.

70. Albizu L, et al. (2010). Time-resolved fret between gpcr ligands reveals oligomers in native tissues. *Nat Chem Biol* 6(8):587-594.

71. Leyris JP, et al. (2011). Homogeneous time-resolved fluorescence-based assay to screen for ligands targeting the growth hormone secretagogue receptor type 1a. *Anal Biochem* 408(2):253-262.

72. Rajagopal A, Scherer A, Homyk A & Kartalov E (2013). Supercolor coding methods for large-scale multiplexing of biochemical assays. *Anal Chem* 85(16):7629-7636.

73. Persson K, Hamby K & Ugozzoli LA (2005). Four-color multiplex reverse transcription polymerase chain reaction--overcoming its limitations. *Anal Biochem* 344(1):33-42.

74. Coffey DC, Ferguson AJ, Kopidakis N & Rumbles G (2010). Photovoltaic charge generation in organic semiconductors based on long-range energy transfer. *ACS Nano* 4(9):5437-5445.

75. Bose R, et al. (2008). Temperature-tuning of near-infrared monodisperse quantum dot solids at 1.5 microm for controllable forster energy transfer. *Nano Lett* 8(7):2006-2011.

76. Kelley RF, Goldsmith RH & Wasielewski MR (2007). Ultrafast energy transfer within cyclic self-assembled chlorophyll tetramers. *J Am Chem Soc* 129(20):6384-6385.

77. Halivni S, Sitt A, Hadar I & Banin U (2012). Effect of nanoparticle dimensionality on fluorescence resonance energy transfer in nanoparticle-dye conjugated systems. *ACS Nano* 6(3):2758-2765.

78. Lee L, Johnston AP & Caruso F (2012). Probing the dynamic nature of DNA multilayer films using forster resonance energy transfer. *Langmuir* 28(34):12527-12535.

79. Busch C, et al. (2012). An in vivo spectral multiplexing approach for the cooperative imaging of different disease-related biomarkers with near-infrared fluorescent forster resonance energy transfer probes. *J Nucl Med* 53(4):638-646.

80. Wang Y & Wang LV (2012). Forster resonance energy transfer photoacoustic microscopy. *J Biomed Opt* 17(8):086007.

81. Liu H, Wang Y, Shen A, Zhou X & Hu J (2012). Highly selective and sensitive method for cysteine detection based on fluorescence resonance energy transfer between fam-tagged ssdna and graphene oxide. *Talanta* 93:330-335.

Chapter 2. Experimental techniques for measuring FRET

As already discussed in Chapter 1, FRET is one of the widely used techniques that has the capability to study molecular processes in subnanometer resolution because of its versatility, sensitivity and specificity. Compared to other techniques such as X-ray diffraction, nuclear magnetic resonance, and electron microscopy, FRET-based fluorescence microscopy offers the advantage of studying both fixed and live cells with improved spatial (angstrom) and temporal (nanosecond) resolution. Several FRET techniques based on wide-field confocal microscopy, fluorescence lifetime imaging microscopy (FLIM), fluorescence correlation spectroscopy (FCS), two photon microscopy, total internal reflection microscopy (TIRF), and polarization anisotropy have continuously been advancing enabling the study from single molecules to live-animals. This chapter provides an overview of some popular FRET-based fluorescence microscopic techniques along with their advantages and limitations, with emphasis on a spectrally resolved two-photon microscope developed in our lab. Common to all fluorescence microscopic techniques, FRET measurements also require protein tagging with fluorescent probes. Most of the FRET pairs used for tagging proteins of interest come from a class of naturally fluorescent proteins called green fluorescence proteins (GFPs) and their variants. A brief review on the variants of GFPs as FRET pairs and their significance in fluorescence microscopy is also given in this chapter.

2.1 Green fluorescence proteins (GFPs) and its variants

The green fluorescent protein, originally found in the *Aequorea victoria* jellyfish, is a protein consisting of 239 amino acid residues and a molecular mass of 26.9 kDa. GFP is known to exhibit green fluorescence when exposed to blue or violet light (1). Various fluorescent proteins are known to be present in several coelenterates such as *Aequorea, Phialidium,* and *Renilla* (2, 3). Because of their advantageous ptotophysical properties, fluorescent proteins are often used as fluorescent markers or "tags" to protein of interest for the study of numerous aspects in cell biology, neurobiology, and ecology (4). By monitoring the location of the GFP tag, using a fluorescence microscope, information regarding the protein of interest if also ascertained.

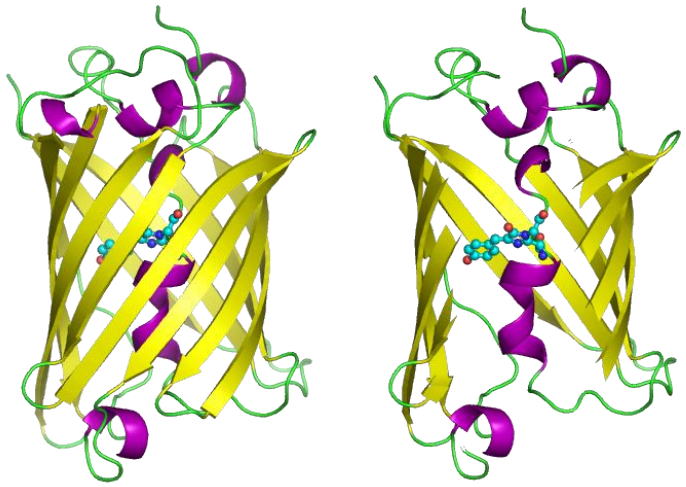

Figure 2.1 Schematic depiction of the green fluorescence protein (GFP). On the left, the entire GFP with fluorophore at the center is shown, while on the right, a cutaway portion of the GFP is shown, revealing the central fluorophore distinctively. The yellow ribbons and pink helices represent $\boldsymbol{\beta}$ – sheets and $\boldsymbol{\alpha}$ helices, respectively. The image is taken from (5).

The benefit of using GFPs for protein tagging stems from the fact that they are naturally formed by cyclization of the peptide backbone without using other cofactors for

syntheses. Therefore, they do not alter the normal function or localization of their fusion partner (1). Additionally, localization of GFPs does not require fixation or permeabilization for substrate entry, making it an extremely useful candidate for the study of cellular dynamics in living cells (6)**.** GFPs have a barrel-like structure comprised of eleven β-sheets. Six α helices run diagonally through the center of the barrel as shown in Fig. 2.1. The chromophore is at the center of the β sheet barrel, which is the portion of the known for its fluorescence. The fluorophore of GFP is not a separately synthesized prostethic group; rather it is composed of amino acid residues 65-67 (Threonone-Tyrosine-Glycine) within the polypeptide chain.

2.1.1 GFP as fluorescence marker

The most successful application of GFPs stems from its use as a fluorescent marker of a non-fluorescent protein. The gene encoding the GFP is fused in frame to the gene of the protein of interest, and the resulting gene is expressed in cells or an organism. Thus, GFPs are mostly used as a tag or as an indicator in cell biology to monitor the expression level and localization of the proteins in a subcellular region (3, 7). In FRET studies, two different types of GFPs are generally used: one as a donor, and one as an acceptor, which are fused to the same, or different proteins of interest to study homo-, and hetero-interactions respectively. By monitoring the energy transfer efficiency (FRET efficiency) occurring between the donor and acceptor, the distance between the proteins tagged with donors and acceptors can be determined.

2.1.2 GFP classes

Based on the distinctive components of the chromophores, GFPs are divided into seven different classes with each class containing distinct sets of excitation and emission spectra (8), (3).

(i) Class 1 GFPs are widely known as wild-type (wt) GFPs, have the most complex spectra among all GFPs. The co-existence of neutral-phenol and anionic-phenol chromophores of the wild-type GFPs gives two peaks in their excitation spectra: one, dominant peak at 395 nm (due to a neutral chromophore) with an emission peak at 504 nm and second, a minor peak (almost three times lower) at 470 nm (due to anion chromophore) with emission at 506 nm. The UV light source used to excite wt-GFPs at 395 nm can damage the tissues. In addition, the detected signals contain a significant contribution from cellular auto-fluorescence. These problems can be avoided using the second excitation peak, however it is not very efficient since only 15% of the class I proteins contain anionic chromophore.

(ii) Class 2 GFPs with phenolate anions in chromophores are very commonly used among all classes of GFPs because they were first known group of brighter fluorophores with simple spectra. They were mutated to suppress the 395 nm excitation peak of wt-GFP and enhance the 470 nm excitation peak by five to six fold, so named as enhanced GFP (EGFP). The mutation shifts the excitation peak to 488-490 nm with an emission peak at 509-511 nm.

(iii) Class 3 GFPs with a neutral phenol in the chromophore is mutated to eliminate the anionic chromophore resulting the excitation and emission wavelengths at

399 and 511 nm respectively. This class of GFPs is advantageous to use because of their largest separated excitation and emission spectra among the classes.

(iv) Class 4 GFPs are also known as yellow fluorescent protein (YFP) due to the extended tail of their emission spectrum in the yellow wavelength range giving an overall yellowish appearance. They are mutated by stacking an aromatic ring next to the phenolate anion of the chromophore resulting an increase of the excitation and emission spectrum up to 20 nm. Depending on the combinations of aromatic residues used at the amino acid (AA) positions of 65, and 203, there are different fluorophores named as e-YFP, Venus, Citrine etc. included in this group of GFPs. The members of this group differ in their brightness and slightly in their excitation and emission spectra in the range of 508 - 516 nm, and 518 - 529nm respectively.

(v) Class 5 GFPs are produced by substituting Trp with Tyr at the AA position 66 making a new chromophore with indole (9) instead of phenol. This class of GFPs are commonly called cyan fluorescent proteins (CFPs) because of their excitation and emission wavelengths of 436 and 485 nm respectively, example includes Cerulean.

(vi) Class 6 also named as blue fluorescent proteins (BFP) results from the mutation replacing Tyr with His at position 66 (9) shifting its excitation and emission wavelength to shorter than Trp66 in class 5 GFPs. They have excitation at 383 nm and emission at 447 nm, so the emission is blue.

(vii) Class 7 is developed with mutation of Phe at 66 giving shortest excitation and emission wavelengths among the classes at 360 and 442 nm respectively. This class is very little investigated because of its lack of practical applications.

2.1.3 Selection of FRET pairs

As discussed in chapter 1, the FRET efficiency depends on the Förster distance, R_0 (distance of 50% energy transfer efficiency) that is governed by many parameters such as the overlap of donor emission and acceptor excitation spectra, quantum yield of the donor, extinction coefficient of acceptor, etc. (10). Therefore, it is important to consider the spectroscopic properties of donor and acceptor in choosing GFP variants as workable FRET pairs.

Selection of an appropriate donor and acceptor pair, from among the wide range of available fluorophores, which satisfies the necessary conditions needed to observe FRET, is identified as one of the prerequisites for improving the accuracy and resolution of FRET measurement. Since the discovery and characterization of purified GFPs by Shimomura, active efforts in molecular biology have been going on to identify and develop suitable FRET pair fluorophore with improved brightness, photostability, maturation speed, and efficiency.

The most important condition for choosing fluorophores as a FRET pair is that the excitation spectrum of the acceptor should overlap appreciably with the emission spectrum of the donors. The amount of overlap is calculated using the *spectral overlap integral* defined in equation (1.33). While spectral overlap is the utmost importance in choosing a FRET pair, there do exist a number of other important concerns which must be taken in to account: (i) fluorescent proteins fused to the proteins of interest should be non-toxic to the cells; (ii) they should be bright enough to be able to detect by the

instrument while overcoming the signal of auto-fluorescence; (iii) while studying oligomerization of proteins, it is important to tag the monomeric form of a fluorescent protein to the protein of interest so that the fluorophore doesn't promote oligomerization; (iv) the fluorescent proteins should be insensitive to the environmental conditions of the cells *in vivo* measurements in order to correctly interpret the effect of environment on the protein of interest; (v) while performing multicolor FRET experiments using filter-based methods, it is important to have minimum spectral cross-talk and bleed-through between the fluorophores and (vi) if a high power laser is used as the excitation source in the measurement technique, it is critical to choose the photo-stable fluorophores to minimize the effect of photo-bleaching.

Depending on the imaging techniques, the GFP classes that are used as FRET pairs are BFP-GFP, GFP-YFP, and CFP-YFP as donors-acceptors respectively (10). The BFP fluorophores suffers from the disadvantages of having both the lowest quantum yield and also the lowest photostability among all GFP variants (9). Because of its excitation peak in UV-range, the emission spectrum of BFP includes a significant contribution from cellular auto-fluorescence which adds signal, and hence increase the amount of noise in intensity measurements (11). To address these problems, BFP was replaced by CFP family members as donors and in order to minimize spectral cross-talk (described later in this chapter) for CFP-GFP excitation spectrum, fluorophores from YFP class are chosen as an acceptors. Another advantage of CFP-YFP as a FRET pairs are its calculated R_0 value of ~ 5 nm whereas for BFP-GFP pair, it is 4 nm making it feasible to detect FRET for larger donor-acceptor distance. The most commonly used

CFP-YFP FRET pairs include: Cerulean-Venus, Cerulan-Citrine, ECFP-EYFP etc. Also, a recently developed GFP based FRET pair, GFP_2-YFP proved as useful FRET pair particularly for spectral FRET coupled with linear unmixing method (described in section 2.3.4) due to its low spectral cross-talk and spectral bleed-through and larger *spectral overlap integral* (12). GFP_2 is a modified version of wt-GFP with a F64L substitution that significantly increases the brightness. It has similar excitation and emission peak at 396 and 504 nm respectively as wt-GFP_2. Recent developments in technology have helped in cloning red fluorescent proteins (RFPs) from corals that make it possible to use fluorophore with higher excitation spectra as donors (YFPs) and RFPs as acceptors which can be a better choice in terms of avoiding auto-fluorescence (13).

2.2 Challenges in FRET measurements

There are several experimental issues that can challenge FRET measurements leading to a misinterpretation of the results. With the advancement in recent technologies, several microscopic techniques are applied to measure FRET at different levels of precision and accuracy.

2.2.1 Widely used assumptions in FRET measurements

FRET based measurements use several assumptions and these needed to be taken care of to interpret the results accurately. For example, it is assumed that there is always a non-radiative resonance energy transfer between donor and acceptor and the probability of reabsorption of the donor emission fluorescence by the acceptor is neglected (14, 15). This phenomenon is less probable in a system of low fluorophore density, but cannot be

neglected when fluorophore density is very high (14). A second commonly used assumption in FRET measurements is that, it is anticipated that the properties of the FRET pair will not change when tagged with other biological molecules of interest. Also the molecular interaction between FRET pairs as well as with the surrounding molecules is always neglected but these interactions can change the overall properties of the FRET (15).

Apart from the above mentioned assumptions there are several common problems that are generally addressed and are widely studied which include spectral cross talk and spectral bleed-through, non-specific FRET, mixture of fluorophore populations, variable expression levels of energy donors and acceptors, relative brightness of the fluorophores, auto-fluorescence, detector saturation, optical noise, and photo-bleaching. Each of these problems is discussed in more detail below.

The ideal condition of FRET is that the excitation spectrum of acceptor and emission spectrum of the donor should overlap with each other significantly without overlap of excitation, or emission spectra of both the fluorophores, which is rarely true in reality. Due to relatively small Stokes' shift of GFP variants, there is always overlap of excitation, and emission spectra of GFP variant FRET pairs (16). The overlap of the excitation spectra of donor and acceptor is called spectral cross talk while the overlap of the emission spectra is termed as spectral bleed-through. The plot displayed in Fig. 2.2. shows a FRET pair with both an appreciable spectral cross talk as well as spectral bleed-through, illustrated by the grey and red shaded regions, respectively. Due to spectral cross

talk, both donor and acceptor are excited to a different extent at the same excitation wavelength resulting in contamination of FRET signal by direct excitation of the acceptor. Similarly, due to spectral bleed-through donor emission is detected through the acceptor channel. These two artifacts affect and complicate the value of FRET calculated from the signal contaminated by these effects. Spectral cross talk and bleed through is usually determined by comparing the fluorescence intensities of three different types of samples i.e., donor-only sample, acceptor-only sample, and a sample with both donor and acceptor (FRET pair). All the three samples are excited at the donor excitation wavelength, and the emission is measured at the acceptor emission channel. Measuring the emission spectra of the donor and calculating its quantum yield in the wavelength range of the acceptor emission channel determines the extent of spectral cross talk. The contribution of spectral bleed-through is determined from the extinction coefficient of the acceptor fluorophore at the donor excitation wavelength and the relative excitation light intensity of both donor and acceptor (15). The signals due to spectral cross-talk and bleed-through are then subtracted from the measured signal at acceptor channel; the resulting signal thus contains signal purely from the FRET. But information about the dynamics is lost in the process since it is not possible to measure the crosstalk and bleed through signal simultaneously using the same sample as used for FRET measurement.

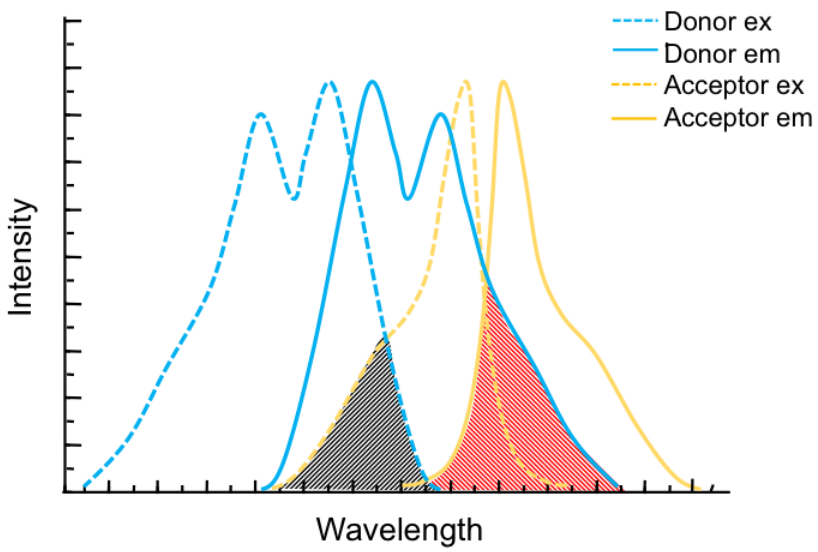

Figure 2.2 Schematic representation of normalized excitation and emission spectrum of a donor (D) and acceptor (A) (not in scale). Solid and dotted lines represent excitation and emission of D (cyan) and A (yellow). Shaded area shown in black, and red color represents spectral cross-talk, and spectral bleed-through respectively.

Another problem occurring in FRET measurements is the requirement of high level of the fluorescence signal. It is true that the level of fluorescence signal can be increased by either increasing the power of excitation light or by increasing the number of fluorophores in the sample. However, each of these solutions brings problems to their own. Increasing the excitation intensity can lead to extensive photobleaching of the sample and is also restricted by the upper limit of the excitation power of the measuring system. Increasing the number of fluorophores, on the other hand, decreases the intermolecular distances between the fluorophores. As the intermolecular distance between fluorophores decreases, the probability of a number of unassociated donors and acceptors being within distances close enough for FRET to occur increases. This effect is often referred to as non-specific or stochastic FRET, leads to FRET occurring between non-interacting proteins. This non-specific FRET is usually detected through the

dependence of FRET on fluorescent intensity which is usually determined by plotting the measured FRET values vs. the intensity of either donor or acceptor (15). Also, donor to acceptor ratios outside the range of 1:10 and 10:1 also limits the detection of FRET signals (17).

The measured FRET efficiency values are also affected by having undesired fluorophore combinations, such as uncoupled fluorophores or like fluorophore pairs within the fluorophore population (18). The occurrence of fluorescence from such fluorophore combinations contributes to the overall measured fluorescence intensities, but because no FRET is occurring to these entities, a decrease in the actual FRET efficiency value occurs. The error in the measured FRET efficiency can be pronounced in a system of mixed fluorophore population with varying expression levels in cells where the concentrations of donor and acceptors vary remarkably. The quantification of extraneous signal from the fluorescence of undesired fluorophores can be performed by measuring the fractional decrease or increase in the donor and acceptor intensities respectively (18). Finally, the optical noise or background noise when studying single molecule detection because of low signal to noise ratio (15).

2.3 Experimental techniques to measure FRET

In vivo FRET spectroscopy has become widely used in last 30 years since it is very sensitive and relatively easy to perform. Since FRET techniques can resolve the distance up to molecular level (< 10nm) irrespective of the scale of the sample, FRET is also dubbed by Stryer as the spectroscopic or molecular ruler (19). *In vivo* FRET experiments,

however, are often difficult to interpret because of the complexity of living biological systems. Successful quantitative measurements and interpretation of data requires availability of correct control experiments and the ability to choose the best methods on particular samples (20). Some of the widely used FRET techniques with their advantages and limitations are discussed in this section.

2.3.1 Sensitized emission

Sensitized emission is one of the most widely used techniques for the measurement of FRET, being applicable to study both live and fixed cells. In this method, the sample for FRET measurement is excited at an excitation wavelength known to excite the donor, and emission is measured through the acceptor channel. In most cases, it is difficult to isolate the activity of single fluorophores due to the artifacts of spectral crosstalk and bleed-through as described in section 2.2.2. The measured signal contains the signal arising due to FRET along with that from direct excitation of the acceptor and also from the donor emission spectrum because of spectral cross-talk and bleed-through respectively. In order to minimize artifacts caused by bleed-through and cross-talk, three different measurements are performed one on each of the three different types of samples: donor-only samples, acceptor-only sample and sample with both donor and acceptor (FRET pair) as discussed before. The signals obtained from donor-only and acceptor-only are then subtracted from the measured spectra containing both donor and acceptor, the resulting signal thus contains signals purely from FRET. It is important to keep all experimental parameters such as detector/amplifier gain, emission wavelength window, zoom, scan speed, pinhole size etc. the same for all three samples. Though promising,

this method suffers from the disadvantage of low intensity, environmental susceptibility and chemical and photochemical instability (21). The method also requires extensive image processing, making the process laborious and more prone to errors (21). Additionally, the controls used for the measurement are different samples, hence FRET measurement for an unknown stoichiometry as well as for the system with continuously changing concentrations of donors, and acceptors become extremely difficult, limiting its application for the study of complex cellular environment and their dynamics (21).

2.3.2 Fluorescence lifetime imaging microscopy (FLIM)

Fluorescence spectroscopy measurements can be divided into two broad classes, namely steady state and time resolved. Steady state measurement use a constant illumination of the sample. It is well known that the excitation/de-excitation phenomena occur on the nanosecond (ns) scale, therefore the steady state is reached immediately after light exposure hence the term steady state. Time-resolved measurements, on the other hand, use short pulses of less than a ns so that the molecular phenomena can be recorded before the excited fluorophore reaches the ground state (4). Steady state is thus considered as the time average of such several short phenomena. Though complex and expensive, time resolved techniques in many cases are more useful compared to steady state measurements. The time resolved measurement contains information about the anisotropy of the sample that is helpful for determining the shape and flexibility of macromolecules, information which is lost in steady state measurements. Additionally, the time resolved measurements contain several significant pieces of information such as the ability to detect multiple lifetimes of one molecule show more than one conformation of a

molecule. It also reveals the distribution of acceptors around donors and quenching phenomena.

Time resolved spectroscopy is known to measure the lifetime of the excited state of a molecule. The excited state lifetime can be understood as the amount of time taken by the excited-state population to decay to its ground state and is also known as decay time (4). Lifetime can also be defined as the average amount of time a fluorophore remains in its excited state after excitation. The following relation is used to obtain the value of lifetime (4):

$$\langle t \rangle = \frac{\int_0^\infty t exp\left(-t/\tau\right) dt}{\int_0^\infty exp\left(-t/\tau\right) dt} \tag{2.1}$$

where t is time, and τ is the average lifetime of the excited state.

The most common instruments used for lifetime measurements are time-resolved fluorescence spectroscopes whereby the fluorescence intensity decay over time is recorded, and the average lifetime is calculated by calculating the slope of the plot of log *I(t) vs. t*. The other technique used is the frequency-domain measurement where the sample is excited with intensity-modulated light varied at high frequency typically of the order of MHz so that its reciprocal becomes comparable to the reciprocal of the decay time of the sample.

With the technology advancements it is now possible to create images for a lifetime using fluorescence lifetime imaging microscopy (FLIM) which has gained significant popularity in biological sciences. The underlying principle of FLIM is based

on the image contrast for different lifetimes that are presented on a color scale with height representing the local delay times (22). FLIM measurements are independent of concentrations of fluorophores and their corresponding intensities; the color contrast is purely based on the different decay times of donors, and acceptors mixed together in a complex environment. FLIM can be used to record images both in time and frequency domains similar the time-resolved spectroscopy. This technique can be particularly useful for FRET measurements since FRET requires the transfer of energy from a donor to acceptor decreasing donor's lifetime while increasing the lifetime of acceptors. The lifetime difference occurring due to the transfer of energy can thus be easily recorded using FLIM even in the presence of multiple donors and acceptors where local image contrast can provide information regarding lifetimes of each donor and surrounding acceptors.

Though useful, FLIM measurements are slow compared to the timescale of molecular diffusion due to its characteristics of point-to-point measurements that may alter the molecular makeup of an image pixel during measurement (21). Additionally, FLIM is limited to determine stoichiometry only for dimers since it relies on averaging signals from several pixels in order to increase signal to noise ratio. For a system containing higher order oligomers than dimers, averaging over multiple pixels results in accumulation of large number of lifetimes coming from oligomers with different size and shape; due to this effect it is almost impossible to fit the experimental data with multiple exponential decay functions (23).

2.3.3 Fluorescence correlation spectroscopy

Fluorescence correlation spectroscopy (FCS) is an advanced spectroscopic technique that has recently found great interest in the field of biochemistry, biophysics, and biotechnology. FCS is based on time-dependent fluctuations of fluorophores in a small volume of the sample under thermal equilibrium (24). Unlike, fluorescence spectroscopy, the parameter of interest for FCS is not the emission intensities of fluorophores, but the spontaneous fluctuations in the emission intensities occurring due to the physical and chemical changes of the sample of interest. Due to the high sensitivity of the measurement, FCS cannot be performed on samples with a high concentration and large volume. The typical focal volume used for the measurement is about one femtoliter (25) and the typical concentrations ranging from 10^{-9} M – 10^{-6} M. The general principle underlying the FCS technique is to measure intensity fluctuation over time; the rate of the intensity fluctuation depends on the fluorophore diffusion rate. If the rates of fluorophore diffusion are high, a rapid increase and decrease in the fluorescent emission intensity is observed, while if the diffusion rate is slow, fluctuations are observed to be slower. The autocorrelation function is usually calculated by the amplitude and speed of the fluctuations which carries information on relative weights and characteristics time scales of different transitions in the system (25). The height of the correlation function vs. correlation time curve is used to calculate the average number of fluorophores as they are inversely proportional to each other while the diffusion coefficients of fluorophores are estimated by the position curve on time axis.

The technique of Förster resonance energy transfer (FRET) technique is well known for the study of conformational changes in proteins and has found significant promise in the field of biological sciences. Since FRET's sensitivity to distance is high (in the order of sixth power), continuously changing distances between FRET pairs (donors and acceptors) can lead to fluctuations in the emission intensities occurring due to the different amount of energy transfers between donors and acceptors. Because of this, the techniques of FCS and FRET appear to complement one another well. Torres *et al* used FCS technique to study the fluctuations caused in FRET due to continually changing distances and had demonstrated the promise of the FCS-FRET method to study the conformational dynamics of biomolecules (26). Though promising, this method suffers from several challenges that still needs to be addressed. Along with the samples containing the FRET pair, the FCS-FRET measurement requires an identical sample containing the donor molecule. The measurement of both samples must be performed under identical optical conditions with precisely controlled confocal volume for each sample. This task has proved to be difficult in practice, limiting the large scale applications of FCS.

2.3.4 Spectral imaging with linear unmixing

In FRET spectral imaging is a branch of imaging techniques where a complete spectrum of the donor and acceptor fluorophore can be acquired at every location of the imaged sample. Spectral imaging coupled with linear unmixing is an improvised version of sensitized emission, which relies only on donor excitation followed by the acquisition of the entire spectrum of donor and acceptor at the same time. Since the measured spectrum

contains signal from both donor and acceptor; spectral unmixing using elementary spectra of the donor and acceptor is required to calculate individual contributions from donors and acceptors (27). Thus using spectral imaging, it is possible to acquire complete spectral information at once instead of using sets of filters for different bandwidth regions for donors and acceptors, hence it is widely used in the field of FRET biosensors and the study of oligomerization and dynamics of protein-protein interaction (28-31). Also, this method contributes significantly to overcome spectral bleed-through, spectral cross-talk and cellular autofluorescence that are potential problems in FRET based imaging methods (32). Details about the method of spectral imaging are described in section 2.4.2. While spectral imaging offers significant advantages to FRET spectrometry, the experimental set up requires specialized mode-locked solid state laser for multiphoton excitation that is relatively costly limiting its commercial potential. (23).

2.3.5 Fluorescence polarization imaging

Fluorescence polarization (FP) imaging technique is a very sensitive technique capable of studying the size, folding, and stabilization of proteins as well as the viscosity of cytosols. This technique relies on selective excitation of the fluorophores based on the direction of their dipole moments. Each molecule in a cluster of fluorophores has their respective transition dipole moments oriented in a specific direction to the molecular axis. A certain number of molecules in the group can have their dipole moments arranged in a certain angular distribution that can be excited when polarized light is incident on it. The emissions from these excited molecules also have their emission dipole moments distributed in certain angular range. The change in orientations of excited and emitted

dipole moments provide the measure of anisotropy of the molecules. The emission can be depolarized in many ways. Examples include but are not limited to rotational diffusion and complete randomization. FP imaging is well known to predict the size of proteins (33) where the fluorophores are tagged to the proteins. If a protein is large, it takes a long time to change its conformation, thereby slowing down the rate of emission polarization from the tagged fluorophore. Conversely, if the protein is small, the rate of emission polarization will be faster, providing an accurate detail on the size of the molecule. Additionally, this can also provide information about how a protein folds and reaches its stabilized state (33). On the other hand, if biomolecules are dispersed in a viscous medium, the change in emission polarization rate will be slower compared to the ones in less viscous medium, helping to predict the viscosity of the biomolecular environment.

FP imaging is particularly helpful in homo-FRET measurements. Homo-FRET is defined as FRET occurring between the same species of molecules. The identification of homo-FRET is not possible in spectrally resolved measurements or FLIM, since there is no change in either the emission intensity of the donor or the lifetime of the fluorophore during resonance energy transfer is observed (34). The FP technique is found to be useful in this regard, since the fluorophores that can be excited by polarized light exhibit highly polarized emissions compared to the fluorophore emissions occurring via homo FRET. In biological sciences, detection of homo-FRET is more significant than hetero-FRET since it can allow the study of protein oligomerization, and heterogeneity in lipid-order, in complex cell environment (34). FP techniques can provide misleading results occurring from changes in polarization due to other factors such as the use of high numerical

aperture (NA > 1) objective lens and change in orientation of fluorophores during measurement (35).

2.3.6 Total internal reflection fluorescence microscopy (TIRF)

Total internal reflection fluorescence microscopy (TIRF) is a highly useful technique for studying phenomenon occurring at the cell surface providing useful insights over extracellular, and intracellular events occurring near the cell surface. The significant advantage of TIRF is that it can measure the fluorescence in an extremely thin region at the interface of two media without much background noise. As the name implies, TIRF works on the principle of total internal reflection of incident light. When the light travels from denser to rarer medium, the refracted light bends away from the incidence normal. At a certain angle of incidence the refracted light becomes perpendicular to the normal of incidence; this is called the critical angle. At angles larger than the critical angle, all incident light gets totally reflected back into the same medium; this is referred to as total internal reflection. Even though the light undergoing total internal reflection does not enter into the second medium, it does generate an exponentially decaying electric field in the lower refractive index medium adjacent to the interface of two media called as an evanescent wave (36). The generated field has the same frequency as the incident light. These evanescent wave has a penetration depth of ~ 100 nm and can excite a fluorophore which resides in the vicinity of the interface without affecting the molecules far from the interface eliminating the background. Recently, TIRF microscopy has been combined with FRET to both develop biosensors, and study the interactions of G-protein coupled receptors both *in vivo* and *in vitro* (37, 38). Although TIRF incorporated in two-photon

microscopy is an excellent tool to investigate dynamics of many proteins and small molecules on the cell surface with high resolution, its application is limited only to surface the of a cells.

2.4 Linear and non-linear optical microscopy

2.4.1 Single photon vs. multi-photon excitation

The most commonly known absorption phenomena in spectroscopy is single photon absorption where a photon with energy in the UV or visible region is used to excite electrons from the ground state to the excited state. If the energy of one photon is equivalent to the energy gap between the ground and excited state, it is said to be absorbed by the system i.e.,

$$E_f - E_i = \frac{hc}{\lambda_A} \tag{2.2}$$

where E_f is the energy of the excited state $|f\rangle$, E_i is the energy of ground state $|i\rangle$, h is Planck's constant, c is the speed of light, and λ_A is the excitation wavelength as shown in Fig 2.3a. When the single photon in the system is replaced by two photons of less energy (with equal or unequal wavelength) whose sum adds up to the energy gap of the molecule, a similar excitation as single photon is observed but with less energetic photons, this phenomenon is known as two-photon absorption. The corresponding transition is given as:

$$E_f - E_i = \frac{hc}{\lambda_{A1}} + \frac{hc}{\lambda_{A2}} \tag{2.3}$$

where λ_{A1} and λ_{A2} are the excitation wavelengths of two photons.

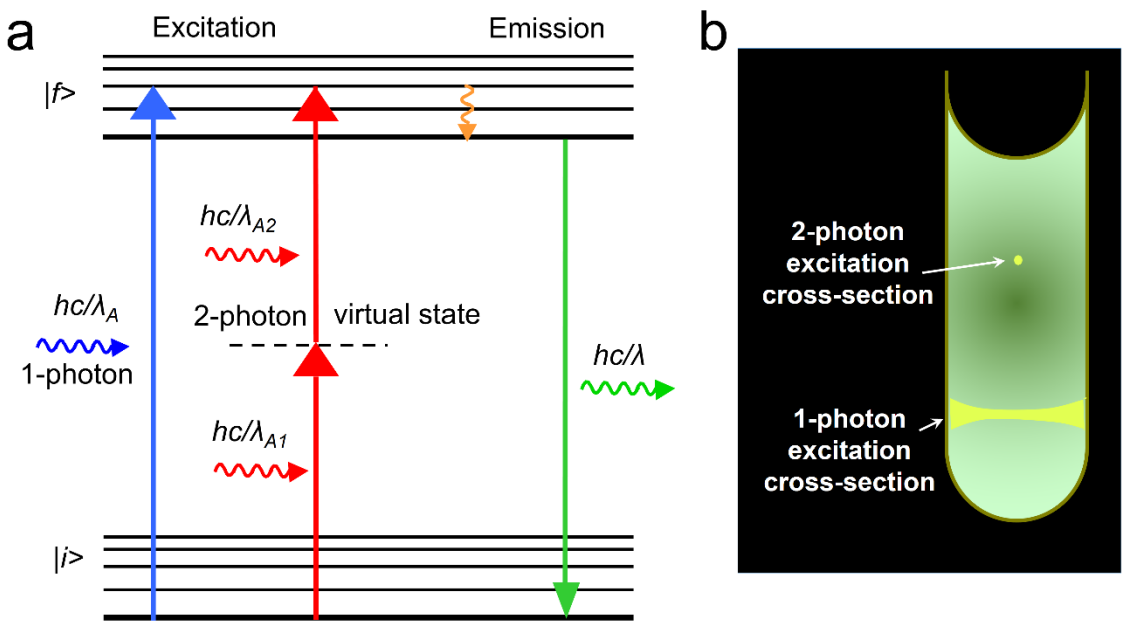

Figure 2.3 Representation of single and two photon excitation energy level diagram and absorption cross section. (a) Energy level diagram of a molecule. $|\boldsymbol{i}\rangle$, and $|\boldsymbol{f}\rangle$, represent ground and first excited state of the molecule, respectively. Solid arrows represent single (blue) and two (red) photon absorption and emission (green). (b) Schematic to show single and 2-photon excitation cross-section shown by bright green color of a solution of fluorescence molecules color in a transparent tube represented by dark green color.

Two-photon absorption, however, depends on the intensity of the incident light, which is supposed to be significantly high for the phenomenon to occur. The strength of absorption is proportional to the square of the incident photon intensity that is parabolic in behavior and hence is a non-linear absorption process. The absorption coefficient of one-photon absorption is given by the Beer Lambert's law, which is

$$I = I_0 e^{-\alpha c x} \tag{2.4}$$

where I_0 is the intensity of incident light, α is the absorption coefficient (cross-section), c is the concentration and x is the light path length, whereas for the two-photon absorption the Beer Lambert's law changes to:

$$II = \frac{I_0}{1 + \beta c x I_0} \tag{2.5}$$

where β is the two-photon absorption coefficient (cross-section). The one-photon absorption cross-section is measured in the units of cm^2 while two-photon absorption cross-section is measured in GM (Göppert-Mayer) unit where, 1GM = 10^{-50} cm^4-sec/photon.

The transition probabilities of single-photon and two-photon absorptions are provided by the following equations (39):

$$P_{one-photon} \sim \left|\langle f|\vec{E}_\gamma.\vec{r}|i\rangle\right|^2 \tag{2.6}$$

and

$$P_{two-photon} \sim \left|\sum_m \frac{\langle f|\vec{E}_\gamma.\vec{r}|m\rangle\langle m|\vec{E}_\gamma.\vec{r}|f\rangle}{\varepsilon_\gamma - \varepsilon_m}\right|^2 \tag{2.7}$$

where $\vec{E}_\gamma.\vec{r}$ is electric dipole interaction energy, $|i\rangle$, $|f\rangle$, and $|m\rangle$ are the initial, final, and intermediate states respectively, ε_γ and ε_m are the photon energies corresponding to the field $\vec{E}_\gamma$ and the energy difference between m^{th} state and the ground state respectively.

There are several advantages of two-photon absorption (TPA) microscopy compared to single-photon absorption (SPA) confocal microscopy (39, 40):

(i) TPA microscopy uses photons with wavelengths in the near infrared region which are significantly less absorbed by biological tissues compared to UV, and visible wavelengths. Therefore, attenuation of excitation light from scattering is reduced because scattering cross-sections decreases with increasing wavelength. The low absorption of infrared light by the biological samples can also help to probe the sample with increased depth.

(ii) Since TPA cross-section is smaller compared to SPA cross-section, therefore, the absorption occurs only at the focal plane of the sample (see Fig. 2.4b). Hence, better resolution is obtained along with reduced photobleaching, and photodamage commonly observed with the SPA confocal microscopy.

(iii) TPA can also help in rejection of excitation light as well as Raman scattering since it uses two photon excitation wavelengths, which is nearly half the excitation wavelength of single photon ensuring wide separation between excitation, and emission wavelengths.

(iv) TPA microscopy doesn’t need a pinhole aperture to reject out-of-focus light, thereby minimizing signal loss, which is significant in SPA confocal microscopy.

While TPA microscopy presents several advantages, it also suffers from a few disadvantages. For instance, TPA suffers from lower spatial resolution when compared to confocal microscopy. Also, it lacks versatility because confocal microscopy can generate images based on refractive index variation in addition to the fluorophore distribution,

which is not possible through TPA microscopy. Nevertheless, TPA has found promising applications in biological sciences such as in physiology, neurobiology, embryology, and tissue imaging and it is expected that future applications can be even more promising. For example, in the field of cellular biology, TPA can potentially be used for noninvasive optical biopsy procedure which that require high speed imaging (40).

2.4.2 Two-photon optical micro-spectroscope (OptiMiS)

Fig. 2.4 shows a schematic of a two-photon optical micro-scope (OptiMiS) system designed and built in our lab. The components of the system include a solid state laser (Verdi^{TM}, coherent Inc., CA, USA., 532 nm), sub-ten femtosecond pulsed Ti: Sapphire laser (KM labs, CO, USA, wavelength range 780-860 nm with FWHM of 120 nm), fixed mirrors, a telescope, computer-controlled orthogonal x-y scanning mirrors (Nutfield Technology Inc., NH, USA), scanning lens, short pass dichroic mirror, relay lens, band-pass filter (1 nm bandwidth), transmission grating, short pass filter, an EM-CCD camera, tube lens, infinity corrected oil immersion objective (Nikon Instruments Inc. NY, 100X magnification, N.A. = 1.43) and x-y-z sample stage.

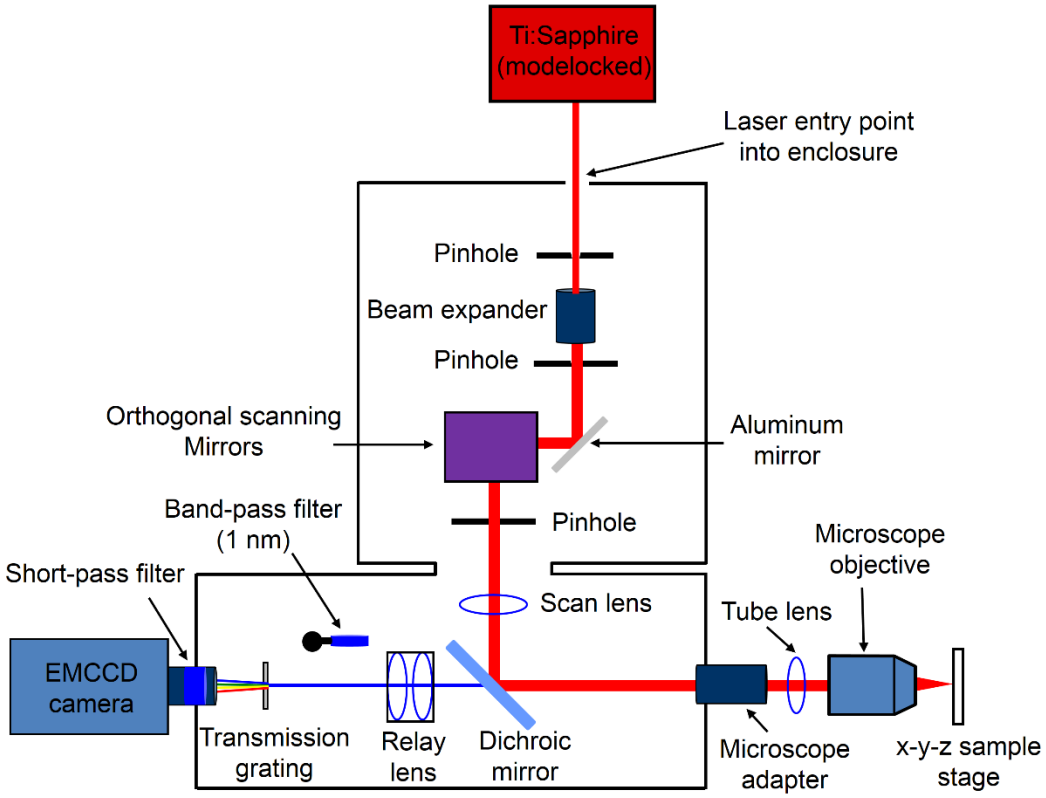

Figure 2.4 Schematic of an optical micro-spectroscope (OptiMiS). The optical components of the microscope are indicated in the figure. The schematic is reconstructed from (27, 41)

As shown in the illustration, the Ti:Sapphire laser generating sub-ten femtosecond pulses of near infra-red (NIR) light (780-860 nm) which after passing through the beam expander is directed to the computer controlled x-y scanning mirrors through a fixed mirror. The light beam is directed by the scanning mirrors before being reflected by the short pass dichroic mirror. The beam is focused to a diffraction-limited spot on the sample by an infinity corrected objective. The back propagating fluorescence generated at every single voxel of the sample is collected by the objective and passes through the short pass dichroic mirror, which allows the passage of fluorescent light having shorter wavelength , 660 nm, through it and reflects back the infrared light that is

reflected back from the sample. The fluorescent light passing through the dichroic mirror then passes through a relay lens to the transmission grating which disperses the light into its spectral components, and then finally falls on the detector (EM-CCD camera). The short pass filter attached to the camera rejects any residual infrared light back propagated along with the fluorescent light. The spot is then scanned over the sample by moving the computer-controlled x-y scanning mirrors. The spectral component of the fluorescence emission from each of the scanned spots in the sample form a line on the detector along one direction (referred to as the y-direction hereafter) after passing through the transmission grating. Thus after scanning the entire x-range (line), the detector provides a 2D image for each line scanned on the sample. The x-dimension of the sample corresponds to the actual x-dimension of the sample while the y-dimension corresponds to the spectral dimension i.e. the wavelength (λ). Many line scans are then performed with different y-values and scanned throughout the sample using x-y scanning mirrors. The individual images corresponding to each line scan is then reconstructed to obtain the final spectral image.

There are several advantages of the OptiMiS setup. First, the fast acquisition of an entire spectrally resolved image requires only a single laser scan of the sample, since the whole spectrum corresponding to each x-line scan is acquired at once. Second, the capability to perform transmission based imaging; the setup uses a halogen lamp placed above the microscope slide and a narrow-band interference filter inserted in the light path before the transmission grating helping to remove the blur caused by diffraction grating. Third, better signal to noise ratio because the number of photons reaching the detector is

larger than the number of photons in other two-photon confocal microscope using pinholes since signals are cut by pinholes. The second generation of OptiMiS utilizes a line scan rather than a point scan by replacing the x-scanning mirror with a cylindrical mirror; this allows the entire x range of the sample to be illuminated with the excitation beam simultaneously, rather than scanning each pixel. This recent development of true-line scan improve the speed and sensitivity by two orders of magnitude while conserving the spectral information (42). The image reconstruction algorithm was written in C++ and is described in section 2.4.4.

2.4.3 Spectral calibration

Spectral calibration is an important step for the accurate interpretation of the data. As described in section 2.4.2, y-pixels correspond to spectral dimension. Therefore, in order to reconstruct the real image from the snapshots taken at different y-pixels, it is critical to assign the correct wavelength to each y-pixel. Thus, the microscope must be calibrated using a standard sample with known fluorescence emission spectrum before data acquisition. The standard sample is an aqueous solution of 2 mM fluorescein sodium salt (Uranine, Fischer Scientific, IL). The full set of x-line scans is performed on the standard sample where the scanning parameter Δy is adjusted based on previous knowledge such that the shift in the spectrum is one pixel for every y-increment of x-y scanning mirror position. The obtained images are then reconstructed using a reconstruction algorithm described in section 2.4.3 and the reconstructed image is processed in ImageJ utilizing inbuilt ascending order and stacked functions for background correction. In order to double check the correct assignment for the value of Δy, we sampled the measured

spectrum of the uranine scan at three different regions (generally the top, middle and bottom) of the reconstructed images. Non-overlapping spectrum or shifted spectrum at different regions indicates incorrect value of Δy and hence the value of Δy is adjusted until the spectrum of fluorescein at all three regions of the reconstructed image overlap perfectly with one another. Knowing that the y (spectral) pixels positions in the camera is linearly related to the wavelength of the emitted photons, a linear relationship between the reconstructed image and the corresponding wavelength was established having following relationship

$$\lambda_i = m(i - i_{max}) + \lambda_{max} \tag{2.8}$$

with

$$m = \frac{(\lambda_{max} - \lambda_{1/2})}{(i_{max} - i_{1/2})} \tag{2.9}$$

where, λ_i corresponds to the ith wavelength of reconstructed image, λ_{max} and $\lambda_{1/2}$ are maximum and half maximum wavelengths of the emission intensities of fluorescein respectively, and i_{max} and $i_{1/2}$ are the reconstructed image numbers corresponding to maximum and the half maximum intensities of the fluorescence.

2.4.4 Image reconstruction

The real spectral images were obtained by using a simple reconstruction algorithm after a correlation of wavelengths with y-pixel was determined. The algorithm steps are described using Fig. 2.5. Each image represents full ‘x’ line scan, the laser being centered

at a particular y-pixel (i.e. wavelength). Each row in the 'y', or spectral dimension represents a wavelength. The entire spectral range is divided into 10 equally spaced wavelengths separated by Δy. Therefore spectral resolution is determined by wavelength value corresponding to Δy pixels. The highest spectral resolution is set to be 1 nm, however for faster acquisition, spectral resolution can be decreased by increasing Δy in the integral increment as required. The x-line scans are performed after each increment of Δy within the scanning range starting from top to bottom along the y-direction. As shown in Fig. 2.5a, let us assign the wavelengths as λ_1, λ_2, λ_3 ,…., λ_{10} for the first line-scan represented by Image#1. After the x-y scanning mirror is moved by an increment of Δy in y-direction, the first wavelength in Image#2 corresponds to the second wavelength in image#1 and so on. Thus, in order to reconstruct the image of entire scanning region at a particular wavelength, rows from all the images corresponding to the wavelength needed to be stacked. For e.g., to reconstruct the image for wavelength, λ_5, rows corresponding to wavelength λ_5 from all the images are stacked as shown in Fig. 2.5b. Fig 2.5c shows an example of the reconstructed image of a CHO cell expressing Cerulean at a certain wavelength as represented by λ_5. Thus reconstructed algorithm provides spectrally resolved images at various wavelengths, which are further processed for calculation of FRET parameters.

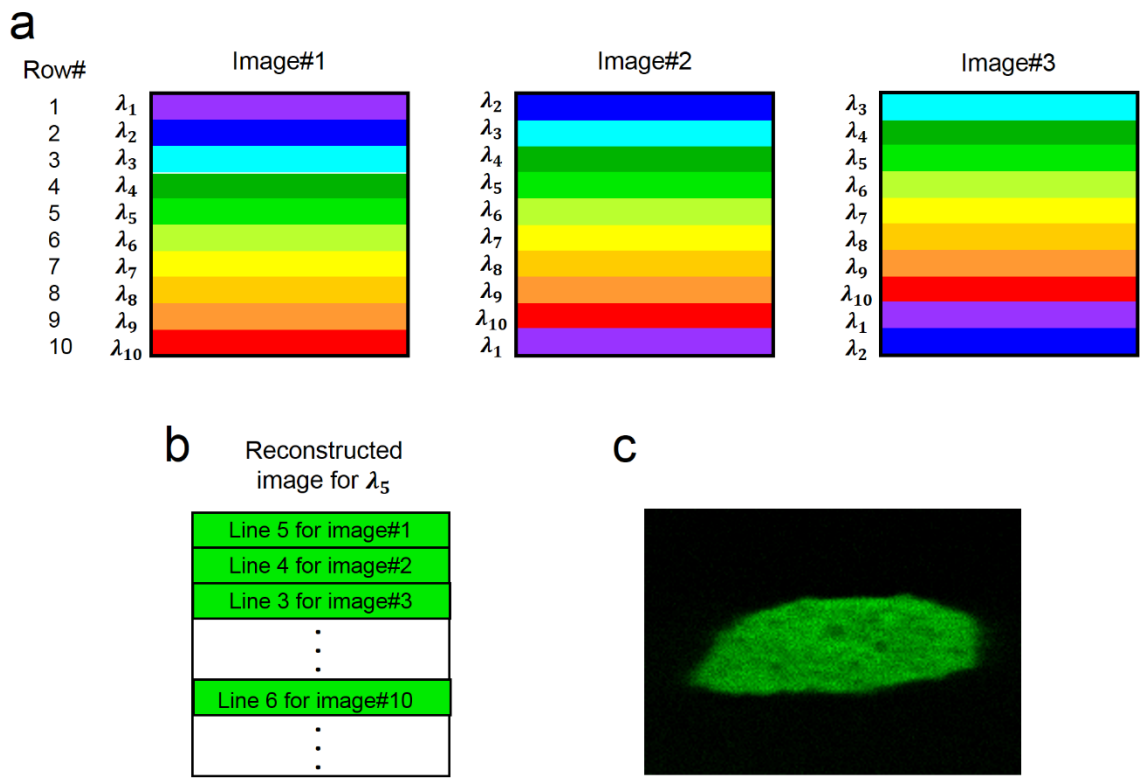

Figure 2.5 Visualization of image reconstruction algorithm from the individual scans. **(a)** Scanning algorithm showing three consecutive images for entire x-scanning range at three consecutive y-centers of focused laser. Row number defines different equally spaced wavelengths of separation, $\boldsymbol{\Delta y}$. **(b)** Reconstruction algorithm of image for a certain wavelength, $\boldsymbol{\lambda_5}$. **(c)** Reconstructed images of a CHO cell expressing Cerulean at a certain wavelength, $\boldsymbol{\lambda_5}$.

References

1. Ormo M, et al. (1996). Crystal structure of the Aequorea victoria green fluorescent protein. *Science* 273(5280):1392-1395.

2. Shimomura O, Johnson FH & Saiga Y (1962). Extraction, purification and properties of aequorin, a bioluminescent protein from the luminous hydromedusan, Aequorea. *J Cell Comp Physiol* 59:223-239.

3. Tsien RY (1998). The green fluorescent protein. *Annu Rev Biochem* 67:509-544.

4. Lakowicz JR (2006). Principles of Fluorescence Spectroscopy (Springer, New York).

5. Wikipedia-contributors (Green fluorescent protein, Wikipedia, The Free Encyclopedia,

http://en.wikipedia.org/w/index.php?title=Green_fluorescent_protein&oldid=565829146.

6. Kain MCSR (2006). Green Fluorescent Protein: Properties, Applications, and Protocols (Wiley-Interscience, Hoboken, NJ).

7. Kremers GJ, Gilbert SG, Cranfill PJ, Davidson MW & Piston DW (2011). Fluorescent proteins at a glance. *J Cell Sci* 124(Pt 2):157-160.

8. Tsien RY (1998). The green fluorescent protein. *Annu Rev Biochem* 67:509-544.

9. Heim R, Prasher DC & Tsien RY (1994). Wavelength mutations and posttranslational autoxidation of green fluorescent protein. *Proc Natl Acad Sci U S A* 91(26):12501-12504.

10. Pollok BA & Heim R (1999). Using GFP in FRET-based applications. *Trends Cell Biol* 9(2):57-60.

11. Truong K & Ikura M (2001). The use of FRET imaging microscopy to detect protein-protein interactions and protein conformational changes in vivo. *Curr Opin Struct Biol* 11(5):573-578.

12. Zimmermann T, Rietdorf J, Girod A, Georget V & Pepperkok R (2002). Spectral imaging and linear un-mixing enables improved FRET efficiency with a novel GFP2-YFP FRET pair. *FEBS Lett* 531(2):245-249.

13. Mizuno H, Sawano A, Eli P, Hama H & Miyawaki A (2001). Red fluorescent protein from Discosoma as a fusion tag and a partner for fluorescence resonance energy transfer. *Biochemistry* 40(8):2502-2510.

14. Dexter DL (1953). A Theory of Sensitized Luminescence in Solids. *J Chem Phys* 21:836-853.

15. Takanishi CL, Bykova EA, Cheng W & Zheng J (2006). GFP-based FRET analysis in live cells. *Brain Res* 1091(1):132-139.

16. Heim R & Tsien RY (1996). Engineering green fluorescent protein for improved brightness, longer wavelengths and fluorescence resonance energy transfer. *Curr Biol* 6(2):178-182.

17. Chen H, Puhl Hr, Koushik S, Vogel S & Ikeda S (2006). Measurement of FRET efficiency and ratio of donor to acceptor concentration in living cells. *Biophys J* 91(5):L39-41.

18. Miyawaki A & Tsien RY (2000). Monitoring protein conformations and interactions by fluorescence resonance energy transfer between mutants of green fluorescent protein. *Methods Enzymol* 327:472-500.

19. Stryer L (1978). Fluorescence energy transfer as a spectroscopic ruler. *Annu Rev Biochem* 47:819-846.

20. Clegg RM (1996). Fluorescence Resonance Energy Transfer. Fluorescence Imaging Spectroscopy and Microscopy, eds Wang XF & Herman B (Wiley-Interscience, New York), Vol 137.

21. Ishikawa-Ankerhold HC, Ankerhold R & Drummen GP (2012). Advanced fluorescence microscopy techniques--FRAP, FLIP, FLAP, FRET and FLIM. *Molecules* 17(4):4047-4132.

22. Cole MJ, et al. (2001). Time-domain whole-field fluorescence lifetime imaging with optical sectioning. *J Microsc* 203(Pt 3):246-257.

23. Valerica Raicu DRS (2013). FRET Spectrometry: A New Tool for the Determination of Protein Quaternary Structure in Living Cells. *Biophys J* 105(9):1937-1945.

24. Schwille P (2001). Fluorescence correlation spectroscopy and its potential for intracellular applications. *Cell Biochem Biophys* 34(3):383-408.

25. Bonnet OKaG (2002). Fluorescence correlation spectroscopy: the technique and its applications. *Rep Prog Phys* 65(251).

26. Torres T & Levitus M (2007). Measuring conformational dynamics: a new FCS-FRET approach. *J Phys Chem B* 111(25):7392-7400.

27. Raicu V, et al. (2009). Determination of supramolecular structure and spatial distribution of protein complexes in living cells. *Nature Photon* 3(2):107-113.

28. Stoneman M, Singh D & Raicu V (2011). In vivo quantification of G protein coupled receptor interactions using spectrally resolved two-photon microscopy. *J Vis Exp* (47).

29. Singh DR, et al. (2013). Determination of the quaternary structure of a bacterial ATP-binding cassette (ABC) transporter in living cells. *Integr Biol* 5(2):312-323.

30. Patowary S, et al. (2013). The muscarinic M3 acetylcholine receptor exists as two differently sized complexes at the plasma membrane. *Biochem J* 452(2):303-312.

31. Woehler A (2013). Simultaneous quantitative live cell imaging of multiple FRET-based biosensors. *Plos One* 8(4):e61096.

32. Xu H & Rice BW (2009). In-vivo fluorescence imaging with a multivariate curve resolution spectral unmixing technique. *J Biomed Opt* 14(6):064011.

33. Piston DW & Rizzo MA (2008). FRET by fluorescence polarization microscopy. *Methods Cell Biol* 85:415-430.

34. Ghosh S, Saha S, Goswami D, Bilgrami S & Mayor S (2012). Dynamic imaging of homo-FRET in live cells by fluorescence anisotropy microscopy. *Methods Enzymol* 505:291-327.

35. Sun Y, Rombola C, Jyothikumar V & Periasamy A (2013). Forster resonance energy transfer microscopy and spectroscopy for localizing protein-protein interactions in living cells. *Cytometry A* 83(9):780-793.

36. Axelrod D (2008). Chapter 7: Total internal reflection fluorescence microscopy. *Methods Cell Biol* 89:169-221.

37. Shen K, Arslan S, Akopian D, Ha T & Shan SO (2012). Activated GTPase movement on an RNA scaffold drives co-translational protein targeting. *Nature* 492(7428):271-275.

38. Boyer SB & Slesinger PA (2010). Probing novel GPCR interactions using a combination of FRET and TIRF. *Commun Integr Biol* 3(4):343-346.

39. So PT, Dong CY, Masters BR & Berland KM (2000). Two-photon excitation fluorescence microscopy. *Annu Rev Biomed Eng* 2:399-429.

40. So PT (2002). Two-photon Fluorescence Light Microscopy, Macmillan Publishers Ltd, Nature Publishing Group, http://www.els.net/.

41. Stoneman MR, et al. (2012). Quantifying the efficiency of various FRET constructs using OptiMiS (TM). *Biotechniques* 52(3):191-195.

42. Biener G, et al. (2013). Development and Experimental Testing of an Optical Microscopic Technique Incorporating True Line-Scan Excitation. *Int J Mol Sci (under review)*.

Chapter 3. Experimental verification of Förster Resonance Energy Transfer (FRET) theory using optical micro-spectroscopy (OptiMiS) and fluorescence reference standards

Förster Resonance Energy Transfer (FRET) is a radiationless photophysical process of energy transfer from an excited donor (D) to its nearby (< 10 nm) acceptor (A) via dipole-dipole interaction (1-3). The theory that describes this process, introduced by Förster (4-6), has so far been widely used and confirmed in particular with regard to the dependence of the efficiency of energy transfer (FRET efficiency) from D to A on the sixth power of the distance between D and A (2, 3). By inserting fluorescent proteins (FP), which can act as D and A, at particular locations of the protein of interest, the distance between the tags and hence between the interacting parts of the proteins can be determined. This approach is used to study associations of macromolecules such as proteins (7-9). However, generalizing and testing the FRET theory for oligomeric complexes containing multiple donors and acceptors has only become possible in recent years (10-12). Therefore, many aspects of it are yet to be investigated. Koushik et al. (13) reported that kinetic theory of FRET failed to predict the ensemble FRET efficiency of oligomers. To this end this chapter deals with an overview of the FRET theory (9, 10) and also testing the kinetic theory of FRET for linked fluorescent proteins that form dimeric, trimeric, and tetrameric combinations located in the cytoplasm or at the plasma membrane. The cytoplasmic probes were fused combinations of a donor (Cerulean, C), an acceptor (Venus, V), and a chromophore-deficient Venus-like molecule that cannot absorb or transfer energy (Amber, A) namely, ACVA, VCAA, ACAV, and VCVV respectively (13). The membrane-bound probes, developed in house, were fused dimers

and trimers of GFP_2 (or G_2, for short) (14) and YFP (or Y) (15) which we call here G_2Y, YG_2, and YG_2Y. The FRET efficiencies for all the dimer, trimer, and tetramer constructs were measured experimentally using an optical micro-spectroscopic (OptiMiS) system (12, 16). According to the theory (10), the FRET efficiency of a tetramer with multiple donor and acceptors such as VCVV can be predicted from that of analogues that contain a single donor and acceptor (e.g., ACVA, ACAV, and VCAA); also, the apparent FRET efficiency of a trimer such as YG_2Y can be predicted from the pair-wise FRET efficiency that corresponds to that of dimers such as G_2Y and YG_2. By comparing the measured and predicted FRET efficiencies, we are able to test the generality of all the aspects of the FRET theory describing multimeric complexes.

3.1 Overview of FRET theory

In recent years, quantitative FRET studies have evolved in mainly two directions: (1) estimation of intermolecular distances between interacting proteins in a protein complex from the energy transfer efficiency and Förster distance; (2) determination of the stoichiometry or the quaternary structure of protein complexes by measuring intensities of donor and acceptor in presence and absence of FRET. In the first type of application, FRET efficiencies of protein complexes can be obtained from measurements of fluorescence intensity (17) as well as from fluorescence lifetime imaging (3, 18). The second line of investigation, is based on fluorescence intensity measurements, which have recently evolved into a method for stoichiometry and quaternary structure determinations of protein complexes in living cells (12). The DNA of the proteins of

interest is fused to the genes of the fluorescent proteins and inserted into cells for expression of the corresponding fusion proteins.

3.1.1 FRET efficiency for dimeric complexes

In this section, we will overview the elementary theory of FRET, with an aim to derive expressions for FRET efficiencies of oligomeric complexes. For simplicity, let us first consider a donor-acceptor pair. In the absence of FRET, an optically excited fluorophore loses some of its excitation energy through vibrational relaxation and comes to the lowest vibrational energy level of the excited state from where it can be de-excited to the ground state either through radiative or non-radiative emissions. The quantum yield of the fluorophore, i.e., the rate of photon emission by the excited fluorophore can be expressed as (9, 10):

$$Q^X = \frac{\Gamma^{r,X}}{\Gamma^{r,X} + \Gamma^{nr,X}} \tag{3.1}$$

where $\Gamma^{r,X}$ and $\Gamma^{nr,X}$ are the rates of radiative and non-radiative energy transfer of excited fluorophore, respectively; X stands for either donor (D) or acceptor (A). The lifetime of the fluorophore can also be defined in terms of the de-excitation rate constants as:

$$\tau^X = \frac{1}{\Gamma^{r,X} + \Gamma^{nr,X}} \tag{3.2}$$

When an acceptor molecule is located in the vicinity of an excited donor, another possible pathway for de-excitation of the donor is through FRET. In this case, the donor is de-excited to its ground state by transferring its energy non-radiatively, through interaction between its transition dipole, and a dipole induced into the nearby acceptor. The quantum yield (Q^{DA}) and lifetime (τ^{DA}) of donor in presence of FRET can be expressed, by modifying equations 3.1 and 3.2, as follows:

$$Q^{DA} = \frac{\Gamma^{r,D}}{\Gamma^{r,D} + \Gamma^{nr,D} + \Gamma^{FRET}} \tag{3.3}$$

and

$$\tau^{DA} = \frac{1}{\Gamma^{r,D} + \Gamma^{nr,D} + \Gamma^{FRET}}, \tag{3.4}$$

where Γ^{FRET} is the rate of energy transfer from the excited donor to the unexcited acceptor and can be defined as:

$$\Gamma^{FRET} = (\Gamma^{r,D} + \Gamma^{nr,D})\left(\frac{R_0^6}{r^6}\right) = \frac{1}{\tau^D}\left(\frac{R_0^6}{r^6}\right) \tag{3.5}$$

where R_0 is the Förster distance (i.e., distance between the donor and acceptor for which the energy transfer rate is 50%) and r is the distance between donor and acceptor (2, 3, 19). It is worth mentioning that FRET affects only the excitation of acceptor, while de-excitation of acceptor is independent of the way acceptor gets excited (9). Hence, the quantum yield and lifetime of the acceptor remain unchanged in FRET. The energy

transfer efficiency of the donor excited through FRET can be expressed in terms of the rate constants as:

$$E = \frac{\Gamma^{FRET}}{\Gamma^{r,D} + \Gamma^{nr,D} + \Gamma^{FRET}} \tag{3.6}$$

or,

$$\frac{E}{1-E} = \frac{\Gamma^{FRET}}{\Gamma^{nr,D} + \Gamma^{FRET}} \tag{3.7}$$

Plugging equation (3.5) into equation (3.6) we get,

$$E = \frac{\Gamma^{FRET}}{\frac{\Gamma^{FRET}}{\left(\frac{R_0^6}{r^6}\right)} + \Gamma^{FRET}} = \frac{\left(\frac{R_0^6}{r^6}\right)}{1 + \left(\frac{R_0^6}{r^6}\right)} = \frac{R_0^6}{r^6 + R_0^6} \tag{3.8}$$

while by plugging equations (3.4) and (3.5) into (3.8), we obtain the following expressions for FRET efficiency in terms of the lifetime of excited donors in presence and absence of energy acceptors:

$$E = 1 - \frac{\tau^{DA}}{\tau^{D}} \tag{3.9}$$

Combining equations (3.1) (for X = D) and (3.3) with (3.6), we obtain a relation between the FRET efficiency and the quantum yields of the donor in the presence and absence of acceptor (or FRET):

$$Q^{DA} = Q^{D}(1 - E) \tag{3.10}$$

This equation indicates that the donor emission decreases as a result of the energy transfer to the acceptor.

3.1.2 FRET efficiency for multimeric complexes

Here we will overview a kinetic theory of FRET introduced recently (10). According to that theory, the FRET efficiency of a multimeric complex consisting of donors and acceptors, can be generalized in terms of a pair-wise FRET efficiency, or the efficiency between a certain donor-acceptor pair.

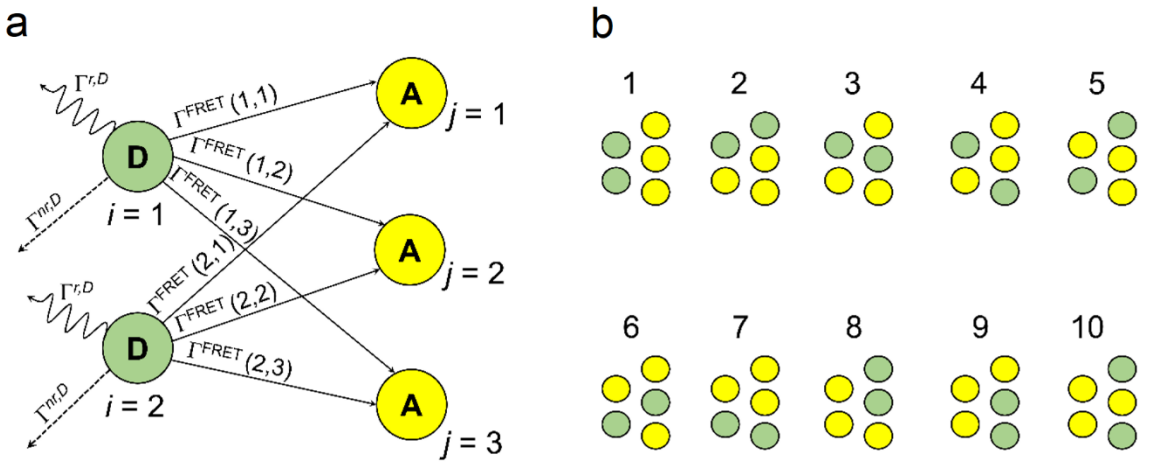

Figure 3.1: Schematic representation of an oligomer (a pentamer in this example) with two donors (D) and three acceptors (A) and their possible configurations. **(a)** Possible energy transfer pathways from the donors to the acceptors in the oligomers. Solid, dashed and wavy arrows represent FRET, radiative and non-radiative energy transfer. **(b)** Ten possible configurations of the pentamer shown in **(a)**. Figure, adapted from (10).

Considering an oligomer containing *n* subunits (or protomers), with *k* of them being identical donors and *n-k* identical acceptors, there exist *k* pathways for the donors to lose excitation energy through radiative emission of a photon or non-radiative de-excitation (due to the interaction with the environment) and *n-k* different ways of losing excitation energy via FRET with nearby acceptors (see Fig. 3.1 (a) as an example of all possible

energy transfer pathways from a pentamer with two donors and three acceptors). If the number of possible configurations of an oligomer is represented by q (see Fig. 3.1 (b), where q = 10), the quantum yield of the i[th] donor can be expressed as (9, 12):

$$Q_{i,k,n,q}^{DA} = \frac{\Gamma^{r,D}}{\Gamma^{r,D} + \Gamma^{nr,D} + \sum_{j=1}^{n-k} \Gamma_{i,j,q}^{FRET}} = \frac{Q^D}{1 + \sum_{j=1}^{n-k} \left(\Gamma_{i,j,q}^{FRET} / \Gamma^{r,D} + \Gamma^{rn,D} \right)} \tag{3.11}$$

where $\Gamma_{i,j,q}^{FRET} = (\Gamma^{r,D} + \Gamma^{nr,D}) \left(R_{i,j,q}^0 / r_{i,j,q}^0 \right)^6$ is the energy transfer rate of i[th] donor to j[th] acceptor through FRET. Since the orientation factor for individual donor-acceptor pairs in an oligomer might be different (2, 3), the Förster distance can also be different for each pair of donors and acceptors. The FRET efficiency for the i[th] donor can be defined as:

$$E_{i,k,n,q} = \sum_{j=1}^{n-k} \frac{\Gamma_{i,j,q}^{FRET} / \Gamma^{r,D} + \Gamma^{rn,D}}{1 + \sum_{j=1}^{n-k} \left(\Gamma_{i,j,q}^{FRET} / \Gamma^{r,D} + \Gamma^{rn,D} \right)} = \sum_{j=1}^{n-k} E_{i,j,q} \tag{3.12}$$

where $E_{i,j,q} = \frac{\Gamma_{i,j,q}^{FRET} / \Gamma^{r,D} + \Gamma^{rn,D}}{1 + \sum_{j=1}^{n-k} \left(\Gamma_{i,j,q}^{FRET} / \Gamma^{r,D} + \Gamma^{rn,D} \right)} = \frac{\left(R_{i,j,q}^0 / r_{i,j,q}^0 \right)^6}{1 + \sum_{j=1}^{n-k} \left(R_{i,j,q}^0 / r_{i,j,q}^0 \right)^6}$ is the FRET efficiency of i[th] donor and j[th] acceptor. Equation (3.12) is also called the kinetic model of FRET. Using equation (3.12), equation (3.11) can also be written as $Q_{i,k,n,q}^{DA} = Q^D \left(1 - E_{i,k,n,q} \right)$, which is similar to equation (3.10).

3.1.3 Experimental determination of FRET efficiency using filter-based methods

The standard experimental method for determining FRET efficiencies of protein complexes using optical filters of a certain bandwidth is described in this section. Fig. 3.2 shows a mixture of two populations of fluorophores consisting of donors and acceptors of energy. When the distances between donors and acceptors are significantly larger than the Förster radius (Fig. 3.2 (a)) and the mixture is subjected to light with wavelength λ_{ex}, which excites the donors significantly and only rarely excites the acceptors, the emission intensity at the emission wavelength of acceptor will provide high signal from the donors and low signal from the acceptors and donors, as shown in Fig. 3.2 (c). If some donors and acceptors are within the range of Förster distance (3), as illustrated in Fig. 3.2 (b), the donors can excite their nearby acceptors by transferring their energy non-radiatively, and the emission intensity at the emission wavelength of acceptors, λ_{em}, will be dominated by acceptor emission as shown in Fig. 3.2 (d). The measured emission intensity can thus be expressed as:

$$I^m(\lambda_{ex}, \lambda_{em}) = I^D(\lambda_{ex}, \lambda_{em}) + I^A(\lambda_{ex}, \lambda_{em}). \tag{3.13}$$

Now, representing the intensity lost by the donor due to FRET and that gained by the acceptor as $I^D(\lambda_{em}, FRET)$ and $I^A(\lambda_{em}, FRET)$, respectively, the above equation may be re-written as:

$$\begin{aligned} I^m(\lambda_{ex}, \lambda_{em}) &= I^{DA}(\lambda_{ex}, \lambda_{em}) + I^{AD}(\lambda_{ex}, \lambda_{em}) \\ &= I^D(\lambda_{ex}, \lambda_{em}) - I^D(\lambda_{em}, FRET) + I^A(\lambda_{ex}, \lambda_{em}) + I^A(\lambda_{em}, FRET) \end{aligned} \tag{3.14}$$

where $I^{DA}(\lambda_{ex}, \lambda_{em})$ and $I^{AD}(\lambda_{ex}, \lambda_{em})$ are the emission intensities of the donor in the presence of acceptors and vice versa.

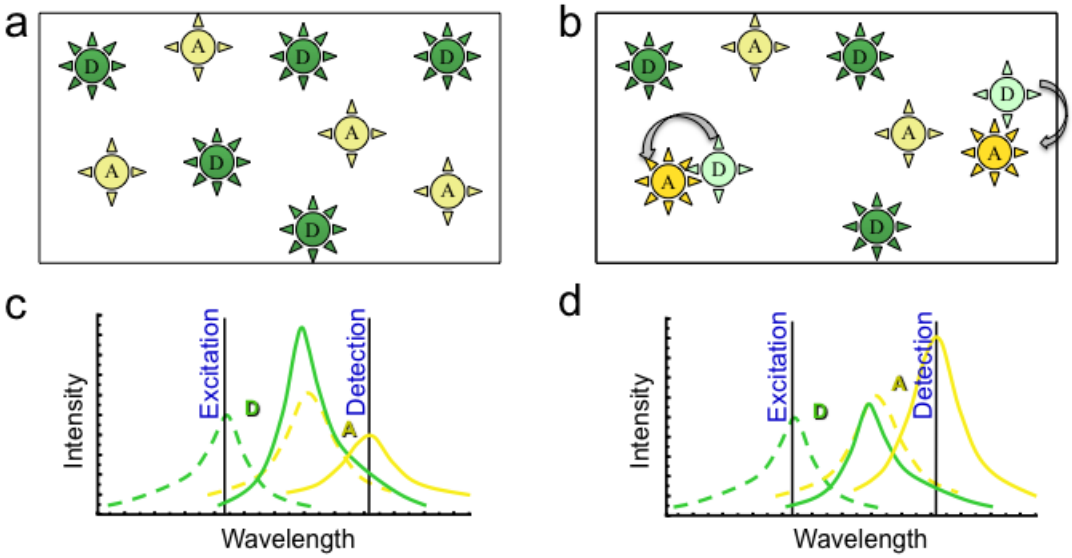

Figure 3.2: Schematic representation of the effect of FRET on a mixture of donors (D) and acceptors (A) excited at the maximum excitation wavelength of the donors. **(a)** Mixture of D and A separated by distances > 10 nm. Donors and acceptors are shown in dark green color and light yellow color respectively representing excitation of the donors and no energy transfer to the acceptors. **(b)** If some donors, and acceptors are within the Förster distance from one another; the donors become dimmer and the acceptor brighter due to energy transfer. **(c), (d)** Excitation (dashed lines) and emission (solid lines) spectra of donors (green) and acceptors (yellow). **(c)** Strong emission peak for donor and weak emission peak for acceptor corresponding to the situation **(a)** results in low signal detected at the emission wavelength of acceptor. **(d)** Weak emission peak for donor while strong emission peak for acceptor corresponding to the situation **(b)** results in detection of high signal. This image is adopted from (9)

Equation (3.14) shows that the measured emission intensity depends on the excitation wavelength. For most of the fluorophores used as good FRET pairs (i.e., for which there is a significant overlap between the emission spectrum of the donor and the excitation spectrum of the acceptor), a relatively short Stokes shifts result in the excitation of acceptors to different degrees at the excitation wavelengths of donor and vice versa. This effect is called spectral cross-talk (20) and should be avoided in FRET

studies. Choosing the FRET pair which has well separated spectrum is a solution to the spectral cross-talk, however, this decreases the spectral overlap integral ($J(\lambda)$) (3) of the fluorophores reducing the ability to detect FRET signals. Many of the intensity-based measurements methods rely on emission and detection filters to measure the fluorescence intensity of one fluorophore in presence and absence of the other. These filter-based methods need at least two different detection wavelengths: one, $\lambda_{em,1}$, at which donor to acceptor emission ratio is maximum (i.e. acceptor emission in negligible) and at other, $\lambda_{em,2}$ where it is minimum (donor emission is negligible). Accordingly, we can approximate equation (3.14) as:

$$I^m(\lambda_{ex},\lambda_{em,1}) \cong I^{DA}(\lambda_{ex},\lambda_{em,1}) = I^D(\lambda_{ex},\lambda_{em,1}) - I^D(\lambda_{em,1},FRET) \qquad (3.15)$$

and

$$I^m(\lambda_{ex},\lambda_{em,2}) \cong I^{AD}(\lambda_{ex},\lambda_{em,2}) = I^A(\lambda_{ex},\lambda_{em,2}) + I^A(\lambda_{em,2},FRET) \qquad (3.16)$$

Equations (3.15) and (3.16) are used to calculate the apparent FRET efficiencies in terms of donor quenching and acceptor sensitized emission (3, 9, 10) as:

$$E_{app}^{Dq} \equiv \frac{I^D(\lambda_{em,1},FRET)}{I^D(\lambda_{ex},\lambda_{em,1})} = 1 - \frac{I^{DA}(\lambda_{ex},\lambda_{em,1})}{I^D(\lambda_{ex},\lambda_{em,1})} \qquad (3.17)$$

$$E_{app}^{Ase} \equiv \frac{I^A(\lambda_{em,2},FRET)}{I^A(\lambda_{ex},\lambda_{em,1})} = \frac{I^{AD}(\lambda_{ex},\lambda_{em,2})}{I^A(\lambda_{ex},\lambda_{em,2})} - 1 \qquad (3.18)$$

The disadvantage of the above method is spectral bleed-through (see detail discussion in section 2.1) (9). Additionally, in order to determine the intensities from donors in the absence of acceptors (I^D) and the acceptors in absence of donors (I^A), one needs to perform acceptor photobleaching and separate measurement of samples containing acceptors only (9, 17), respectively. In the method based on acceptor photobleaching, the donor is also bleached to a certain extent, and this can affect the apparent FRET efficiency determination. Additionally, the same sample cannot be used more than once in experiments relying on acceptor photobleaching, which prevents the applicability of this method to dynamic studies that require monitoring the evolution of the protein complex in time.

3.1.4 Determination of FRET efficiency from spectrally resolved fluorescence intensity measurements

In this section, we will overview the theory of the method of spectrally resolved FRET imaging (12), and we will also introduce an original contribution, which is related to extraction of spectral components from a composite spectrum consisting of three different species of fluorescent molecules.

The proteins of interest are tagged by the fluorescent molecules that act as donors and acceptors and are transfected to the cells. Cells co-expressing both donor and acceptor tagged proteins are excited at the excitation wavelength of donor and emission spectrum is collected at every pixel of the scanning area. In order to extract the donor and acceptor signals from the composite spectrum at every pixel, first we measure the

fluorescence intensities of the samples containing donors only, and acceptors only. The acquired donor and acceptor emission spectra are normalized by their maximum intensity in order to get the elementary spectrum of donors,

$$I^D = \begin{bmatrix} i_1^D & \dots. & i_n^D \\ \lambda_{em,1} & \dots. & \lambda_{em,n} \end{bmatrix} \tag{3.19}$$

and acceptors,

$$I^A = \begin{bmatrix} i_1^A & \dots. & i_n^A \\ \lambda_{em,1} & \dots. & \lambda_{em,n} \end{bmatrix}, \tag{3.20}$$

where $i_{1,\dots.,}i_n$ are the normalized intensities corresponding to the emission wavelengths $\lambda_{em,1,\dots.,}\lambda_{em,n}$ (9) The emission spectrum at every pixel of the image of the sample containing both donors and acceptors may be written as:

$$I^m = \begin{bmatrix} i_1^m & \dots. & i_n^m \\ \lambda_{em,1} & \dots. & \lambda_{em,n} \end{bmatrix} \tag{3.21}$$

or,

$$I^m = \sum_{j=1}^{n} i_j^m = k^{DA}(\lambda_{ex}) \sum_{j=1}^{n} i_j^D + k^{AD}(\lambda_{ex}) \sum_{j=1}^{n} i_j^A \tag{3.22}$$

The parameters k^{DA}, and k^{AD} are the emission intensities for D in the presence of A, and for A in presence of D respectively and is determined using least square method (17, 21). At every pixel the measured intensity i^m is fitted linearly by adjusting the fitting parameters $k^{DA}(\lambda_{ex})$ and $k^{AD}(\lambda_{ex})$. The square of the fitting residual at any pixel is given by

$$R^2 = \sum_{j=1}^{n} \left(i_j^m\right)^2 + \left(k^{DA}(\lambda_{ex})\right)^2 \sum_{j=1}^{n} \left(i_j^D\right)^2 + \left(k^{AD}(\lambda_{ex})\right)^2 \sum_{j=1}^{n} \left(i_j^A\right)^2$$

$$+ 2k^{DA}(\lambda_{ex})k^{AD}(\lambda_{ex}) \sum_{j=1}^{n} i_j^D i_j^A \qquad (3.23)$$

$$- 2\sum_{j=1}^{n} i_j^m \left\{k^{DA}(\lambda_{ex}) i_j^D + k^{AD}(\lambda_{ex}) i_j^A\right\}$$

For the best-fitted curve, the fitting residual should reach a minimum, i.e., the partial derivatives of the square of the fitting residual with respect to the fitting parameters $k^{DA}(\lambda_{ex})$ and $k^{AD}(\lambda_{ex})$ should be zero, i.e., $\frac{\partial(R)^2}{\partial\left(k^{DA}\right)} = 0$ and $\frac{\partial(R)^2}{\partial\left(k^{AD}\right)} = 0$.

Or

$$k^{DA}(\lambda_{ex}) \sum_{j=1}^{n} \left(i_j^D\right)^2 + k^{AD}(\lambda_{ex}) \sum_{j=1}^{n} i_j^D i_j^A - \sum_{j=1}^{n} i_j^m i_j^D = 0 \qquad (3.24)$$

and

$$k^{AD}(\lambda_{ex}) \sum_{j=1}^{n} \left(i_j^A\right)^2 + k^{DA}(\lambda_{ex}) \sum_{j=1}^{n} i_j^D i_j^A - \sum_{j=1}^{n} i_j^m i_j^A = 0. \qquad (3.25)$$

In matrix form the above two equations can be written as:

$$\begin{bmatrix} \sum_{j=1}^{n} \left(i_j^D\right)^2 & \sum_{j=1}^{n} i_j^D i_j^A \\ \sum_{j=1}^{n} i_j^D i_j^A & \sum_{j=1}^{n} \left(i_j^A\right)^2 \end{bmatrix} \begin{bmatrix} k^{DA}(\lambda_{ex}) \\ k^{AD}(\lambda_{ex}) \end{bmatrix} = \begin{bmatrix} \sum_{j=1}^{n} i_j^m i_j^D \\ \sum_{j=1}^{n} i_j^m i_j^A \end{bmatrix}. \qquad (3.26)$$

Therefore, $$\begin{bmatrix} k^{DA}(\lambda_{ex}) \\ k^{AD}(\lambda_{ex}) \end{bmatrix} = \begin{bmatrix} \sum_{j=1}^{n} \left(i_j^D\right)^2 & \sum_{j=1}^{n} i_j^D i_j^A \\ \sum_{j=1}^{n} i_j^D i_j^A & \sum_{j=1}^{n} \left(i_j^A\right)^2 \end{bmatrix}^{-1} \begin{bmatrix} \sum_{j=1}^{n} i_j^m i_j^D \\ \sum_{j=1}^{n} i_j^m i_j^A \end{bmatrix}. \quad (3.27)$$

Solving the above matrix inversion, provides the expressions of each of the fitting parameters as:

$$k^{DA}(\lambda_{ex}) = \frac{\sum_{j=1}^{n} \left(i_j^A\right)^2 \sum_{j=1}^{n} i_j^m i_j^D - \sum_{j=1}^{n} i_j^D i_j^A \sum_{j=1}^{n} i_j^m i_j^A}{\sum_{j=1}^{n} \left(i_j^D\right)^2 \sum_{j=1}^{n} \left(i_j^A\right)^2 - \left(\sum_{j=1}^{n} i_j^D i_j^A\right)^2} \quad (3.28)$$

$$k^{AD}(\lambda_{ex}) = \frac{\sum_{j=1}^{n} \left(i_j^D\right)^2 \sum_{j=1}^{n} i_j^m i_j^A - \sum_{j=1}^{n} i_j^D i_j^A \sum_{j=1}^{n} i_j^m i_j^D}{\sum_{j=1}^{n} \left(i_j^D\right)^2 \sum_{j=1}^{n} \left(i_j^A\right)^2 - \left(\sum_{j=1}^{n} i_j^D i_j^A\right)^2} \quad (3.29)$$

The presence of a third fluorescent dye will modify the expression of the measured intensity as:

$$I^m = \sum_{j=1}^{n} i_j^m = k^{DA}(\lambda_{ex}) \sum_{j=1}^{n} i_j^D + k^{AD}(\lambda_{ex}) \sum_{j=1}^{n} i_j^A + k^F(\lambda_{ex}) \sum_{j=1}^{n} i_j^F \quad (3.30)$$

where k^F is proportional to the emission intensity of the third fluorophore. Proceeding in a similar way as shown above, the fitting parameters corresponding to the lowest fitting residual may be expressed as:

$$k^{DA}(\lambda_{ex}) = \frac{(YZ - R^2)A + (QR - ZP)B + (PR - YQ)C}{XYZ + 2PQR - XR^2 - YQ^2 - ZP^2} \quad (3.31)$$

$$k^{AD}(\lambda_{ex}) = \frac{(QR - ZP)A + (XY - Q^2)B + (PQ - XR)C}{XYZ + 2PQR - XR^2 - YQ^2 - ZP^2} \tag{3.32}$$

$$k^{F}(\lambda_{ex}) = \frac{(RP - YQ)A + (PQ - XR)B + (XY - P^2)C}{XYZ + 2PQR - XR^2 - YQ^2 - ZP^2} \tag{3.33}$$

where $A = \sum_{j=1}^{n} i_j^m \, i_j^D$, $B = \sum_{j=1}^{n} i_j^m \, i_j^A$, $C = \sum_{j=1}^{n} i_j^m \, i_j^F$, $P = \sum_{j=1}^{n} i_j^D \, i_j^A$, $Q = \sum_{j=1}^{n} i_j^D \, i_j^F$, $R = \sum_{j=1}^{n} i_j^A i_j^F$, $X = \sum_{j=1}^{n} i_j^{D^2}$, $Y = \sum_{j=1}^{n} i_j^{A^2}$ and $Z = \sum_{j=1}^{n} i_j^{F^2}$.

The above three quantities can be used to determine the total number of photons emitted by the donor, $F^{DA}(\lambda_{ex})$, the acceptor, $F^{AD}(\lambda_{ex})$, and a third fluorophore, if present, $F^{F}(\lambda_{ex})$, i.e.,

$$F^{DA}(\lambda_{ex}) = k^{DA}(\lambda_{ex}) \int i^{D}(\lambda_{em}) d\lambda_{em} = k^{DA}(\lambda_{ex}) w^{D} \tag{3.34}$$

$$F^{AD}(\lambda_{ex}) = k^{AD}(\lambda_{ex}) \int i^{A}(\lambda_{em}) d\lambda_{em} = k^{AD}(\lambda_{ex}) w^{A} \tag{3.35}$$

$$F^{F}(\lambda_{ex}) = k^{F}(\lambda_{ex}) \int i^{F}(\lambda_{em}) d\lambda_{em} = k^{F}(\lambda_{ex}) w^{F} \tag{3.36}$$

where w^D, w^A, w^F are the integrals of the elementary emission spectra of donor, acceptor, and the third fluorophore.

As we have seen in sections 3.1.1 and 3.1.2., due to FRET, the donor intensity is quenched while acceptor intensity is enhanced; these effects may be expressed mathematically as:

$$F^{DA}(\lambda_{ex}) = F^{D}(\lambda_{ex}) - F_D^{FRET} \tag{3.37}$$

$$F^{AD}(\lambda_{ex}) = F^{A}(\lambda_{ex}) + F_A^{FRET} \tag{3.38}$$

where, the quantities $F^{D}(\lambda_{ex})$ and $F^{A}(\lambda_{ex})$ are the numbers of photons emitted following excitation by light of wavelength λ_{ex}, F_D^{FRET} is the loss in donor emission due to FRET, and F_A^{FRET} is the gain in acceptor emission due to FRET. Therefore, the FRET efficiency can also be defined as the extent to which the donors are quenched by acceptors as a result of FRET, that is:

$$E_{app} = \frac{F_D^{FRET}}{F^{D}(\lambda_{ex})} \tag{3.39}$$

Equations (3.37) and (3.38) can be justified using equation (A.10) and (A.11). If N^{FRET} is the total number of excitations, donor can emit $Q_D N^{FRET} = F_D^{FRET}$ photons in absence of FRET while the acceptor can emit $Q_A N^{FRET} = F_A^{FRET}$ photons in presence of FRET. Therefore we can write,

$$Q_D F_D^{FRET} = Q_A F_A^{FRET}$$

or

$$F_D^{FRET} = \frac{Q_A}{Q_D} F_A^{FRET} \tag{3.40}$$

Assuming that the acceptors are not excited directly by light (i.e., $F^A(\lambda_{ex}) \approx 0$), and using equations (3.37), (3.38) and (3.40), the apparent FRET efficiency equation of a molecular complex is given by the following expression:

$$E_{app} = \frac{1}{1 + \frac{Q^A}{Q^D}\frac{k^{DA}}{k^{AD}}\frac{w^D}{w^A}} \tag{3.41}$$

This equation is used to determine the FRET efficiency at each pixel in a fluorescence image using a single scan o the sample at a single excitation wavelength, and it circumvents difficulties associated with the classical filter-based method described in the previous section.

3.1.5 Apparent FRET efficiency in the presence of direct excitation of the acceptor

To determine the apparent FRET efficiency (equation 3.41) one always aims to choose an excitation wavelength of the laser that excites the donor maximally while minimizing the acceptor excitation. In reality, there is no single wavelength that can excite the donor significantly to detect FRET without exciting acceptor to some extent. Thus, in the presence of non-negligible direct excitation of the acceptor ($i.e., F^A(\lambda_{ex}) \neq 0$), equation (3.41) becomes,

$$E_{app}^{corrected} = \frac{\frac{Q^D}{Q^A}[F^{AD}(\lambda_{ex}) - F^A(\lambda_{ex})]}{F^{DA}(\lambda_{ex}) + F_D^{FRET}}$$
$$= \frac{\frac{Q^D}{Q^A}[k^{AD}(\lambda_{ex})w^A - F^A(\lambda_{ex})]}{k^{DA}(\lambda_{ex})w^D + \frac{Q^D}{Q^A}\{F^{AD}(\lambda_{ex}) - F^A(\lambda_{ex})\}} \quad (3.42)$$

For FRET standards shown in section 3.2 below, k = 1 and $[A] = [D] = 0$, $[A]_A = [D]_D = 0$ and $[A]_D = x\mu_{oligo}$, where x is the number of acceptors linked to donors in a construct. Therefore, the total number of photons emitted by the acceptors excited by laser at wavelength λ_{ex} can be expressed as (10):

$$F^A(\lambda_{ex}) = \Gamma^{ex,A} Q^A \mu_{oligo} n P_A \quad (3.43)$$

Also, the number of photons emitted by the acceptors in presence of FRET can be expressed as:

$$F_A^{FRET} = \Gamma^{ex,AD}[A]_D Q^A, \quad (3.44)$$

Using equations (3.43) and (3.44) we can write:

$$F^{AD}(\lambda_{ex}) = Q^A\{\Gamma^{ex,A}\mu_{oligo} n P_A + \Gamma^{ex,D}\mu_{oligo} E_{app}\} \quad (3.45)$$

From equation (3.35) and (3.45), we can write the concentration of FRET standards in the cells in terms of its apparent FRET efficiency as:

$$\mu_{oligo} = \frac{k^{AD} w^{A}}{Q^{A}\left\{\Gamma^{ex,A} n P_A + \Gamma^{ex,D} E_{app}\right\}} \tag{3.46}$$

Insertion of the above equation into equation (3.43) gives,

$$F^{A}(\lambda_{ex}) = \frac{\Gamma^{ex,A} n P_A k^{AD} w^{A}}{\Gamma^{ex,A} n P_A + \Gamma^{ex,D} E_{app}} = k^{AD} w^{A} \alpha_A \tag{3.47}$$

where $\alpha_A = \frac{\Gamma^{ex,A} n P_A}{\Gamma^{ex,A} n P_A + \Gamma^{ex,D} E_{app}}$. Since the excitation rate constants of donors and acceptors are directly proportional to their respective extinction coefficients ($\varepsilon^{D}, \varepsilon^{A}$), the expression for α_A becomes

$$\alpha_A = \frac{\varepsilon^{A} n P_A}{\varepsilon^{A} n P_A + \varepsilon^{D} E_{app}} = \frac{1}{1 + \frac{\varepsilon^{D}}{\varepsilon^{A}} \frac{1}{n P_A} E_{app}} \tag{3.48}$$

Therefore, equation (3.42) may be written as:

$$\begin{aligned} E_{app}^{corrected} &= \frac{\frac{Q^{D}}{Q^{A}} k^{AD} w^{A} [1 - \alpha_A]}{k^{DA} w^{D} + \frac{Q^{D}}{Q^{A}} \{k^{AD} w^{A} - k^{AD} w^{A} \alpha_A\}} = \frac{1 - \alpha_A}{1 - \alpha_A + \frac{k^{DA}}{k^{AD}} \frac{w^{D}}{w^{A}} \frac{Q^{A}}{Q^{D}}} \\ &= \frac{1}{1 + \frac{k^{DA}}{k^{AD}} \frac{w^{D}}{w^{A}} \frac{Q^{A}}{Q^{D}} \frac{1}{(1 - \alpha_A)}} \end{aligned} \tag{3.49}$$

Let

$$\frac{k^{DA}}{k^{AD}} \frac{w^{D}}{w^{A}} \frac{Q^{A}}{Q^{D}} = c = \frac{1 - E_{app}}{E_{app}}$$

Then, $$E_{app}^{corrected} = \frac{1}{1 + c\frac{1}{1 - \alpha_A}} \quad (3.50)$$

Using a Taylor series expansion for $\alpha_A \ll 1$ (i.e., assuming that the direct excitation of the acceptor is small), equation (3.49) can be simplified to

$$E_{app}^{corrected} = E_{app}[1 - (1 - E_{app})\alpha_A] \quad (3.51)$$

The above equation gives apparent FRET efficiency for configuration sample, which is corrected for direct excitation of the acceptor.

3.2 Materials and methods

3.2.1 FRET standards expressed in the cytoplasm

To test the above FRET theory, we used two different types of FRET constructs, one type that could be expressed in the cytoplasm and one which could be expressed in the membrane of mammalian cells.

The first type of constructs, which were expressed in the cytoplasm were a generous gift from Dr. Steven Vogel (NIH). Fig. 3.3 shows the set of FRET standards engineered by Koushik et al. (13) using Cerulean (22) as a donor, Venus (23) as an acceptor and Amber (24), a Venus like molecule mutated in order to prevent a fluorophore formation and therefore cannot participate in FRET, but was used to mimic the configuration of tetramers while behaving as a dimer in the process of energy

transfer. The tetramers shown in Fig. 3.3 were used in order to test kinetic theory, while a dimer, Amber-5-Cerulean (A5C) was used to obtain the emission spectrum of the donor (Cerulean). The cloning and construction of monomeric fluorescent proteins Cerulean (C), Venus (V) and Amber (A) and artificial dimer Amber-5-Cerulean (A5C) and heterotetramers: Amber-5-Cerulean-5-Venus-6-Amber (ACVA), Venus-5-Cerulean-5-Amber-6-Amber (VCAA), Amber-5-Cerulean-5-Amber-6-Venus (ACAV), Venus-5-Cerulean-5-Venus-6-Venus (VCVV) were described elsewhere (13) where numbers 5 and 6 represent number of amino acids in the linker.

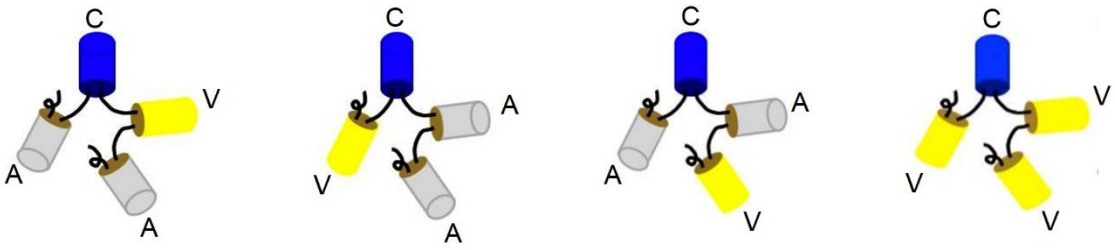

Figure 3.3: Schematic of the cytoplasmic FRET standards. Cerulean (C) as donor linked to the acceptor, Venus (V) and dark Venus like molecule, Amber (A) by amino acid linker shown by curved lines connecting C, V, and A (13).

3.2.2 Generation of monomeric, dimeric and trimeric fluorescent proteins

The second category of constructs, which can be expressed in the membrane of mammalian cells, was developed by our collaborators from the laboratory of Prof. James W. Wells at the University of Toronto. The first 7 residues of the N terminus of the α-subunit type i1 ($G\alpha_{i1}$) in heterotrimeric G proteins (25, 26) comprise a motif (Met-Gly-Cys-Thr-Leu-Ser-Ala) that introduces myristoyl (M) and palmitoyl (P) group at the second and third residues, respectively. The complementary DNA (cDNA) coding for

this sequence, the proceeding 25 residues of $G\alpha_{i1}$ and the 6 bases corresponding to the BamH1 restriction site were fused upstream of the cDNA coding for either GFP2 (MP-GFP2) or eYFP (MP-eYFP). Fluorescent proteins were concatenated through the addition of 6 bases corresponding to the BspE1 restriction site at the 3' end of the former and latter fusions, to create the dimeric variants MP-GFP2-eYFP (G_2Y) and MP-eYFP-GFP2 (YG_2), respectively. A further 6 bases corresponding to the AgeI restriction site were added at the 3' end of MP-eYFP-GFP2 to generate a trimeric variant, MP-eYFP-GFP2-eYFP (YG_2Y). All fusions were ligated into the pcDNA3.1+ vector. Sequences were confirmed by DNA sequencing.

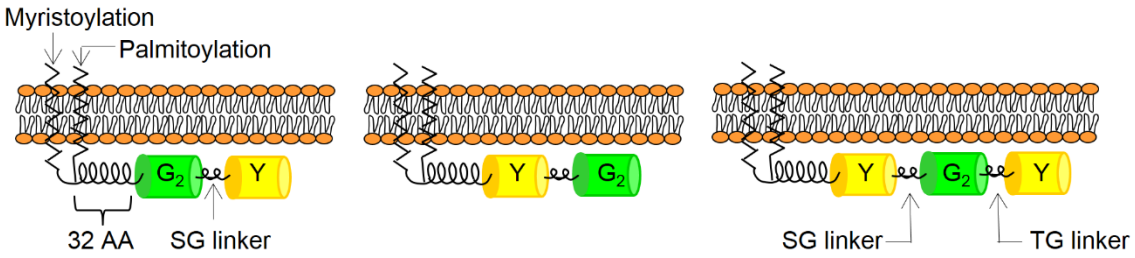

Figure 3.4: Schematic representation of dimeric and trimeric membrane FRET constructs. The addition of a myristoylation and palmitoylation sequence derived from $G\alpha_{i1}$ at the *N* terminus anchors the fluorescent proteins to the plasma membrane. Dimeric fluorescent proteins are linked by serine and glycine (SG) residues and eYFP in the trimeric configuration is linked by threonine and glycine (TG) residues.

3.2.3 Cell culture and Transfection

Chinese hamster ovary (CHO) cells were grown in Dulbecco's Modified Eagle's Medium (DMEM) without sodium pyruvate, supplemented with 10% fetal bovine serum (FBS), 2 mM L-glutamine, 1% penicillin/streptomycin and 1% non-essential amino acids. The cells were cultured and seeded 48 hours before imaging in 6-well plates (each well of 3.5 cm diameter) at a density of 15 – 20k cells/cm^2 and maintained at 37 ºC in a humidified

environment with 5% CO_2. After 24 hours, when the cells were 40-45% confluent, each dish or each well of 6-well plate was transfected with 2 µg of plasmid DNA with 10 µl Lipofectamine 2000 (Invitrogen, USA) diluted in 250 µl of OptiMEM (Invitrogen, USA) medium. The transfection procedure followed was similar to as described by Pisterzi et al. (27). Control cells with no plasmids (mock) were also cultured. Approximately 24 hours after transfection, medium of the cells grown in 6-well plate were removed and 250 µl of OptiMEM was added. The cells from each well were then lifted manually using cell scrapers and collected in 1 mL Eppendorf tubes. About 10 µl of cell suspension in OptiMEM was placed on microscope glass slide with a 0.3 mm cover slide on it and used for imaging. To image the cells using our latest version of OptiMiS (16) with an inverted microscope, the cells were also cultured in 3.5 mm petri dishes with 0.3 mm glass bottom cover slide in it at density 8 - 10k cells/cm^2 and transfected same way. The cells cultured in dishes were used directly for imaging without lifting.

3.2.4 Optical micro-spectroscopy

Spectrally resolved fluorescence imaging of samples were performed at room temperature using a spectrally resolved two-photon microscope (SR-TPM) (12). A femtosecond Ti-Sapphire laser (KM Labs, Boulder, CO) of 80 MHz pulse repetition rate and tunable wavelength of 780-820 nm was used as the excitation energy source. The laser was focused through an infinity corrected oil immersion objective (x100 magnification, NA 1.4, Nikon Instruments, Melville, NY) to a diffraction limited spot of the samples. The light emitted from the samples was projected onto a cooled electron-multiplying CCD camera (EMCCD; Andor, iXon 897) after passing through a

transmission grating. Our later experiments were performed using (OptiMiS) (16) attached to a Ti-Sapphire laser (Tsunami) with a tunable range of 690-1040 nm, 80 MHz repetition rate and < 100 fs pulse width. This instrument was improvised to have line scan (28) rather than the point scan resulting in two orders higher magnitude of acquisition speed compared to a point laser.

3.2.5 Elementary emission spectra of donor and acceptor

CHO cells expressing A5C were imaged using OptiMiS with 800 nm as the excitation wavelength and an average power of ~ 200 mW for line scan measured after microscope objective and ~ 20 mW for point scan measured before the scanning head SR-TPM. The spectrally resolved images collected by the CCD camera at one pixel apart in spectral dimension were reconstructed as described by Raicu et al. (12) to get the spectral images at various wavelengths of the spectral range. Similarly, CHO cells expressing VCVV were excited at 1020 nm (where Cerulean cannot be excited) using similar power in order to obtain the Venus spectrum.

Fig. 3.5 represents the spectral images of representative CHO cells individually expressing A5C and VCVV at different emission wavelengths. The background-corrected average intensity (averaged over certain non-zero intensity pixels as shown by circles in the images of Fig. 3.5) of the spectral images were calculated and normalized in order to obtain the elementary emission spectra of donor and acceptor as shown by the cyan and yellow curve, respectively, of Fig. 3.5. The normalized donor, and acceptor spectrum of

membrane constructs were obtained by imaging CHO cells expressing individually GFP_2, and YFP using laser of ~ 600 mW and tuned at 800 nm and 970 nm respectively.

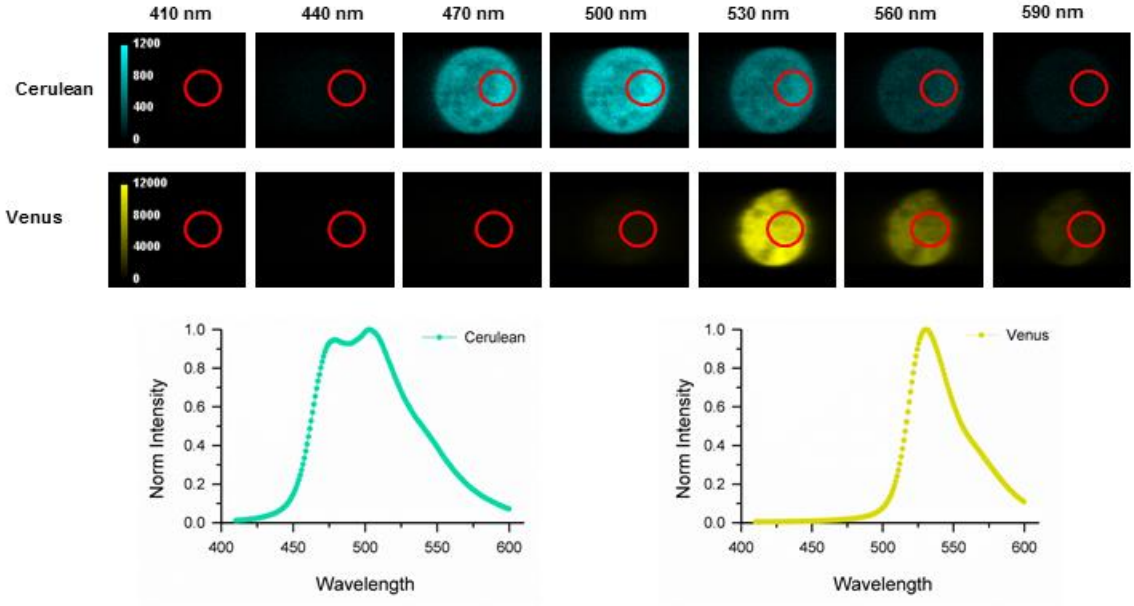

Figure 3.5: Spectral images of a representative CHO cell expressing the cytoplasmic constructs A5C or VCVV, with Cerulean as a donor and Venus as an acceptor of energy. Cyan and yellow plots are the elementary spectra of Cerulean and Venus averaged over bright pixels of a certain region of interest (shown as a red circle in each spectral image).

3.2.6 Analysis of FRET images and FRET efficiency calculation

CHO cells expressing the membrane and cytoplasmic FRET standards were imaged using the optical micro-spectroscope. The normalized elementary spectra of the donor and acceptor, previously determined, were used to unmix the spectrally resolved images at every pixel of the imaged section of the cell expressing the FRET constructs by adjusting the fitting parameters $k^{DA}(\lambda_{ex})$ and $k^{AD}(\lambda_{ex})$ to minimize error as described in section 3.1.4. Thus at every pixel of the imaged section of the cell, the donor fluorescence intensity in the presence of acceptor $k^{DA}(\lambda_{ex})$ and the acceptor fluorescence intensity in

the presence of donor $k^{AD}(\lambda_{ex})$ were calculated. The $k^{DA}(\lambda_{ex})$ and $k^{AD}(\lambda_{ex})$ values along with the quantum yields and spectral integration of the emission spectrum (w^D, w^A) of donor and acceptor were used in equation (3.41) to calculate the apparent FRET efficiency map (E_{app}). To avoid instrumental and other background noise in the E_{app} image, a threshold was used for $k^{DA}(\lambda_{ex})$ and $k^{AD}(\lambda_{ex})$ values.

3.3 Results and discussion

3.3.1 Measured and predicted FRET efficiency of cytoplasmic constructs

The kinetic model of FRET theory was tested using cytoplasmic FRET standards; cells transfected with ACVA, VCAA, ACAV, and VCVV were imaged and apparent FRET efficiency maps were obtained as described in section 3.6. Fig. 3.6 shows donor fluorescence intensity in the presence of acceptor (k^{DA}), acceptor fluorescence intensity in the presence of donor (k^{AD}) and apparent FRET efficiency map (E_{app}) of representative CHO cells expressing either ACVA, VCAA, ACAV, and VCVV. The E_{app} histograms as shown in Fig. 3.6 were obtained by binning the E_{app} pixels according to their value with bin size 0.01 (in the scale of 1) and plotting the number of pixels in each bin against E_{app}. The FRET efficiency histogram is then integrated and averaged over the number of bright pixels to calculate the average FRET efficiency of the imaged section of the cell. The values of the FRET efficiency averaged over a number of cells (represented by n below) for each construct for 9 different days of experiments is listed in Table 3.1. The measured average FRET efficiency for dimers ACVA, VCAA, and ACAV was found to be 0.53 ± 0.04 (n=114), 0.60 ± 0.05 (n=95), and 0.45 ± 0.06 (n=116) respectively. The tetramer,

VCVV with one donor and three acceptors had measured FRET efficiency of 0.80 ± 0.05 (n=96).

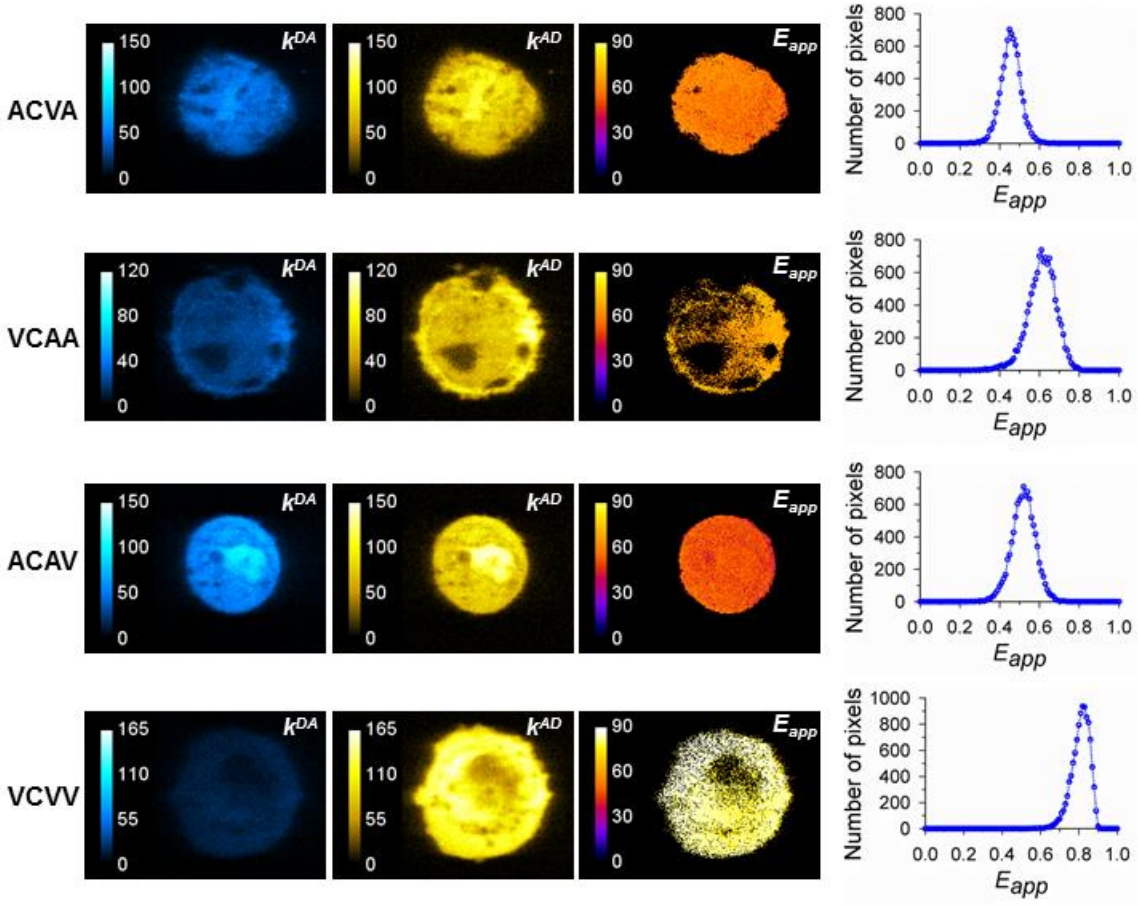

Figure 3.6: Photomicrograph of CHO cells expressing cytoplasmic tetramers. The three images on left show special distribution of the donor intensity in the presence of acceptor (k^{DA}), acceptor intensity in presence of donor (k^{AD}) and apparent FRET efficiencies (E_{app}) of a representative CHO cells transfected with ACVA, VCAA, ACAV, and VCVV. Histograms (right) show the number of pixels vs. E_{app} obtained from the FRET efficiency map (E_{app} image) of corresponding cells.

The apparent FRET efficiency of VCVV can also be predicted using the known energy transfer efficiencies of ACVA, VCAA, and ACAV, by plugging equation (3.7,) into equation (3.12) and using i=1 for the number of donor and j=1 for the number of acceptors. This gives:

$$E_{predicted} = \sum_j \frac{E_j/1 - E_j}{1 + \sum_j (E_j/1 - E_j)} \tag{3.52}$$

where j=ACVA, VCAA, or ACAV. The error of the predicted value of VCVV was calculated using the method of propagation of errors as:

$$d[\ln(E_{predicted})] = \frac{dE_{predicted}}{E_{predicted}} = \frac{\sum_j \frac{dE_j}{(1 - E_j)^2}}{\left\{\sum_j \frac{E_j}{(1 - E_j)}\right\}\left\{1 + \sum_j \frac{E_j}{(1 - E_j)}\right\}} \tag{3.53}$$

The predicted FRET efficiency of VCVV was found to be 0.77 ± 0.05, which was same as the measured FRET efficiency of VCVV within the limits of experimental errors.

Table 3.1: Measured and predicted apparent FRET efficiencies of cytoplasmic constructs

Cytoplasmic constructs	E_{app}	$\boldsymbol{E_{app}^{corrected}}$
ACVA	0.53 ± 0.04 (n = 114)	0.45 ± 0.04 (n = 114)
VCAA	0.60 ± 0.05 (n = 95)	0.53 ± 0.06 (n = 95)
ACAV	0.45 ± 0.06 (n = 116)	0.36 ± 0.07 (n = 116)
VCVV	0.80 ± 0.05 (n = 96)	0.72 ± 0.07 (n = 96)
VCVV predicted	0.77 ± 0.05	0.72 ± 0.07

All the measured and predicted E_{app} values of VCVV for 9 different days of experiment are listed in Table A.1. in appendix A. A paired Student's *t*-test for the mean values of measured and predicted FRET efficiencies (listed in Table A.1) returned the t value (two-tailed) of 2.20 corresponding to the probability of 0.20 for the measured and predicted FRET efficiencies to be statistically insignificant (critical value = 0.05). Thus, results for Student's *t*-test suggested that the differences in measured and predicted FRET efficiencies are within the standard deviations for each of the two sets.

3.3.2 Measured and predicted FRET efficiencies of membrane constructs

We have also tested the kinetic theory of FRET using our spectral FRET method and the membrane constructs YG_2, G_2Y and YG_2Y. Fig. 3.7 shows the donor fluorescence intensity in the presence of acceptor (k^{DA}), acceptor fluorescence intensity in the presence of donor (k^{AD}) and apparent FRET efficiency map of representative CHO cells expressing YG_2, G_2Y and YG_2Y. The FRET efficiency histogram and average FRET efficiency for each cell were calculated the same way as mentioned in section 3.7.1.

The measured FRET efficiencies of YG_2, G_2Y, and YG_2Y averaged over n cells as for each construct and the predicted FRET efficiency for YG2Y are listed in Table 3.2. The predicted FRET efficiency for the YG_2Y construct was calculated using the measured FRET efficiencies of YG_2 and G_2Y in equation (3.52). The measured and predicted FRET efficiency of the trimer YG_2Y were found to be the same within experimental error.

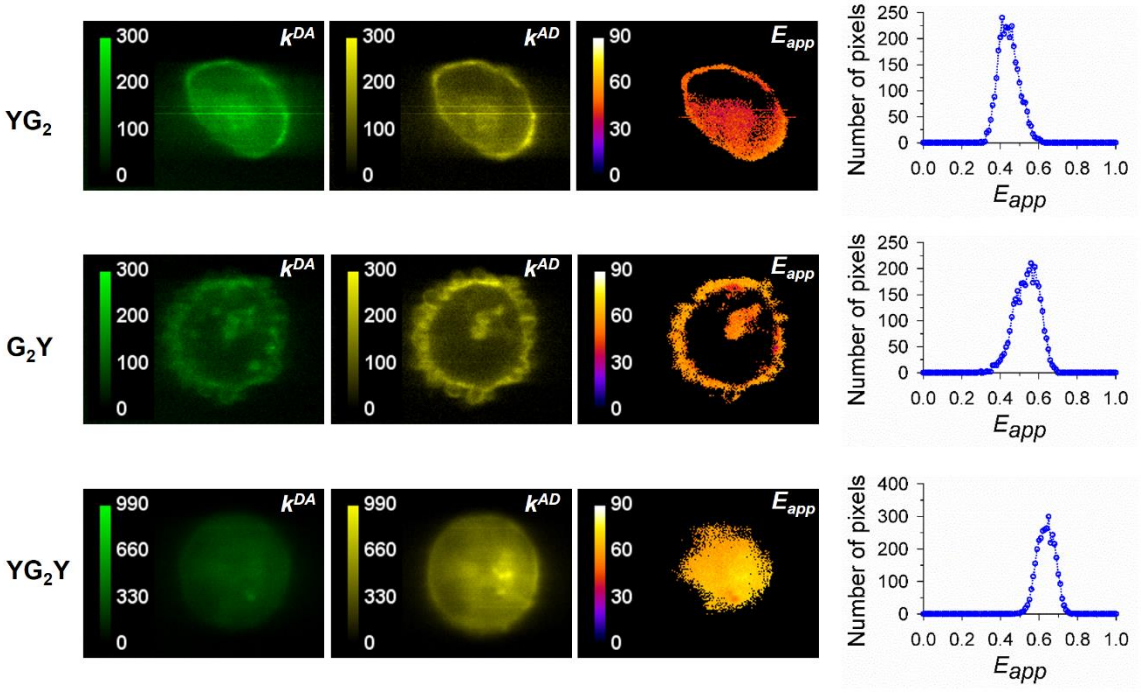

Figure 3.7: Photomicrographs of CHO cells expressing membrane dimers and trimers. First, second, and third column show intensity map of donor in the presence of acceptor (k^{DA}), acceptor in presence of donor (k^{AD}) and the distribution of apparent FRET efficiencies (E_{app}) of a representative CHO cells transfected with dimers (YG_2 and G_2Y) and trimers (YG_2Y). The apparent FRET efficiency (E_{app}) histograms obtained by binning E_{app} values in the bin interval of 0.01 and plotting against E_{app} are shown on the right.

Table 3.2: Measured and predicted E_{app} values for the membrane constructs

Membrane constructs	E_{app}	$E_{app}^{corrected}$
G_2Y	0.49 ± 0.07 (n = 48)	0.43 ± 0.08 (n = 48)
YG_2	0.41 ± 0.10 (n = 48)	0.34 ± 0.11 (n = 48)
YG_2Y	0.61 ± 0.06 (n = 49)	0.54 ± 0.07 (n = 49)
YG_2Y - predicted	0.62 ± 0.13	0.56 ± 0.17

3.3.3 Apparent FRET efficiency corrected for direct excitation

The contribution to acceptor signal resulting from direct excitation of acceptors was ignored in the calculation of apparent FRET efficiency (E_{app}) of the FRET standards listed as E_{app} in Table 3.1 and 3.2. As discussed in section 3.1.5, direct excitation of acceptor scan contribute towards the increase of measured FRET efficiencies of the FRET constructs. It was expected that the measured FRET efficiencies of the constructs with multiple acceptors can be significantly affected because of direct excitation of acceptors. Therefore, we have corrected the measured apparent FRET efficiencies of the individual constructs using equation (3.51).

The extinction coefficient of Venus at the excitation wavelength of ~ 400 nm were obtained by calculating absorbance ratio at 400 and 515 nm respectively using the absorption spectrum of Venus (29) and multiplying the ratio by the extinction coefficient of 92.2 x 10^3 $M^{-1}cm^{-1}$ at its excitation maximum of 515 nm (23). Similarly, the extinction coefficient of Cerulean at 400 nm was calculated using the absorption spectra (29) and extinction coefficient (22) of Cerulean. For the cytoplasmic tetramers with single donor and acceptor (ACVA, VCAA, and ACAV) the number of fluorophores (n) and the probability of acceptors (PA) in each construct was 2 and 1/2 respectively while for VCVV n, and PA was 4 and 3/4 respectively. Using these parameters in equations (3.48) and (3.51) the apparent FRET efficiencies of each cell were calculated. The corrected apparent FRET efficiencies of the constructs averaged over the number of cells are listed as $E_{app}^{corrected}$ in Table 3.1. The corrected apparent FRET efficiency of VCVV and its predicted FRET efficiency calculated using corrected FRET efficiencies of ACVA,

VCAA and VCVV in equation (3.52) suggested that they were same in the range of experimental error.

Similar procedure was followed to correct the apparent FRET efficiencies of the membrane proteins. The extinction coefficients used for GFP2 and eYFP at their respective excitation maximum 400 nm and 515 nm were 30.0×10^3 $M^{-1}cm^{-1}$ (30) and 83.4×10^3 M^{-1} cm^{-1} (23). The values of PA and n for G_2Y and YG_2 were 1/2 and 2 and those for YG_2Y were 2/3 and 3 respectively. The corrected FRET efficiencies for each construct averaged over the number of cells are listed in Table 3.2. The measured FRET efficiencies of YG_2Y was found to be same as the predicted FRET efficiency of YG_2Y using kinetic model of FRET.

3.3.4 Testing the effect of cellular viability on the FRET efficiency

From the measured and predicted apparent FRET efficiency values of VCVV and YG_2Y, as shown in Table 3.1 and Table 3.2 respectively, it was observed that measured and predicted FRET efficiencies for the tetramer VCVV and trimer YG_2Y were the same within the limits of the experimental errors. However, we performed a further experiment to test the effect of viability of the cells and expression level of proteins in the cells on apparent FRET efficiency. Since pH can be different for dead or live cells based on the ambient environment of the cells and quantum yields of fluorophores depend on pH, hence the change in pH in the environment of dead, and living cells can influence the measured FRET efficiency.

In order to investigate the effect of the cell vitality on the FRET efficiency we used a blue dye called cascade blue (Cascade Blue® Acetyl Azide, Trisodium Salt, Invitrogen), which is impermeable to the plasma membrane of cells. The single photon excitation maximum of cascade blue is 400 nm. The presence of cascade blue inside cells indicated a broken cell membrane or a dead cell. In order to test whether there is a difference in apparent FRET efficiencies of dead and living cells a 2 µM solution of cascade blue in distilled water was added to each sample before imaging. The imaged section of cells were unmixed using elementary emission spectrum of Cerulean, Venus and Cascade blue and the fluorescence intensities of donor in the presence of acceptor (k^{DA}), acceptor in presence of donor (k^{AD}), and intensity of cascade blue in presence of both donor and acceptor (k^{F}) was calculated as described by the equations (3.31) – (3.33).

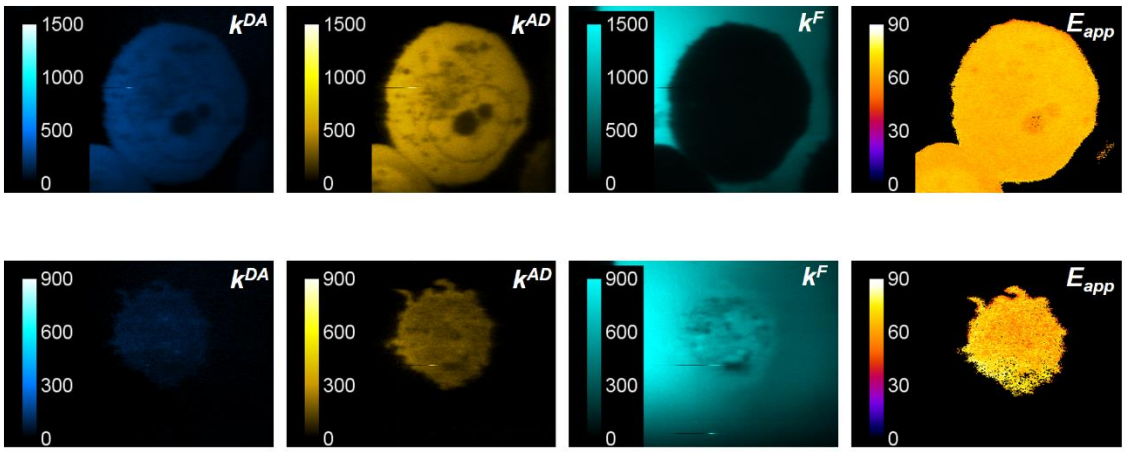

Figure 3.8: Photomicrograph of CHO cells expressing cytoplasmic construct, VCAA in presence of cascade blue. Images shown are two dimensional map of donor fluorescence intensity in the presence of acceptor (k^{DA}), acceptor in presence of donor (k^{AD}), and cascade blue intensity in presence of donor and acceptor (k^{F}). First row shows the image of a live CHO cell expressing VCAA while the second row shows the image for a dead cell. Distribution of apparent FRET efficiency map (E_{app}) for both type of cells shows similar FRET efficiencies.

First and second row of Fig. 3.8 shows the k^{DA}, k^{AD}, and k^{F} map of a representative dead and living cells respectively. Distribution of E_{app} map shows similar values of FRET efficiency for both the dead, and living cells. The average E_{app} values for living and dead cells shown in Fig. 3.8 are 0.60 ± 0.07 and 0.62 ± 0.11 respectively. We also calculated E_{app} values for each cell individually, and depending on the cascade blue intensity inside the cells; they are divided into dead, and living cell category. Based on these results, we concluded that apparent FRET efficiencies were independent of cells either being dead or alive. In other words, change in pH did not change the quantum yields of the fluorophores remarkably to change their apparent FRET efficiencies.

3.3.5 Investigation of stochastic FRET

For high expression levels of our FRET standards, the donor can transfer its energy via intermolecular FRET to nearby acceptors of adjacent complexes (31). The effect is known in the literature as *stochastic FRET*. Theoretically, stochastic FRET will be dominant for VCVV since more acceptors from the adjacent proteins are available to the donor to have intermolecular FRET. In order to test this effect, we performed an experiment using cytoplasmic tetramers ACVA, VCAA, ACAV, and VCVV at different expression level of the proteins. Cells were imaged after 6, 10, and 16 hours of transfection. Since each construct contains only one donor, therefore, expression of donor in each cell is a representation of expression level of the construct that can be calculated using equation, $F^{D}(\lambda_{ex}) = k^{DA}(\lambda_{ex})w^{D} + k^{AD}(\lambda_{ex})w^{A}$.

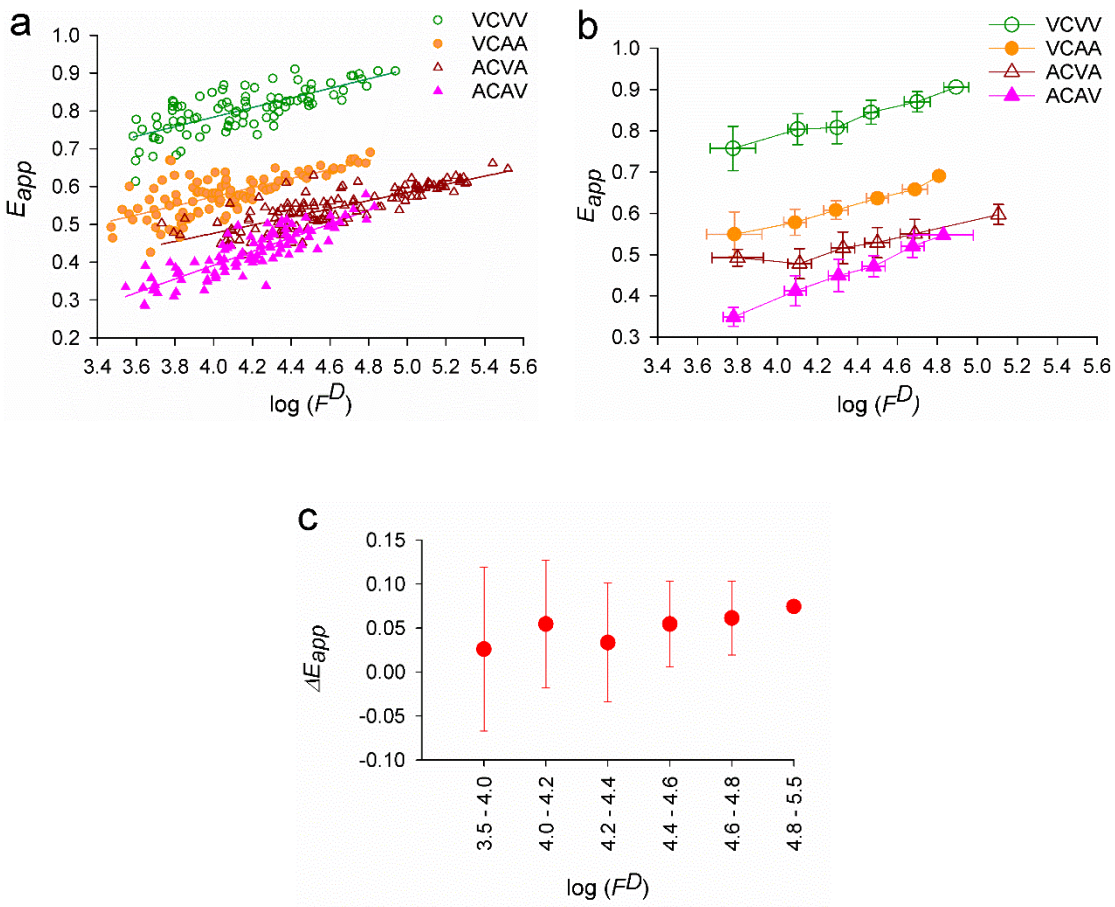

Figure 3.9: FRET efficiency (E_{app}) vs. log (F^D) for cytoplasmic tetramers. **(a)** Each data point represents a cell of VCVV (open circle), VCAA (closed circle), ACVA (open triangle) and ACAV (closed triangle). The solid lines passing through the data points represents linear fitting of log (F^D) values for each construct. **(b)** The data points are averaged over a certain range of log (F^D) shown in Table A.2. The standard deviations are shown by vertical lines through each data point on the plot. **(c)** Closed circles represent difference in measured and predicted FRET efficiencies of VCVV for log (F^D) ranges listed in Table A.3, vertical line through each point shows error for each data point.

Fig. 3.9 (a) shows the variation of average FRET efficiencies (E_{app}) with log (F^D) for ACVA, VCAA, ACAV, and VCVV where each data point represents one cell. We also divided the entire range of log (F^D) for each construct into six divisions and calculated the average values of log (F^D), E_{app}, and standard deviation for each range as shown in Table A.2 in appendix I and plotted in Fig. 3.9 (b). Fig. 3.9 (c) shows plot of the difference in measured, and predicted apparent FRET efficiencies for VCVV (ΔE_{app})

against each interval of log (F^D) as shown in Table A.3 in appendix A.2. The error calculated using the method of propagation of error for ΔE_{app} is also listed in Table A.3 and shown by the error bar in Fig. 3.9c. A paired Student's t-test performed to check the statistical significance of dependence of ΔE_{app} values with log (F^D) gave the *t* value of 2.3 corresponding to the probability of 0.78 for the dependence of the difference between the measured and predicted FRET efficiencies to be statistically insignificant (critical value = 0.05). The graph shown in Fig. 3.9 (a), (b) & (c) for each construct shows that apparent FRET efficiency increases with the increase in expression level of proteins (constructs), although based on the Student's *t*-test the difference between the measured and predicted values for VCVV is independent of the expression level. From these observations, we concluded that for the agreement between measured and predicted FRET efficiencies for VCVV or YG_2Y is very robust and independent of whether intramolecular FRET is contaminated by intermolecular (or stochastic) FRET.

3.4 Conclusion

The theory of FRET based on fluorescence lifetime imaging techniques have so far been widely investigated to probe protein-protein interactions. However, the study of oligomerization and stoichiometry of protein complexes through intensity-based measurements have only emerged recently. The technique based on spectrally resolved two-photon microscopy proposed by Raicu et al. has recently attracted wide attention owing to its ability to investigate the quaternary structure of macromolecules in living cells.

Using this method, we tested the kinetic FRET theory for multimeric complexes using protein standards expressed both in the cytoplasm and in the membrane. The results showed that the measured average FRET efficiencies of the membrane trimer, YG_2Y, and cytoplasmic tetramer, VCVV, using the theory based on the approximation of negligible direct excitation of acceptors were same as the predicted FRET efficiencies using kinetic theory of FRET within the range of experimental error. Our corrected theory for the calculation of FRET efficiency involving direct excitation of acceptor showed changes in the measured values of average FRET efficiencies of the individual constructs while the difference between the measured and predicted FRET efficiencies of YG_2Y and VCVV remained the same.

Our results disagreed with those of Koushik et al., which indicated significant discrepancies between the measured and predicted FRET efficiencies for VCVV. We tested the possibility that the excess in energy transfer for VCVV reported by Koushik et al. (13) based on the change in pH resulting from the change in the ambient environment for living and dead cells. The results based on the fact that the cell was dead if its plasma membrane were broken did not show any difference in average FRET efficiencies for dead and living cells.

We further investigated the effect of stochastic FRET on the measured FRET efficiencies. The results showed that the FRET efficiencies increased with increase in the expression levels of proteins encoding the fluorescence probes. However, there was no difference in between the measured and predicted FRET efficiencies for VCVV even for

the highest expression level. This result suggested that stochastic FRET, when present were already incorporated into the measured FRET efficiencies and accounted for by the theory.

In light of these facts, we conclude that the discrepancies found by Vogel's group between the measured and predicted FRET efficiencies was possibly due to an unidentified systematic error in their experiments and/or data analysis.

References

1. Stryer L (1978). Fluorescence energy transfer as a spectroscopic ruler. *Annu Rev Biochem* 47:819-846.

2. Clegg RM (1996). Fluorescence resonance energy transfer. Fluorescence Imaging Specroscopy and Microscopy, eds X. F. Wang & Herman B (John Wiley & Sons, Inc. , New York), pp 179–252.

3. Lakowicz JR (2006). Principles of Fluorescence Spectroscopy (Springer, New York).

4. Förster T (1946). Energiewanderung und Fluoreszenz. *Naturwissenschaften* 33(6):166-177.

5. Förster T (1947). Fluoreszenzversuche an Farbstoffmischungen. *Angew Chem A* 59:181-187.

6. Förster T (1948). Zwischenmolekulare Energiewanderung und Fluoreszenz. *Ann Phys* 2:55-75.

7. Vamosi G, Gohlke C & Clegg RM (1996). Fluorescence characteristics of 5-carboxytetramethylrhodamine linked covalently to the 5' end of oligonucleotides: multiple conformers of single-stranded and double-stranded dye-DNA complexes. *Biophys J* 71(2):972-994.

8. Lee NK, et al. (2007). Three-color alternating-laser excitation of single molecules: monitoring multiple interactions and distances. *Biophys J* 92(1):303-312.

9. Raicu V (2010). FRET-based determination of protein complex structure at nanometer length scale in living cells. Nanoscopy and Multidimensional Optical Fluorescence Microscopy, ed Diaspro A (CRC Press, Boca Raton).

10. Raicu V (2007). Efficiency of resonance energy transfer in homo-oligomeric complexes of proteins. *J Biol Phys* 33(2):109-127.

11. Yeow EK & Clayton AH (2007). Enumeration of oligomerization states of membrane proteins in living cells by homo-FRET spectroscopy and microscopy: theory and application. *Biophys J* 92(9):3098-3104.

12. Raicu V, et al. (2009). Determination of supramolecular structure and spatial distribution of protein complexes in living cells. *Nature Photon* 3(2):107-113.

13. Koushik SV, Blank PS & Vogel SS (2009). Anomalous surplus energy transfer observed with multiple FRET acceptors. *Plos One* 4(11):e8031.

14. Zimmermann T, Rietdorf J, Girod A, Georget V & Pepperkok R (2002). Spectral imaging and linear un-mixing enables improved FRET efficiency with a novel GFP2-YFP FRET pair. *FEBS Lett* 531(2):245-249.

15. Tsien RY (1998). The green fluorescent protein. *Annu Rev Biochem* 67:509-544.

16. Stoneman MR, et al. (2012). Quantifying the efficiency of various FRET constructs using OptiMiS (TM). *Biotechniques* 52(3):191-195.

17. Raicu V, Jansma DB, Miller RJ & Friesen JD (2005). Protein interaction quantified in vivo by spectrally resolved fluorescence resonance energy transfer. *Biochem J* 385(Pt 1):265-277.

18. Elangovan M, Day RN & Periasamy A (2002). Nanosecond fluorescence resonance energy transfer-fluorescence lifetime imaging microscopy to localize the protein interactions in a single living cell. *J Microsc* 205(Pt 1):3-14.

19. Förster T (1965). Delocalized excitation and excitation transfer (Florida State University, USA) p 122.

20. Berney C & Danuser G (2003). FRET or no FRET: a quantitative comparison. *Biophys J* 84(6):3992-4010.

21. Epe B, Steinhauser KG & Woolley P (1983). Theory of measurement of Foster-type energy transfer in macromolecules. *Proc Natl Acad Sci U S A* 80:2579-2583.

22. Rizzo MA, Springer GH, Granada B & Piston DW (2004). An improved cyan fluorescent protein variant useful for FRET. *Nat Biotechnol* 22(4):445-449.

23. Nagai T, et al. (2002). A variant of yellow fluorescent protein with fast and efficient maturation for cell-biological applications. *Nat Biotechnol* 20(1):87-90.

24. Koushik SV, Chen H, Thaler C, Puhl HL, 3rd & Vogel SS (2006). Cerulean, Venus, and VenusY67C FRET reference standards. *Biophys J* 91(12):L99-L101.

25. Sprang SR (1997). G protein mechanisms: insights from structural analysis. *Annu Rev Biochem* 66:639-678.

26. Rens-Domiano S & Hamm HE (1995). Structural and functional relationships of heterotrimeric G-proteins. *FASEB J* 9(11):1059-1066.

27. Pisterzi LF, et al. (2010). Oligomeric size of the M2 muscarinic receptor in live cells as determined by quantitative fluorescence resonance energy transfer. *J Biol Chem* 285(22):16723-16738.

28. Biener G, et al. (2013). Development and Experimental Testing of an Optical Microscopic Technique Incorporating True Line-Scan Excitation. *Int J Mol Sci (under review)*.

29. Day RN & Booker CF (2008). Characterization of an improved donor fluorescent protein for Forster resonance energy transfer microscopy. *J Biomed Opt* 13(3):031203.

30. Yang F, Moss LG & Phillips GN, Jr. (1996). The molecular structure of green fluorescent protein. *Nat Biotechnol* 14(10):1246-1251.

31. Singh DR & Raicu V (2010). Comparison between Whole Distribution- and Average-Based Approaches to the Determination of Fluorescence Resonance Energy Transfer Efficiency in Ensembles of Proteins in Living Cells. *Biophys J* 98(10):2127-2135.

Chapter 4. Quaternary structure determination of the muscarinic M3 acetylcholine receptors at the plasma membrane

4.1 Biological system of interest

4.1.1 G-proteins

The guanosine nucleotide-binding proteins commonly referred to as G-proteins are a class of membrane proteins that serve as intermediaries for communicating signals between cells and extracellular compounds such as hormones and neurotransmitters (1, 2). The G-proteins, when coupled with numerous membrane receptors in cells, serve as vital components in transferring signals to the cells generating diverse biological responses (3). The heterotrimeric G-proteins are composed of three subunits encoded by distinct genes, α, β, and γ, each existing in several isoforms that together make hundreds of combinations of G-proteins. The binding of G-protein with certain receptors lead to target specific physiological processes in response to external stimuli that is largely governed by the specific combinations of α, β, and γ subunits (4, 5).

4.1.2 G-protein coupled receptors

G-protein coupled receptors (GPCRs) are the largest class of membrane proteins that allows a wide variety of signal transmission from outside to inside of a cell. They receive signals from their ever changing environment and transfer it inside the cells by activating G-proteins coupled to them triggering biological responses to specific stimuli (6).

GPCRs are known to consist of seven transmembrane alpha helices that are spanned along the width of the plasma membrane and hence it is also termed as seven-

transmembrane receptor (6, 7). The seven transmembrane segments are connected by three intra- and extra-cellular loops. The portion of a GPCR outside the cell receives extracellular signals transferring it to the inside of the cell where it interacts with the G-protein coupled to the receptor for complete signal transduction from outside to inside of the cell. The functional diversity of GPCRs is due to their ability to bind to a broad range of ligands, such as small organic compounds, peptides, and proteins. The ability of GPCR to bind to specific ligand not only helps in the signal transduction process but also makes GPCR as a target of several drugs (8).

Based on their sequence homology and functional similarity, GPCRs are classified into several families (9-12). Attwood and Findaly (13) proposed seven hydrophobic domains of GPCRs based on their amino acid sequence. Latter, Kolakowski (14) introduced A – F and O classifications for GPCRs. The classification was made on the basis of receptor binding to G-proteins. All those receptors that were proven to bind with G-proteins were classified in A – F family while remaining seven transmembrane spanning proteins were assigned to O (other) family. Fredriksson et al. (15) divided the known and predicted 802 human GPCRs in five main families' viz. Glutamate, Rhodopsin, Adhesion, Frizzled/Taste2 and Secretin popularly known as GRAFS. The major difference between previous, and recent nomenclature introduced by Fredriksson et al. is the division of family B into Secretin and Adhesion family. Recent nomenclature system includes extended total number of unique receptors and also recently discovered bitter Taste2 receptors (16).

4.1.3 Signal transduction mechanism through G-protein coupled receptors

The first step involved in the action of a GPCR for signal transduction is specific activation of the receptor through binding of ligands such as hormones, and neurotransmitters at the cell surface (5, 17-21). The signal transduction mechanism is shown schematically in Fig. 4.1.

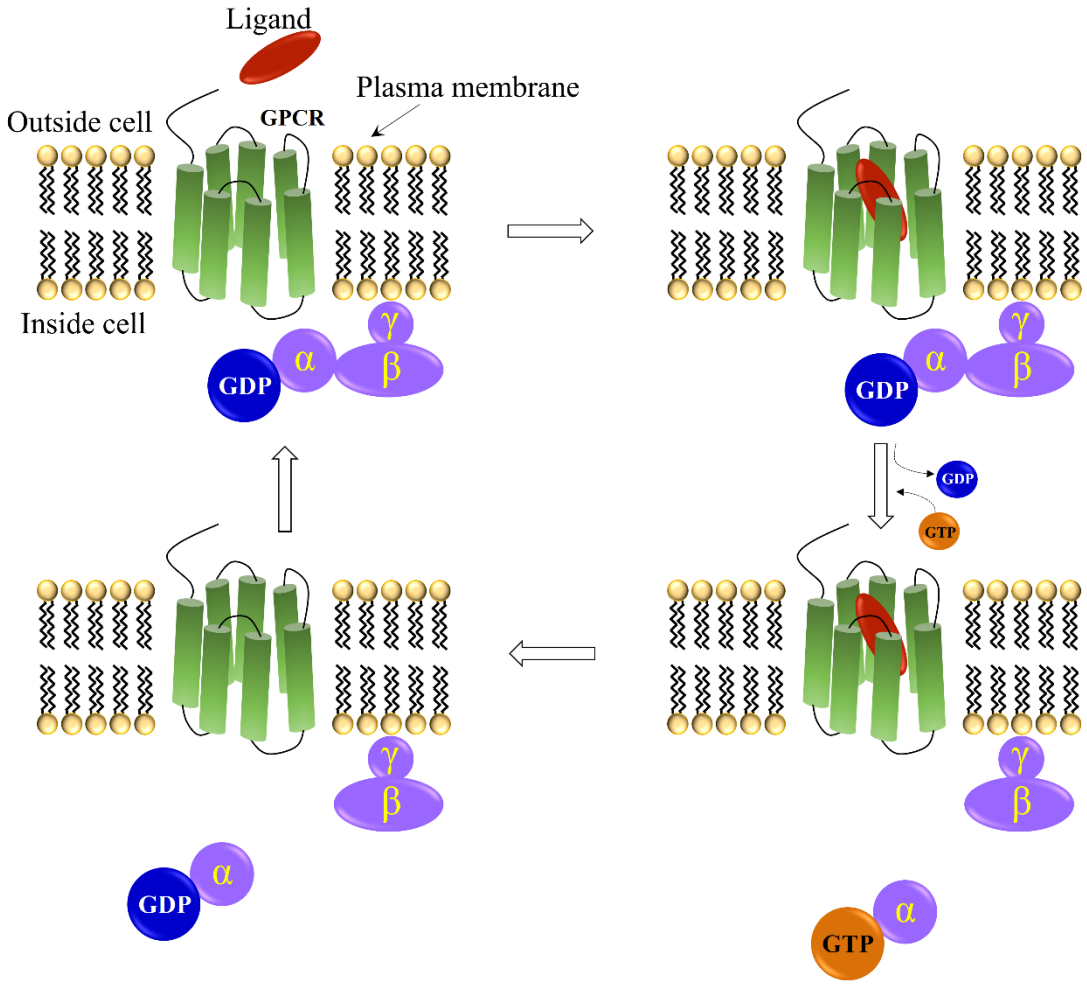

Figure 4.1: Schematic showing signal transduction mechanisms through GPCRs. The figure is adapted from (22).

The binding of a ligand to a GPCR leads to conformational changes in the receptor allowing it to function as a guanine-nucleotide exchange factor (GEF) catalyzing

the exchange of GTP with GDP bound to G_α of G-protein (8-12). The G_α subunit bound to the GTP dissociates from $G\beta\gamma$ dimer and the receptor. Both G_α-GTP and $G_{\beta\gamma}$ subunits then bind and regulate the appropriate effector system activating different signal cascades. The system is then deactivated when intrinsic GTPase activity of α-subunit hydrolyzes GTP to GDP mediated by GTPase-activating proteins, allowing it to re-associate with $G_{\beta\gamma}$ and start a new cycle (8-12).

4.1.4 Muscarinic acetylcholine receptors

Muscarinic acetylcholine receptors (mAChRs) are members of class A GPCRs that regulate numerous fundamental functions in peripheral and central nervous system (PNS and CNS, respectively). Acetylcholine is synthesized in a reaction of acetyl coenzyme A (acetyl CoA) and choline in a nerve terminal by choline acetyltransferase. Acetylcholine is stored in the nerve terminal and released into the synapse upon nerve depolarization. Acetylcholine thus produced is received by the acetylcholine receptors. There are two types of acetylcholine receptors: (i) nicotinic receptor that is responsive to agonist nicotine ($C_{10}H_{14}N_2$) and (ii) muscarinic receptor that is responsive to the agonist muscarine ($C_9H_{20}NO^{2+}$) (23). Different types of muscarinic acetylcholine receptors bind to specific G-proteins inside a cell to cascade signals from outside to inside of the cells.

Riker and Wescoe (24) first reported the existence of muscarinic receptor subtypes. Because of diversified functions of muscarinic receptors at various locations, and their potential therapeutic applications for various diseases like asthma, intestinal disorder, functions of the urinary bladder, and Alzheimer's diseases, studies based on

classifications of muscarinic receptors have attracted wide interest. The research presented by Peralta et al. suggested that human mAChRs contain at least four subtypes (M_1 – M_4) which are different in their structures, affinity to various ligands, and their pattern to tissue specific expression (25). Later, Bonner et al. cloned and expressed a fifth human receptor in mammalian cells that is closely related to M_3 (26). Based on the mAChRs coupling with different types of G-proteins, they are divided into two broad classes: first, M_1, M_3, and M_5 that are preferentially coupled to $G_{\alpha q}$/11 type of G-proteins and second, M_2 and M_4, which activate $G_{\alpha i}$/0 type of G-proteins (27-31). M_1, M_4, and M_5 receptors are present mainly in CNS while M_2 and M_3 are present both in CNS and PNS (31). CNS muscarinic receptors mainly regulate behavioral, sensory, and autonomic processes and are responsible for many diseases such as Alzheimer's diseases, Parkinson's diseases, depressions, and schizophrenia. The PNS receptors are mainly present on the effector tissues innervated by parasympathetic nerves and are mainly responsible for a decrease in heart rate, increase in glandular secretion, and smooth muscle contractility (31).

Among the five different types of muscarinic receptors, type-3 muscarinic receptors (M_3Rs) are present mainly in smooth muscles, endocrine and exocrine glands, lungs, pancreas, and the brain. In CNS, M_3Rs induce emesis. M_3Rs that are expressed in certain regions of the brain influence insulin homeostasis regulation. The mutations of M_3Rs cause urinary bladder diseases and prune belly-like syndrome which are the frequent causes of progressive renal failure in children (32). Sjögren's syndrome is a chronic autoimmune disease where the immune cells attack and destroy the exocrine

glands because of unknown reasons (33). Although the diagnosis of the diseases are yet to be understood, researchers reported that antibodies of agonist M_3Rs are detected in patients attacked by the Sjögren's syndrome and were proposed to contribute to pathogenesis (34). Under-expression of either the M_3 or the M_2 receptors in smooth muscles cause disorder of the smooth muscle organs leading to paralysis ileus (35). Apart from the above-mentioned chronic diseases, M_3Rs are also involved in several other diseases such as type 2 diabetes, obesity, peptic ulcer disease, irritable bowel syndrome, and gastrointestinal spasms. It is, therefore, important to understand the structural and functional form of these receptors and their mutations.

Since more than single subtype of mAChRs are present at any location of CNS or PNS and to date there is no specific ligand that activates specific mAChR, it is not clear so far whether a single or multiple subtypes of receptors are responsible for a particular disease. Researchers have been trying to develop agonists and antagonists for subtype selective mAChRs for the treatment of various diseases, but these receptors have highly subtype selective orthosteric binding sites (31, 36), which is one of the major challenges for the medicinal chemist to develop subtype specific orthosteric ligands. This complicates the discovery of novel drug particular for a specific subtype of mAChRs causing their side effects by blocking/activating multiple mAChRs. Recently, research has been focused on developing novel drugs that can bind to target mAChRs through allosteric mechanism due to their high selectivity and effectiveness. Hence, these drugs are more target specific and have less side effects (36, 37). Most of the mAChRs have two allosteric binding sites, and the allosteric ligands have no effect on the receptors in

the absence of the agonists (36, 37). Recent findings of AC-42 (38, 39) and N-desmethylclozapine (40) which can very selectively activate M_1 mAChRs, raised the hope of possible discovery of specific mAChR subtype binding ligands by targeting allosteric receptor sites (31).

Apart from these findings, it is also critical to understand the quaternary structure of these receptors in their native environment to help to understand the functional forms and diversities of these receptors and their responses to specific drugs. Many questions need to be addressed for the drug discovery; a few among them are: (a) whether or not they oligomerize to bind to specific ligands? (b) How do they respond to the ligands or drugs i.e., do they undergo any changes in the quaternary organizations? In other words, do the ligands regulate their quaternary size, and shape from one form to the other? (c) Does the expression level of the receptors in cells change their affinity for the ligands? To address the above questions we have described a method in the following section where we used muscarinic acetylcholine receptors type 3 (M_3Rs) as our biological system of interest.

4.2 Oligomerization of muscarinic M_3 acetylcholine receptors

(This research was originally published in Biochemical Journal. S Patowary, E Alvarez-Curto, T R Xu, J D Holz, Julie A. Oliver, G Milligan and V Raicu, The muscarinic M_3 acetylcholine receptor exists as two differently sized complexes at the plasma membrane. Biochem. J. (2013); 452: 303–312 © The Biochemical Society).

4.2.1 Review of GPCR's oligomerization

G protein-coupled receptors (GPCRs) are the largest family of transmembrane proteins in the human genome and the most utilized as the targets for small molecule drugs and medicines (11). In recent times, a series of atomic level X-ray structures of members of the large class of rhodopsin-like GPCRs (41-46) has appeared to provide support for the historical view, based on analysis of the binding of such drugs, that these receptors exist as monomeric, non-interacting polypeptides. Despite this, there has been a persistent literature consistent with GPCRs existing as dimers or higher-order oligomers (47, 48). Gratifyingly for champions of this proposal, recent X-ray structures of the chemokine CXCR4 receptor have provided strong evidence of a substantial dimer interface involving elements of transmembrane domains V and VI (49). Moreover, the structure of the μ-opioid receptor shows a dimeric 4-helix bundle interface provided by many of the residues of transmembrane domains V and VI as well as a further, less extensive, interface provided by elements of transmembrane domains I and II along with the intracellular element often designated 'helix VIII' (50). These interfaces potentially allow the presence of tetrameric or even higher-order organization (50) and suggest that at least a subset of the rhodopsin-like GPCRs form quaternary structures with avidity sufficient to be maintained throughout detergent-mediated solubilization and preparation for crystallization trials.

Support for the presence of GPCR dimers and/or higher-order quaternary complexes in intact cells and tissues has been derived from studies involving techniques ranging from fluorescence recovery after photobleaching (51) to approaches employing

resonance energy transfer (52-55). Despite this, the functional significance of GPCR quaternary structure remains uncertain, although a substantial number of studies have shown the importance of dimeric/oligomeric interactions for the proper maturation and cell surface delivery of class A receptors (56-58) and are consistent with interactions occurring at an early stage in GPCR synthesis.

Although certain commentators have championed the primacy of monomeric or oligomeric forms of rhodopsin-like GPCRs (59, 60), it is not obvious that a single state must exist at the exclusion of others. Studies based on fluorescence recovery after photobleaching and antibody-based tethering of a GPCR have provided evidence for dynamic interactions between individual protomers, and for the extent of the interaction varying between even closely related class A GPCRs (51). Furthermore, studies that have begun to develop single molecule tracking have provided evidence of association and disassociation of what appear to be GPCR quaternary complexes (60-62). Herein we have assessed this hypothesis in cells engineered to express a form of the muscarinic M_3 acetylcholine receptor (M_3R) tagged with an energy acceptor to remain at a constant amount, whilst levels of an energy donor-tagged form of a mutationally modified version of this receptor (Tyr149Cys, Ala239GlyM_3R) could be titrated from an inducible locus (63). Specifically, we investigated the quaternary organization and degree of stability of M_3R at the plasma membrane. This was achieved by using measurement and analysis, within a suitable theoretical framework (64, 65), of distributions of apparent FRET efficiencies, E_{app} (or E_{app} histograms), across FRET images of individual cells expressing proteins of interest (54). The quaternary structure of the complex is identified from the

number and relative disposition of peaks within an E_{app} histogram, which constitutes a veritable "FRET spectrum" associated with a specific quaternary structure. The separation of dimer from tetramer signals is achieved using a method here introduced that takes into account the amplitudes of the individual peaks in the E_{app} histogram. Data analysis indicates that, at the plasma membrane, homomers of the M_3R exist as a mixture of dimers and rhombic tetramers whilst biochemical studies support dynamic interchanges between such complexes.

4.2.2 Materials and methods

4.2.2.1 Cell models

Flp-In™ T-REx™ 293 cells constitutively expressing FLAG-M_3R-Citrine and also harboring Myc-Tyr149Cys, Ala239GlyM_3R-Cerulean at the Flp-In™ T-REx™ locus that provides tetracycline inducible expressions were generated previously and described fully (63). Cells were grown in Dulbecco's Modified Eagle's Medium (DMEM) without sodium pyruvate, supplemented with 10% organic fetal bovine serum (FBS, PAA Laboratories Inc, Dartmouth, MA), 2 mM L-glutamine, 1% penicillin/streptomycin, 10 μg mL^{-1} blasticidin, 200 μg mL^{-1} hygromycin B, and 1 mg mL^{-1} G418. Equivalent cells able to express either FLAG-M_3R-Citrine or Myc-Tyr149Cys, Ala239GlyM_3R-Cerulean in isolation from the Flp-In™ T-REx™ locus were generated and maintained in the same way, but without G418. Cell lines were maintained at 37 °C in a humidified environment with 5% CO_2. 72 hours prior to imaging, the cells were sub-cultured and seeded at 48,000-60,000 cells/cm^2. The cells were approximately 70% confluent after 48 hours of growth, at which time fresh medium, containing doxycycline at concentrations as

indicated, was added to the cells for an additional 24 hours incubation. The cells were then non-enzymatically lifted using Cellstripper (Mediatech Inc., Manassas, VA) and re-suspended in 1 mL Opti-MEM (Life Technologies, Grand Island, NY) for imaging.

4.2.2.2 Cell-surface biotinylation

Cells were seeded on plates previously coated with poly-D-lysine and washed with ice-cold borate buffer (10 mM boric acid, 154 mM NaCl, 7.2 mM KCl, and 1.8 mM CaCl2, pH 9.0) and incubated on ice with 1 mL of 0.8 mM EZ-Link sulphosuccinimidyl 2-(biotinamido)ethyl-1,3-dithiopropionate (Pierce Chemical, Rockford, IL) in borate buffer for 15 min. The cells were then rinsed with a solution of 0.192 M glycine and 25 mM Tris, pH 8.3, to quench the excess biotin, and lysed with RIPA buffer (50 mM HEPES, 150 mM NaCl, 1% Triton X-100, and 0.5% sodium deoxycholate, 10 mM NaF, 5 mM EDTA, 10 mM NaH_2PO_4, 5% ethylene glycol, pH 7.4). Lysates were centrifuged for 30 min at 14,000 g, and the supernatant was recovered. Cell surface-biotinylated proteins were isolated using 50 µL of ImmunoPure immobilized streptavidin (Pierce Chemical, Rockford, IL) and rotating for 1 hour at 4 °C. Samples were subsequently centrifuged, and the streptavidin beads were washed three times with RIPA buffer. Finally, the biotinylated proteins were eluted with 50 µL of SDS sample buffer for 1 h at 37 °C, and SDS-PAGE and Western blotting were performed.

4.2.2.3 Cell lysates, PAGE, and immunoblotting

Cells were washed once in cold PBS and harvested with ice-cold RIPA buffer supplemented with Complete Protease Inhibitor Cocktail (Roche Diagnostics, Mannheim,

Germany). Extracts were passed through a 25-gauge needle and incubated for 15 min at 4 °C while spinning on a rotating wheel. Cellular extracts were then centrifuged for 30 min at 14,000 g and the supernatant was recovered. Samples were heated at 65 °C for 15 min and subjected to SDS-PAGE analysis using 4–12% BisTris gels NuPAGE, (Life Technologies, Grand Island, NY) and MOPS buffer. Proteins were then electrophoretically transferred onto nitrocellulose membranes that were blocked for 45 min in 5 % fat-free milk in TBST (1x Tris-buffered saline containing 0.1 % (v/v) Tween 20) and subsequently incubated with the required primary antibody overnight at 4 °C. Incubation with the appropriate horseradish peroxidase-linked IgG secondary antiserum was performed for 2 hours at room temperature. Immunoblots were developed by application of enhanced chemiluminescence substrate (Pierce Chemical, Rockford, IL).

4.2.2.4 Proximity ligation assay (PLA)

Cells were seeded on 0-thickness glass cover slips previously coated with poly-D-lysine. PLA (66) was performed on cells maintained with or without doxycycline induction using the Duolink II Detection Kit (Olink Bioscience, Uppsala, Sweden). The antibodies used in this study were monoclonal mouse anti-FLAG M2 and rabbit anti-FLAG (Sigma Aldrich Co Ltd), and 9B11 mouse anti-Myc and rabbit anti-Myc (Cell Signaling Technology, Nottingham, UK).

4.2.2.5 Two-photon fluorescence microscopy

Approximately 10 μL of a suspension of cells in Opti-MEM medium was placed on a microscope slide and covered with a coverslip. A spectrally resolved two photon

microscope (SR-TPM) was used to acquire the spectral images as described (54). Briefly, a femtosecond Ti:Sapphire laser (KM Labs, Boulder, CO) was used as excitation energy source. Laser pulses with spectra approximately 20 nm wide (full-width half-maximum) were focused through an infinity-corrected oil immersion Plan Apochromat objective (×100 magnification, NA = 1.4; Nikon Instruments, Melville, NY) to a diffraction-limited spot onto the sample. The back-propagating fluorescence emitted by the sample was projected through a transmission grating onto a cooled electron-multiplying CCD camera (EMCCD; Andor, iXon 897).

4.2.2.6 Elementary emission spectra for the FRET pair

Cells harboring Myc-Tyr149Cys, Ala239Gly M_3R-Cerulean or FLAG-M_3R-Citrine and induced with 100 ng mL^{-1} doxycycline were imaged with the SR-TPM using 800-nm excitation light. Average powers of the order of 35 mW and 60 mW (measured before the scanning head of the microscope) were used for Cerulean and Citrine, respectively. The average emission spectra obtained from several cells were normalized to obtain elementary emission spectra of donor (D, Cerulean) and acceptor (A, Citrine). Due to the negligible Citrine excitation by the 800-nm laser light (note that Citrine has single photon absorption wavelength at 516 nm (66), the Citrine emission was very dim even at comparatively higher excitation power. Therefore, its spectrum contained cellular auto-fluorescence in the lower wavelength region. In order to correct for this artifact, the measured spectrum was fitted with three Gaussian functions, *viz.* a broad Gaussian at lower wavelengths corresponding to cellular auto-fluorescence, and two other closely spaced Gaussians corresponding to the two spectral components usually seen in Citrine

emission, were used to fit the measured spectrum of cells expressing FLAG-M_3R-Citrine. After the fitting, the first Gaussian was subtracted from the total measured spectrum to obtain the auto-fluorescence corrected emission spectrum of Citrine. For cross-checking, the emission spectrum of Citrine was also measured using a similar spectrally-resolved two-photon microscope equipped with a Ti-Sapphire laser (Tsunami, Spectra Physics) tuned to ~ 900 nm wavelength.

4.2.2.7 Image analysis

Spectral images obtained from cells co-expressing inducible Myc-Tyr149Cys, Ala239GlyM_3R-Cerulean and constitutive FLAG-M_3R-Citrine that had been treated with different concentrations of doxycycline were unmixed using the D and A elementary spectra, determined as described above, to obtain the donor fluorescence intensity in presence of acceptor (k^{DA}) and the acceptor fluorescence intensity in presence of donor (k^{AD}) at every pixel of the imaged section of the cell (54, 65). The spatial distribution map of FRET efficiencies was computed from the k^{DA} and k^{AD} values by using the following equation (3.41): Q^D (=0.62) (67), and Q^A (=0.76) (66). E_{app} distributions (i.e., the number of pixels showing a certain FRET efficiency value), or histograms, were computed by binning the apparent FRET efficiency values of all pixels (bin size, 0.01) and plotting their histograms. Only the pixels in regions of interest around the cellular membrane were included in the analysis. To reduce the probability that pixels characterized only by instrumental noise contribute to the distribution of FRET efficiencies, a threshold value was used for the k^{DA} and k^{AD} images.

Expression level of donor-tagged M_3R was determined by comparing the measured fluorescence intensity of the donor corrected for FRET to the fluorescence emission of a standard fluorescent solution of purified YFP (prepared as described elsewhere (68)), based on knowledge of absorption cross sections and the quantum yields of the two fluorophores (69, 70). All the procedures related to spectral unmixing, as well as computation of FRET efficiencies and donor-only fluorescence intensities were computer-coded using MatLab (The MathWorks, Inc., Natick, MA).

4.2.2.8 Estimation of the protein expression level

From the k^{DA} and k^{AD} values determined from spectral unmixing, we computed the fluorescence of the donor in the absence of acceptor using the formula $F^D = k^{DA}w^D + k^{AD}w^A Q^D/Q^A$, where all the symbols are as defined in section 3.1.4. Then we calculated the average donor fluorescence in the absence of FRET. In order to obtain an order of magnitude estimate of the donor concentration inside the cells, we used the following expression, derived from the expression for the number of photons generated by a two-photon absorption process (71):

$$C_x = C_s \left[\frac{F^x \sigma_s Q_s t d_s {NA_s}^4 {P_s}^2 {f_s}^2 \tau_x {\lambda_x}^2}{F^s \sigma_x Q_x t d_x {NA_x}^4 {P_x}^2 {f_x}^2 \tau_s {\lambda_s}^2} \right], \qquad (4.1)$$

where C is the molar concentration, F is the average fluorescence intensity of the donors in the absence of energy transfer, σ is the two-photon absorption cross-section, Q is the quantum yield, td is the pixel dwell time of the scanning system, NA is the numerical aperture of the microscope objective, P is the average excitation light power, f is the

repetition rate of the laser pulse, τ is the laser pulse duration (50 fs for the KM Labs laser used in the FRET study and 170 fs for the MaiTaiTM laser used for concentration calibration—see below), and λ is the excitation wavelength, while the subscripts s and x stand for standard solution and for the unknown concentration (of donor-tagged molecules). The average fluorescence intensity of a fluorescent standard consisting of an aqueous solution of YFP (10 μM concentration) was determined using a separate microscope Zeiss Axio Observer (Zeiss, Thornwood, NY) equipped with an OptiMiSTM module (Aurora Spectral Technologies, Bayside, WI) and an ultrashort-pulse laser (MaiTaiTM, Spectra Physics, Santa Clara, CA) tuned to 960 nm. The solution of YFP was prepared as described elsewhere (68). The absorption cross sections and the quantum yields were obtained from the literature (69, 72).

Using this method, we estimated the donor concentrations, which varied between 1.1 and 2.5 x 10^5 molecules per cell, for doxycycline concentrations ranging from 0.5 to 100 ng mL^{-1}. The ratios of donor to acceptor concentrations determined from fitting the bar chart of peak areas allowed us to then compute the concentration of acceptors, which varied between 1.9 x 10^5 and 7.1 x 10^4 molecules per cell as the doxycycline concentration was changed between 0.5 to 100 ng mL^{-1}. From this, the total expression level of M_3R was determined to only slightly vary from just under 3 x 10^5 to 3.2 x 10^5 receptors per cell with doxycycline concentration.

4.2.2.9 Fitting of FRET efficiency distributions to quaternary structure models

The E_{app} histograms obtained as described above were simulated with various quaternary structure models using Microsoft Excel. The best fit of the model to the experimental data was achieved by minimizing the fitting residual defined as:

$$es = \frac{\sum_i |Experimental_i - Simulated_i|}{\sum_i (Experimental)_i}, \qquad (4.2)$$

where *'Experimental'* stands for the experimentally observed number of occurrences of a certain FRET efficiency value (plotted on the vertical axis in the histograms), *'Simulated'* is the simulated value for the *'Experimental'* data, and *'i'* is a summation index corresponding to individual data points.

The bar chart representing the average areas under the peaks in the histograms at a certain doxycycline concentration were fitted with the simulated rhombus tetramer model by minimizing the following fitting residual:

$$Res = \sum_j \left(Experimental_j - Simulated_j\right)^2, \qquad (4.3)$$

where *'j'* is the bar number in the graph (*j*=1,3,4,5, i.e., starting from left and excluding the second peak), *'Experimental$_j$'* is the height of a certain bar, *'j'*, which represents the average cumulative area under the Gaussian corresponding to the j^{th} peak for all the cells, and *'Simulated$_j$'* represents the predicted height for each bar, according to the model described in the Fig. 4.2 caption.

4.2.3 Results

4.2.3.1 Determination of the largest quaternary structure of M_3R at the plasma membrane

We have previously generated (63) Flp-In™ T-REx™ 293 cells to constitutively express an N-terminally FLAG epitope-tagged form of the human M_3R that had the yellow fluorescent protein Citrine linked in-frame to its C-terminal tail (FLAG-M_3R-Citrine). These cells also harbor at the Flp-In™ T-REx™ locus a N-terminally Myc epitope-tagged form of the M_3R with the cyan fluorescent protein Cerulean at the C-terminus and in which the ligand binding pocket had been engineered by mutation of two residues to allow selective activation by the synthetic chemical clozapine N-oxide (CNO) rather than the natural ligand acetylcholine (Myc-Tyr149Cys, Ala239GlyM_3R-Cerulean). The Flp-In™ T-REx™ locus allows expression of different amounts of (Myc-Tyr149Cys, Ala239GlyM_3R-Cerulean) (i.e., donor) to be achieved following addition of varying concentrations of the inducer doxycyline whilst levels of FLAG-M_3R-Citrine remain constant (63). Despite defining the presence of M_3R homomers in these cells upon induction of Myc-Tyr149Cys, Ala239GlyM_3R-Cerulean, previous studies were unable to effectively assess the location, the size of such complexes or their stability over time (63). This cell line therefore provided a direct link to the previous work whilst the pharmacological selectivity of the wild type and variant form of the M_3R allowed potential selective activation of the component parts of identified multimers (see later).

To probe oligomerization of M_3R at the cell surface, we use herein an optical micro-spectroscopic technique and FRET for probing interactions with image-pixel

resolution (54). This method provides distributions of FRET efficiencies for individual cells (rather than average values), avoids information washing caused by diffusion of molecules during the measurements, and is nearly insensitive to stochastic (or bystander) FRET (60), which only introduces a low, broad background in the FRET efficiency distributions (73).

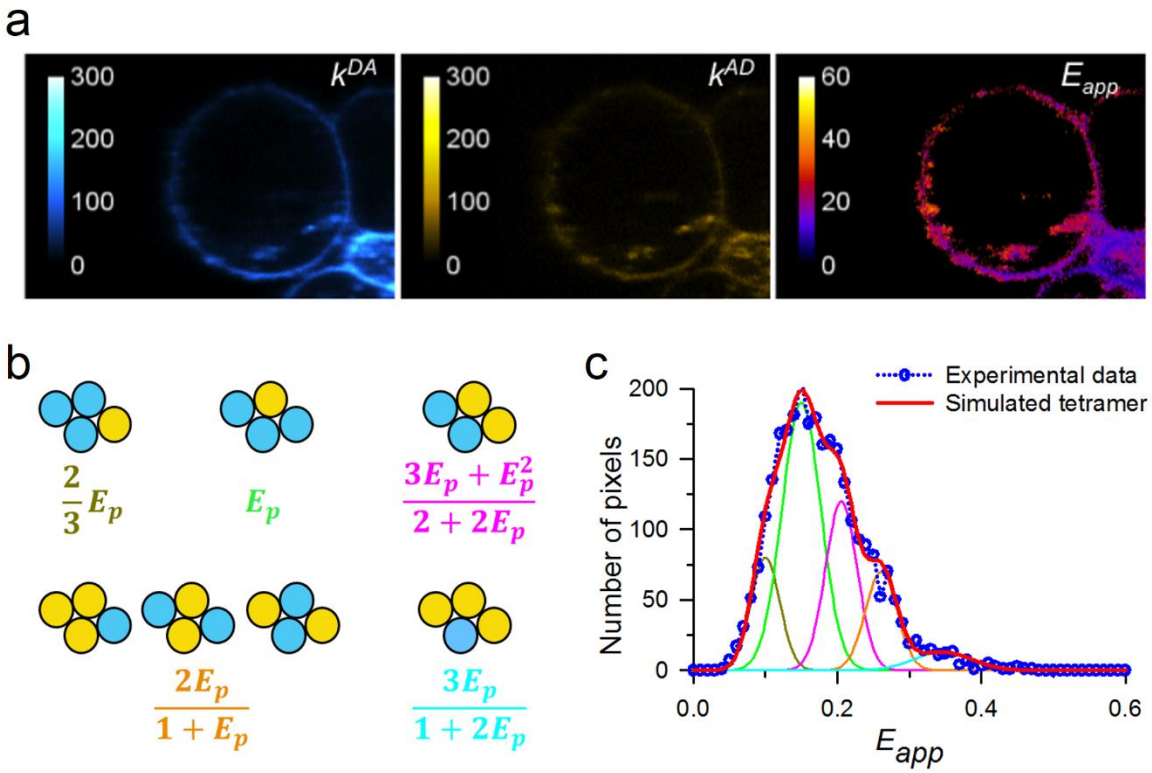

Figure 4.2: FRET-based analysis of Flp-In™ T-REx™ 293 cells expressing Myc-Tyr149Cys, Ala239GlyM$_3$R-Cerulean (inducible) and FLAG-M$_3$R-Citrine (constitutive). **(a)** Photomicrograph of a cell showing donor fluorescence in the presence of acceptor (k^{DA}), acceptor fluorescence in the presence of donor (k^{AD}), and the apparent FRET efficiency distribution map (E_{app}) computed, using Eq. 4.1, from the values of k^{AD} and k^{DA} at each pixel. **(b)** Distinct configurations of donors and acceptors within a parallelogram (or rhombus)-shaped tetramer and their apparent FRET efficiencies. **(c)** E_{app} histograms obtained from pixels representing the plasma membrane of the cell shown in **(a)** (open circles/dotted lines) and the theoretical best fit (thick solid line) with a sum of five correlated Gaussian peaks (shown separately as thin solid lines) whose positions are given by a single adjustable parameter, E_p (=0.18) via the rhombus tetramer model shown in **(d)**. This figure was reproduced from (74)

Initially, individual Flp-In™ T-REx™ 293 cell lines with induced expression of only Myc-Tyr149Cys, Ala239GlyM_3R-Cerulean (energy donor) or only FLAG-M_3R-Citrine (energy acceptor) were imaged to determine the elementary spectra of donors and acceptors. These elementary spectra were used to unmix spectrally-resolved images of cells expressing both donors and acceptors to obtain donor fluorescence intensity in the presence of acceptors (k^{DA}) and acceptor fluorescence intensity in the presence of donors (k^{AD}), as described in section 4.2.2.7. Co-expression of differing ratios of Myc-Tyr149Cys, Ala239GlyM_3R-Cerulean and FLAG-M_3R-Citrine was accomplished by inducing these cells for 24 hours in the presence of different concentrations of doxycycline. Fig. 4.2 (a) shows k^{DA} and k^{AD} images of a representative cell expressing both variants of M_3R as well as the spatial map of apparent FRET efficiencies (E_{app}) as computed from the k^{DA} and k^{AD} images. E_{app} histograms were obtained by binning the E_{app} image pixels according to their value (bin size, 0.01) and plotting the number of pixels in each bin against E_{app} (Fig. 4.2 (c)).

The E_{app} histograms obtained were incompatible with the oligomeric form of the M_3R being a simple dimer, for which a single peak is expected in the histogram (however, please see the Discussion section). The E_{app} histogram for the plasma membrane area of the cell was analyzed using a FRET theory (64) for oligomeric complexes with various sizes and geometries (54, 65). Fig. 4.2 (c) shows the results of a simulation using the parallelogram (or rhombus) tetramer model illustrated in Fig. 4.2 (b). The pair-wise FRET efficiency, characterizing the energy transfer in a single donor and acceptor pair (E_p), was used as an adjustable parameter which determines

simultaneously the positions of the five Gaussian peaks in the experimental data. As seen in Fig. 4.2 (c), the rhombus tetramer properly describes the peaks in the E_{app} histogram of the complexes localized at cell surface.

Simulations using a rhombus hexamer model (presented in Table 4.1) provided similarly good fits. However, of the twenty different peaks predicted by the hexamer model, only those peaks having the same positions as obtained from the simulations with a tetramer were needed to achieve a good, unique fit. That means that, in fact, the rhombus tetramer is the natural result of attempts to fit the data using higher order oligomers.

Table 4.1: E_{app} peaks predicted by a parallelogram hexamer model. This table was reproduced from (74)

Peak Number	E_{app} = f (E_p)	Configurations
1	$\frac{2}{5}E_p$	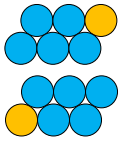
2	$\frac{3}{5}E_p$	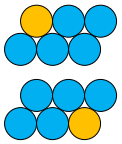
3	$\frac{1}{4}E_p + \frac{1}{2}\frac{E_p}{1+E_p}$	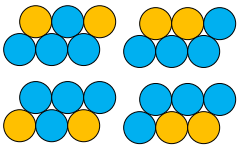
4	$\frac{4}{5}E_p$	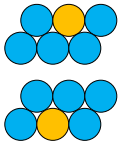

5	$\frac{1}{3}E_p + \frac{2}{3}\frac{E_p}{1+E_p}$	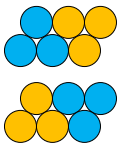
6	$\frac{1}{2}E_p + \frac{1}{2}\frac{E_p}{1+E_p}$	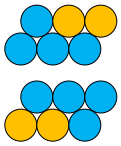
7	E_p	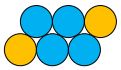
8	$\frac{1}{4}E_p + \frac{E_p}{1+E_p}$	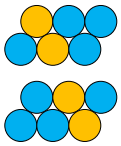
9	$\frac{3}{4}E_p + \frac{1}{2}\frac{E_p}{1+E_p}$	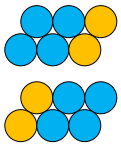
10	$\frac{1}{2}E_p + \frac{E_p}{1+E_p}$	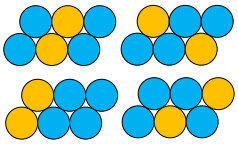
11	$\frac{2}{3}E_p + \frac{E_p}{1+2E_p}$	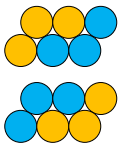
12	$\frac{1}{3}E_p + \frac{4}{3}\frac{E_p}{1+E_p}$	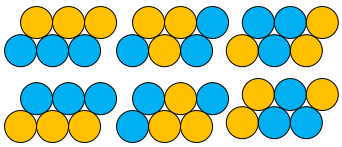
13	$\frac{1}{2}E_p + \frac{3}{2}\frac{E_p}{1+2E_p}$	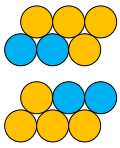
14	$\frac{1}{3}E_p + \frac{2}{3}\frac{E_p}{1+E_p} + \frac{E_p}{1+2E_p}$	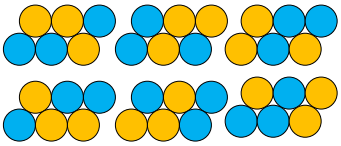

15	$\frac{2E_p}{1+E_p}$	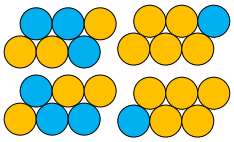
16	$\frac{4}{3}\frac{E_p}{1+E_p}+\frac{E_p}{1+2E_p}$	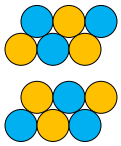
17	$\frac{E_p}{1+E_p}+\frac{3}{2}\frac{E_p}{1+2E_p}$	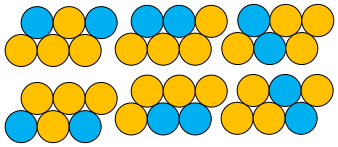
18	$\frac{E_p}{1+E_p}+\frac{2E_p}{1+3E_p}$	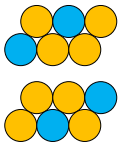
19	$\frac{3E_p}{1+2E_p}$	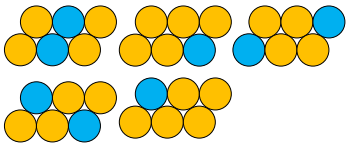
20	$\frac{2E_p}{1+3E_p}$	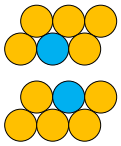

Flp-In™ T-REx™ 293 cells grown on glass coverslips and induced or not to express Myc-Tyr149Cys, Ala239GlyM_3R-Cerulean demonstrated the presence of a substantial proportion of FLAG-M_3R-Citrine at or close to the cell surface in both situations, and the appearance of Myc-Tyr149Cys, Ala239GlyM_3R-Cerulean at a similar location only in doxycycline-induced cells. Merging of such images demonstrated the co-localization of the two forms of M_3R at the level of light microscopy (Fig. 4.3). To ensure that these two forms of M_3R were actually at the plasma membrane with the N-terminal region located extracellularly, and potentially participating in an oligomeric

complex, we employed proximity ligation assays (PLA) using anti-Myc and anti-FLAG antibodies as the primary detection agents. These also confirmed that the two forms of M_3R were in close apposition, and while specificity of the PLA was confirmed by a lack of signal in cells in which expression of Myc-Tyr149Cys, Ala239GlyM_3R-Cerulean had not been induced (Fig. 4.3).

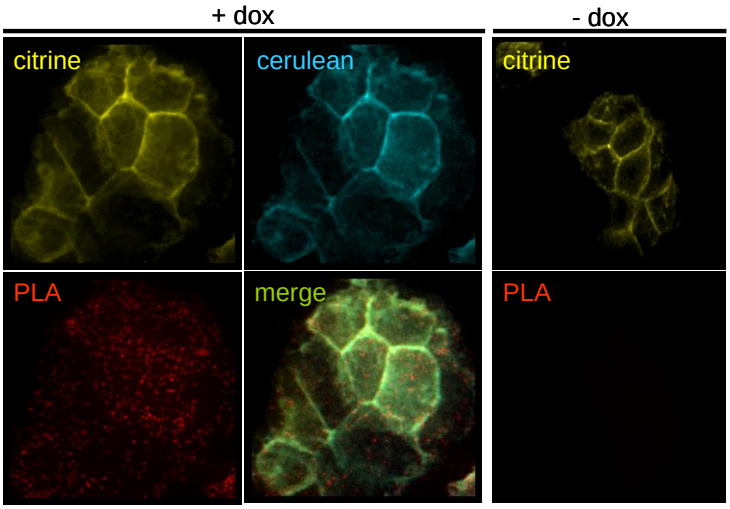

Figure 4.3: Cell surface location and proximity of energy donor and acceptor forms of M_3Rs. Flp-In™ T-REx™ 293 cells expressing FLAG-M_3R-Citrine were uninduced (- dox) or treated with 100 ng mL^{-1} doxycycline (+ dox) for 24 hr to induce expression of and Myc-Tyr149Cys, Ala239Gly M_3R-Cerulean. Images of the individual receptor forms and overlay of images to display co-localization at the cell surface are shown. Proximity ligation assays conducted on doxycycline-induced cells indicated close apposition of the two variants (red) and the extracellular location of the epitope tags while equivalent studies performed on non-induced cells demonstrated the requirement for both variants to be present to generate the signal. This figure was reproduced from (74).

In light of all these findings, and with the application of Occam's razor, we hypothesize that the rhombus tetramer is the largest quaternary structure formed by M_3Rs at the plasma membrane. Separate control experiments, which incorporated FRET standards, confirmed that the detected oligomers are not artifacts potentially introduced by the present methods (54, 75, 76).

4.2.3.2 Do tetramers represent the only quaternary structure at the plasma membrane?

Next, we assessed whether smaller structures (such as dimers and trimers) may coexist with tetramers. By inducing the cells with different doxycycline concentrations (0.5 ng mL^{-1}, 1.0 ng mL^{-1}, 10.0 ng mL^{-1}, and 100 ng mL^{-1}), differing ratios of Myc-Tyr149Cys, Ala239Gly M_3R-Cerulean and FLAG-M_3R-Citrine concentrations were achieved in the cells. At least thirty cells for each doxycycline concentration were imaged and their E_{app} histograms were analyzed using the method described above. The areas under each individual Gaussian (with dimensions of pixels x percentage of E_{app} or, simply, pixels) were averaged over all the cells treated with a certain doxycycline concentration, and a bar chart showing such averages for each peak in the histogram was created for each doxycycline concentration (Fig. 4.4). Each bar in the chart represents therefore the average number per cell of certain configurations of donors and acceptors in Fig. 4.2 (b).

Assuming first that the oligomers are exclusively in tetrameric form, the heights of the individual bars in each chart were modelled using a set of mathematical expressions that depend on the number of different permutations within each of the tetrameric configurations shown in Fig. 4.2 (b) (e.g., two for the first configuration, two for the second, four for the third, etc.) as well as the fraction of donor and acceptor concentrations in the tetramers (see the caption to Fig. 4.4). As seen, the simulated bar heights were in agreement with the experimentally determined heights, except for the second bar (corresponding to the second peak in the E_{app} histograms), for which the experimental value exceeded the theoretical prediction by a significant amount. We also

note that the ratio between donor and acceptor concentrations (see the values in Fig. 4.4 caption) increases with an increase in doxycycline concentration, as expected for an increase in donor expression level. This speaks strongly in favor of the validity of the rhombus tetramer model used to analyze the E_{app} histograms, because extraction of the correct donor to acceptor ratio confirms the validity of the mathematical expressions of the amplitudes predicted by the rhombus tetramer. The same conclusion may be drawn by simply noticing that the amplitudes of the peaks 1 and 2 increase with an increase in donor expression level, while the amplitudes of the peaks 4, and 5 decrease, as expected for a rhombus tetramer in which the proportion of the tetramer configurations rich in donors increases with donor expression level at the expense of the configurations rich in acceptors.

The excess in the cumulative amplitudes corresponding to the second peak suggests that an additional population of complexes must be present, which is characterized by only one peak in its E_{app} histogram whose position is determined by the same pair-wise FRET efficiency (E_p) as for the tetramers. The only possible explanation for the observed excess in the area of the second peak of the E_{app} histogram appears to be the co-existence of dimers with tetramers at the membrane. Since trimers should contribute not only to the second but also to the fourth peak (65) in the experimentally determined histogram, we conclude that trimers are absent from our system. Overall, these observations suggest that the dimers and tetramers may dynamically interconvert at the plasma membrane. We will return to this idea later on in this section.

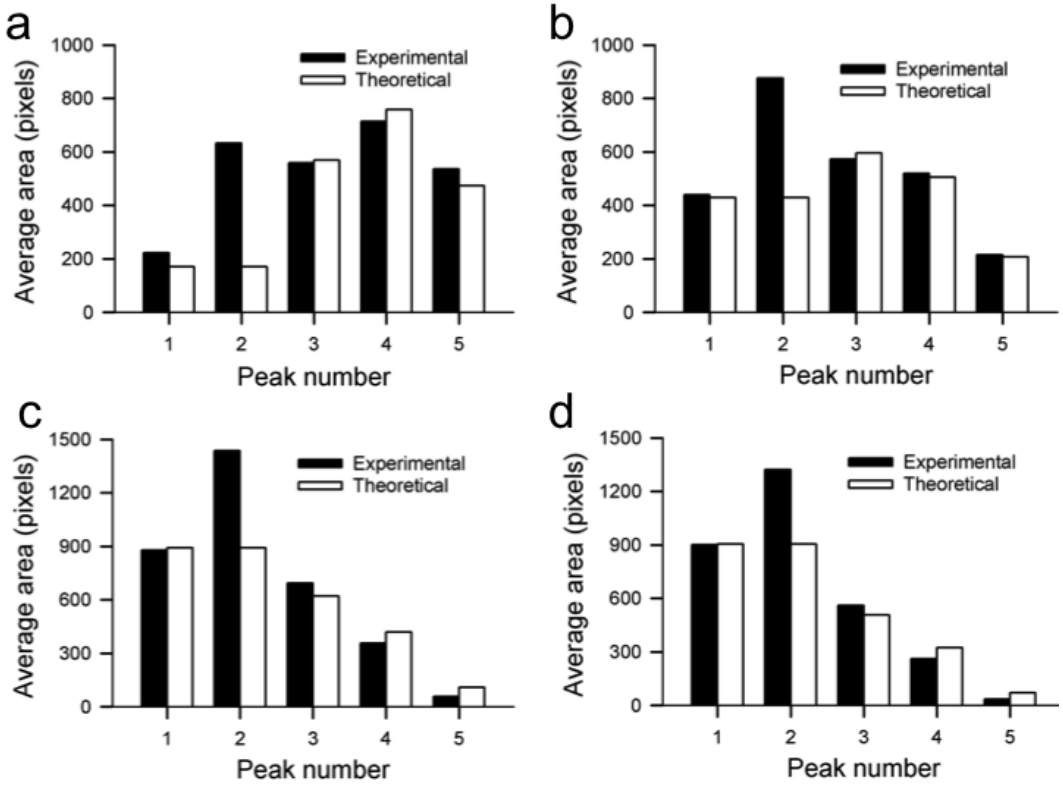

Figure 4.4: Bar charts of the average area under each Gaussian peak in E_{app} histograms. 'Experimental' bars represent the areas under each Gaussian peak in the individual E_{app} histograms, as in Fig. 4.2 (c), averaged over several cells. 'Theoretical' bars represent simulations using amplitudes predicted for the rhombus tetramer model shown in Fig. 4.2 (b). Each bar represents the average number of tetramers per cell corresponding to a certain configuration of donors and acceptors shown in Fig. 4.2 (b). For a tetramer model, the heights of the vertical bars are given by the following family of expressions corresponding to each donor-acceptor configuration shown in Fig. 4.2 (b): $2{P_D}^3{P_A}^1 s$, $2{P_D}^3{P_A}^1 s$, $4{P_D}^2{P_A}^2 s$, $(2{P_D}^1{P_A}^3 + {P_D}^2{P_A}^2 + {P_D}^2{P_A}^2)s$, and $2{P_D}^1{P_A}^3 s$, where s is a scaling factor, while $P_D = \frac{[D]/[A]}{1+[D]/[A]}$ and $P_A = \frac{1}{1+[D]/[A]}$ are the fractions of donors and acceptors, respectively, in complexes, with [D] being the concentration of donors and [A] the concentration of acceptors. Each panel in the figure corresponds to different donor expression levels, as induced by the following doxycycline concentrations: Panel **(a)**: 0.5 ng mL^{-1}; Panel **(b)**: 1.0 ng mL^{-1}; Panel **(c)**: 10.0 ng mL^{-1}; Panel **(d)**: 100.0 ng mL^{-1} (see ref (63) for details). The theoretical simulations for the bar heights were performed simultaneously for peaks 1, 3, 4, and 5 by adjusting the D to A concentration ratio and the scaling factor *s*. The best-fit values for [D]/[A] and *s* were, respectively: 0.60 and 2587 (N = 36 cells) for panel **(a)**; 1.44 and 2548 (N = 85 cells) for panel **(b)**; 2.87 and 4231 (N = 90 cells) for panel **(c)**; 3.57 and 4342 (N = 113 cells) for panel **(d)**. This figure was reproduced from (74).

Having established the identity of the oligomeric structures present at the plasma membrane, we next used the observed excess in the height of the second bar in the charts

(relative to the prediction by the tetramer model) to determine the ratio between the number of protomers associated into dimers with mixed composition (i.e. with both donor- and acceptor-tagged receptors) *vs.* those in tetramers with mixed composition. This was computed as the ratio between the excess height (i.e., experimental minus predicted value) of the second bar times two (because a dimer contains two protomers) and the sum of the heights of the five simulated bars in the individual charts multiplied by four (because each tetramer contains four protomers). The results corresponding to the four panels in Fig. 4. 3 are, in order from A to D: 0.11, 0.10, 0.09, and 0.08.

Beyond a desire to use the same cell lines that had been used previously to define that M_3R formed some element of quaternary structure (63), the combination of wild type and the mutationally modified M_3R in these cells allowed distinct and independent estimates of the levels of expression of the receptors in these studies. Specific radioligand binding using [^{3}H]QNB allowed selective measurement of the acceptor species (FLAG-M_3R-Citrine) as this ligand does not bind with high affinity to Myc-Tyr149Cys, Ala239GlyM_3R-Cerulean (63), and this was complemented by determination of the expression level of donor-tagged receptor, which was based on micro-spectroscopic measurements. Based on determinations of the donor fluorescence intensity corrected for loss through FRET, as described in section 4.2.1.8, in this work we estimated the donor to be present to between 1 x 10^5 and 2.5 x 10^5 molecules per cell for doxycycline concentrations ranging from 0.5 to 100 ng mL^{-1} (see section 4.2.1.8). The ratios of donor to acceptor concentrations determined from fitting the bar chart for peak areas (Fig. 4.4), together with the determined concentrations of donors, allowed us to estimate the

concentrations of acceptors, which varied between 2 x 10^5 and 7 x 10^4 molecules per cell as the doxycycline concentration was changed between 0.5 and 100 ng mL^{-1}. Importantly, these values are very similar to the number of acceptor-tagged copies per cell (~2 x 10^5) determined from binding of the highly-specific [^{3}H]QNB ligand to the acceptor (FLAG-M_3R-Citrine) in the absence of doxycycline. The total expression level of receptor was about 3 x 10^5 receptors per cell, almost independent of doxycycline concentration. This is consistent with the almost constant ratio of dimer to tetramer concentration (see previous paragraph).

4.2.3.3 Quaternary structure of M_3R at the plasma membrane in the presence of agonists

In separate experiments, we took batches of cells induced by 10 ng mL^{-1} of doxycycline to coexpress both forms of the receptor and separated them into three aliquots: One sample was treated with CNO (100 μM for 5-20 minutes), which acts as a highly selective agonist for Myc-Tyr149Cys, Ala239GlyM_3R-Cerulean (63, 77), another sample was treated with carbachol (100 μM), a stable mimetic of the natural M_3R receptor ligand acetylcholine, while an untreated one was used as a control. We imaged the cells as described before and then analyzed the E_{app} histograms using the rhombus tetramer model shown in Fig. 4.2 (b). The E_p values obtained for various cells treated with ligand fell in the same range of values as that corresponding to the untreated cells; this suggested that both the global geometry of the complexes and the distances between their protomers remain largely unaffected upon binding of an agonist ligand. Next, we generated bar charts by adding together the average areas under the Gaussian peaks (Fig.

4.5) and determined the ratios of protomer concentrations in dimers and tetramers from the excess in height of peak #2 in the bar chart (see previous paragraph for details of this procedure), which were 0.16, 0.09, and 0.09 for carbachol-treated, CNO-treated and untreated cells, respectively.

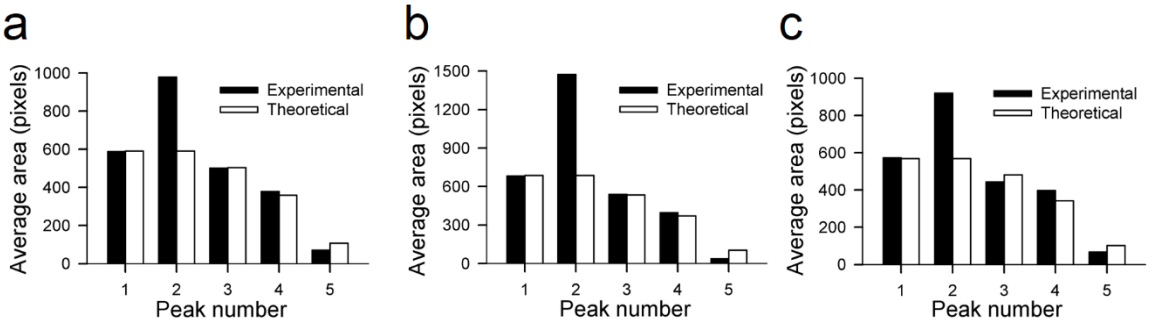

Figure 4.5: Bar charts showing the cumulative areas under each Gaussian peak in E_{app} histograms as in Fig. 4.2 (c) for multiple cells in presence and absence of ligand ('Experimental') and simulations using amplitudes predicted for the parallelogram model shown in Fig. 4.2 (b) ('Theoretical') in the main text. Panel **(a)**: control cells induced with 10 ng mL^{-1} of doxycycline. Panel **(b)**: cells induced with 10 ng mL^{-1} of doxycycline and treated with CNO ligand, which acts as a highly specific agonist only for the Myc-Tyr149Cys, Ala239GlyM_3R-Cerulean energy donor form of the receptor. Panel **(c)**: cells induced with 10 ng mL^{-1} of doxycycline and treated with carbachol, an agonist that binds to the wild-type receptor (FLAG-M_3R-Citrine). The theoretical simulations for the bar heights were performed simultaneously for all five bars by adjusting [D]/[A] and the scaling factor *s*. The best-fit values for [D]/[A] and *s* were, respectively: 2.36 and 2760 (N = 44 cells) for panel **(a)**; 2.35 and 2866 (N = 42 cells) for panel **(b)**; 2.57 and 3289 (for 25 cells) for panel **(c)**. The ratios of protomer concentrations in dimers and tetramers (see main text for details of how these were determined) which were 0.09 for panel **(a)**, 0.09 for panel **(b)**, and 0.16 for panel **(c)**. This figure was reproduced from (74).

Because of the variability of this ratio (from 0.09 to 0.15) observed in several experiments even in the absence of ligand, at this time we choose to not assign any significance to the slight differences between the partitions of protomers among dimers and tetramers in the presence and absence of the selective agonist ligands. The precise interpretation of these results is further complicated by the fact that although saturation binding experiments indicate that the wild-type M_3 receptor binds CNO with an affinity

of ~15 μM (see Table 4.1 in reference (78)), the receptor does not generate a response to this concentration of CNO (see Fig. 4.1 in (77)). More detailed experiments would need to be conducted in the future to more clearly determine whether ligand binding has significant effect on the dimer/oligomer fraction.

4.2.3.4 Testing the stability of the oligomeric complexes

Since our FRET measurements suggested that M_3Rs form rhombus-shaped tetramers as well as dimers at the plasma membrane, we hypothesized that tetramers of M_3R may be meta-stable complexes, although it is widely accepted that oligomeric organization is initiated during the processes of protein synthesis and maturation (58). We used co-immunoprecipitation studies to assess whether recently synthesized receptors would rapidly form stable oligomeric complexes, or whether such complexes might represent transient species that can interchange. To do so, we took advantage of the ability to treat the cells with the *de novo* N-glycosylation inhibitor tunicamycin to allow the separate identification of recently synthesized and longer lived copies of M_3R. Initially, to ensure that elimination of N-glycosylation did not prevent cell surface delivery of the M_3R, untreated and tunicamycin-treated cells that were induced to express Myc-Tyr149Cys, Ala239GlyM_3R-Cerulean were subjected to biotinylation to identify cell surface receptor proteins. Biotinylated proteins were isolated and then resolved by SDS-PAGE. Detection of biotinylated anti-Myc immunoreactivity in samples from both untreated (110 kDa) and tunicamycin-treated (90 kDa) cells defined whether the receptor had been present at the cell surface. The observed ratio of biotinylated N-glycosylated and non-glycosylated M_3R was similar to their proportions in total cell lysates (Fig. 4.6 (a)); this indicated that

prevention of N-glycosylation does not interfere with cell surface delivery of this receptor. Myc-Tyr149Cys, Ala239GlyM_3R-Cerulean was then immunoprecipitated from cells that were concurrently doxycycline-induced and tunicamycin-treated. Following SDS-PAGE, immunoblotting such samples with anti-FLAG identified both non-glycosylated and N-glycosylated forms of FLAG-M_3R-Citrine associated with Myc-Tyr149Cys, Ala239GlyM_3R-Cerulean (Fig. 4.6 (b)).

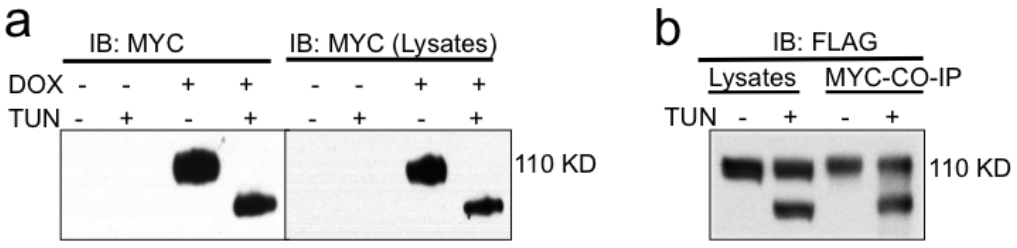

Figure 4.6: Interactions between M_3R protomers synthesized at different times **(a)** Cell surface proteins were labeled with biotin and, after their capture with streptavidin, these were resolved by SDS-PAGE and anti-Myc reactivity monitored (left-hand panel). Total lysates of such cells were resolved and anti-Myc reactivity measured (right-hand panel). **(b)** Flp-In™ T-REx™ 293 cells were treated with 100 ng mL^{-1} doxycycline to induce expression of Myc-Tyr149Cys, Ala239GlyM_3R-Cerulean for a 24 hour period. Tunicamycin treatment was maintained during the entire induction period to prevent N-glycosylation of newly synthesized proteins. Anti-Myc immunoprecipitates were resolved by SDS-PAGE and immunoblotted with anti-FLAG. The presence of N-glycosylated FLAG-M_3R-Citrine as well as the non-glycosylated form in these immunocomplexes is shown. This figure was reproduced from (74).

Based on the earlier studies, the presence of the N-glycosylated form in anti-Myc immunoprecipitates must reflect a complex that now contains a FLAG-tagged form of the receptor synthesized prior to induction of expression of Myc-Tyr149Cys, Ala239GlyM_3R-Cerulean. Because both forms of the FLAG-tagged receptor are immunoprecipitated with an anti-Myc antibody this demonstrates that induced Myc-Tyr149Cys, Ala239GlyM_3R-Cerulean protomers are present in complexes synthesized at

different times. Thus, these results confirm that the oligomeric nature of the complexes is non-permanent, and that the dimers and tetramers can interconvert.

4.2.4 Discussion

4.2.4.1 The M_3R exists as a mixture of dimers and tetramers at the cell surface

By co-expressing differing ratios of Myc-Tyr149Cys, Ala239GlyM_3R-Cerulean and FLAG-M_3R-Citrine in living cells and using spectrally resolved FRET we determined apparent FRET efficiency (E_{app}) histograms, reflecting oligomers of these forms of M_3R located in regions at or near the plasma membrane. The broad histograms obtained were rich in information that could only be defined by organization of the M_3R within a rhombic tetramer and were incompatible with the oligomeric form of the M_3R being limited to a simple dimer, for which a single peak is expected (54, 65). By using this method to analyze data from numerous cells expressing donor-tagged receptors at various levels, the computed areas under each individually described Gaussian were averaged over all cells, and bar charts displaying the average number of oligomers corresponding to each of the five anticipated donor-acceptor configurations of a rhombus tetramer were created for each of four donor expression levels. We modelled the expected contributions of the component bars using a simple model that takes into account the ratio between donor and acceptor concentrations, and this was subsequently compared to the experimental data. This ratio was observed to increase with increasing doxycycline concentrations, as expected for an increase in donor expression level. This provided further support to our observation that the largest quaternary structure of M_3R at the plasma membrane was a rhombus tetramer.

Despite this, the analyses of the experimental data clearly indicated a marked excess in the amplitude of the second peak in the E_{app} histogram compared to that anticipated if the oligomeric M_3R existed solely as a rhombic tetramer. This experimental excess could only be accounted for in models that allow dimers, but not trimers or other oligomeric sizes, to also be present. In support of dynamic interconversion between such oligomeric states over time, co-immunoprecipitation assays suggested that receptors synthesized at different times can be detected in the same oligomer and, therefore, that such complexes are transient in nature and able to interchange protomers. Furthermore, by extension, the absence of M_3R trimers in the plasma membrane as indicated by the E_{app} histogram data implies that protomers do not associate into tetramers one at a time, but rather as dimeric pairs. These observations lead to the conclusion that the molecular bonds within dimers are probably rather strong and suggest that no species with an odd number of protomers are likely to exist under physiological conditions; this excludes both monomers and trimers from the mix. Clearly, non-covalent bonds between the protomers of a receptor dimer can be broken, as a range of studies have produced and purified monomeric G-protein coupled receptors for both biophysical and biochemical analysis (79, 80). Despite this, our results suggest for the first time that dimers may be the smallest structural unit in which M_3R exist at the plasma membrane, and that the dimers associate reversibly to form tetramers. No direct evidence for hexamers or further higher-order oligomers was obtained in these studies. This may indicate that the tetramer is the highest-order structure of the M_3R.

Although our interpretation of the data as presented above appears to be self-consistent, one could, in principle, argue that combinations of dimers and free donors (or donor-only dimers) in our samples may have given the appearance of a combination of dimers and rhombus-shaped tetramers. This possibility, while often mentioned in discussions on this topic, is actually rather easily dismissed. Numerical simulations previously performed by some of us did indeed indicate that the presence of non-interacting free donors in the same excitation volume with a mixed dimer composed of a donor and an acceptor leads to a reduction in the amplitude of the dimer peak in the E_{app} histogram and an appearance of a broader distribution of FRET efficiencies towards values lower than those of the dimer (73). However, no clearly individualized peak (apart from that of the dimer) emerged from those simulations, and the rather amorphous distribution of FRET efficiencies observed at values lower than that of the dimer ended abruptly on the upper end of the E_{app} scale. These features are at variance with the histograms obtained in the present study which show multiple peaks whose amplitudes decrease gradually towards the higher end of the E_{app} distributions. We conclude that our results are inconsistent with a combination of monomers (or just donor-only dimers) and donor-acceptor dimers, and thus our proposal for mixtures of stable dimers and dynamic tetramers continues to stand.

The concept that a dimer may be the minimal *in situ* configuration of a GPCR is supported by recent work at single particle level which concluded that the serotonin 5-HT_{2C} receptor is present as a dimer at the plasma membrane but not as a monomer (81). Notably, however, the same study was also unable to detect tetramers of this receptor.

Furthermore, biochemical analysis of the organization of the orexin OX_1 receptor has recently concluded that this GPCR also exists predominantly as a dimer (82). Moreover, although an earlier single molecule-tracking study on the muscarinic M_1 receptor apparently identified monomer-dimer formation and dissociation (62), these conclusions relied entirely on the view that the ligand used to label the receptor was monitoring monomer-dimer transitions rather than, as suggested herein, potential dimer-tetramer transitions. If all class A GPCRs might be expected to show the same basic homo-oligomerization behavior, the available data (i.e. presence *vs.* absence of tetramers) can be rationalized if receptor expression level in the serotonin 5-HT_{2C} receptor study (81) was substantially lower than in the present study and hence the proportion of dimers to tetramers may have been driven towards a predominance of dimers. This hypothesis could be tested if the overall expression level of the receptors was known in different studies. In the present study, the total concentration of donor- and acceptor-tagged receptors was ~3×10^5 per cell (see the Results section).

4.2.4.2 The ligand does not alter significantly the relative abundance of dimers and tetramers

In addition to determining the quaternary structure of the M_3R, we have also determined that selective agonist binding to either of the M_3R receptor forms did not have a significant effect on its structure and distribution among different oligomer sizes. While this agrees with the findings of other similar studies (83) (and see (84) for review) we cannot, at this stage, completely eliminate the possibility that ligands may affect the partition between dimers and tetramers under extreme concentration situations. To test

this possibility will necessitate the use of rapid excitation switching to determine total concentrations of receptors in the cells and a way to vary the total expression level of M_3R over a broad range of concentrations. In addition, because agonist ligand binding to M_3R is known to cause rapid conformational changes associated with receptor activation (77), this may mean that the transmembrane domains that undergo conformational changes as a result of activation and those that are involved in protein-protein interfaces binding are distinct from one another. It has also been observed that the binding of an inverse agonist ligand to purified and reconstituted β_2-adrenoceptors could modulate tetrameric organization (83). Future studies should, therefore, attempt to probe such rapid alterations in quaternary structure.

4.2.4.3 A general framework for describing GPCRs oligomerization

In summing up our observations above, we propose a general oligomeric structure model that is consistent with the present results while also emphasizing some of the salient features of GPCR oligomeric structure as noted from the abundant literature. Our model (Fig. 4.7) assumes that there are two different binding sites on each receptor, each of which may be associated with a separate transmembrane domain or group of transmembrane domains. If the interaction between the dissimilar binding sites is much stronger than that between the similar binding sites, the monomers will associate first into stable dimers (Fig. 4.7 (a)); then, the dimers may associate weakly (by comparison to protomers within dimers) to form tetramers with ‘closed’ structures, i.e., structures that cannot grow further (Fig. 4.7 (b)). In addition, these tetramers are predicted to take a rhombic shape (Fig. 4.7 (b)). As discussed above, the M_3R appears to indeed present

these features, i.e., it forms rhombus shaped tetramers, but not hexamers. If, by contrast, each binding site interacts strongly with the site of its own type but weakly with a dissimilar site, the dimers (Fig. 4.7 (c)) can form 'open' tetramers (Fig. 4.7 (d)), i.e., tetramers that can grow into higher order oligomers by successive addition of dimers, as suggested initially by Lopez-Gimenez et al. (85).

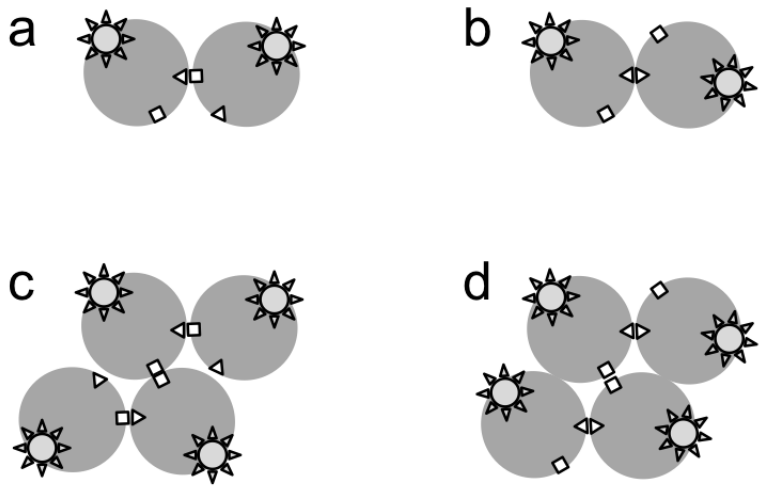

Figure 4.7: A general two-interaction site model of GPCRs. If the strength of the interaction for dissimilar binding sites is very high and exceeds that of similar sites, stable dimers form **(a)** which may associate reversibly into tetramers **(b)**. If similar sites interact strongly and more than the dissimilar sites, stable dimers **(d)** may associate reversibly into open tetramers **(c)**, which may be conducive to higher order structures under certain circumstances. Binding sites are shown as small triangles and squares, and same shapes represent same type of site. The star-shapes in all the structures represent the fluorescent tags, which could be donors and acceptors, or combinations thereof. This figure was reproduced from (74).

An argument can also be made for the existence of a third possibility, which is in fact a particular case of the first two - that of indistinguishable binding sites. In this case, dimers and tetramers may coexist with monomers and trimers. Also in this case, whether the receptors may form oligomers with open or closed configurations may depend on secondary factors, such as additional nonspecific interactions, concentration, and

temperature. In fact, these factors may also alter the degree of association between the two types of dimers illustrated in Fig. 4.7, but they would not be decisive with regard to whether the higher order oligomer has a closed or open structure.

Our proposal reconciles published experiments that report different oligomeric sizes or combinations thereof for different receptors and perhaps different expression levels. Further investigations are necessary in order to fully elucidate which receptor exactly falls into which category and also to identify the specific binding sites. Availability of atomic level crystal structures for greater numbers of receptors would provide a tremendous boost to wide-ranging efforts to determine the location of the binding interfaces on individual receptors. The structure of M_3R has been determined very recently (86), while efforts are underway in various labs to determine the crystal structure of other GPCRs.

Only two clear examples identifying interfaces able to form dimers (49) and tetramers (50) as well as their orientation within the dimer/oligomer are currently available. The atomic level structure of the μ-opioid receptor illustrates the potential for dimeric-tetrameric exchange and that the extent of this might be defined by expression levels and local variations in receptor concentration e.g. in distinct regions of the plasma membrane such as cholesterol-rich domains or rafts. The structure (50) shows a dimeric 4-helix bundle interface provided by many of the residues of transmembrane domains V and VI. Such an extensive interface is likely to be highly stable and would provide a basis for the minimum organisation of the receptor being a dimer. However, although clearly

observed in the crystal structures the second interface, provided by amino acids from transmembrane domains I and II and elements of helix 8, is much less extensive, and therefore intrinsically likely to be far less stable. This might well provide a molecular basis for our observations of the co-existence of dimers and tetramers of M_3R within the plasma membrane and the potential for the proportion of each to be determined by receptor expression level. Even though in the current experiments the donor expression level was controlled by induction of expression of the energy donor species, we have not been able to control total expression level over a wide range to allow detailed analysis of this question, although it is noteworthy that the estimated proportion of dimers decreased as we increases expression of the energy donor variant. Given that the M_3R receptor is expressed in high amounts in various smooth muscles and in certain regions of the brain but at lower levels in tissues such as salivary gland and pancreatic beta cells (87) it may be that the steady-state distribution between dimers and tetramers will vary in different cells and tissues.

References:

1. Milligan G & Kostenis E (2006). Heterotrimeric G-proteins: a short history. *Br J Pharmacol* 147 Suppl 1:S46-55.

2. Dale Purves GJA, David Fitzpatrick, William C. Hall, Anthony-Samuel LaMantia, Leonard E. White (2008). Neuroscience (Sinauer Associates) 4th Ed.

3. Hepler JR & Gilman AG (1992). G proteins. *Trends Biochem Sci* 17(10):383-387.

4. Rens-Domiano S & Hamm HE (1995). Structural and functional relationships of heterotrimeric G-proteins. *FASEB J* 9(11):1059-1066.

5. Sprang SR (1997). G protein mechanisms: insights from structural analysis. *Annu Rev Biochem* 66:639-678.

6. Kobilka BK (2007). G protein coupled receptor structure and activation. *Biochim Biophys Acta* 1768(4):794-807.

7. Milligan G (2007). G protein-coupled receptor dimerisation: molecular basis and relevance to function. *Biochim Biophys Acta* 1768(4):825-835.

8. Escribá PV (2007). G protein-coupled receptors, signaling mechanisms and pathophysiological relevance. *Biochim Biophys Acta* 1768(4):747.

9. Yeagle PL & Albert AD (2007). G-protein coupled receptor structure. *Biochim Biophys Acta* 1768(4):808-824.

10. Lefkowitz RJ (2007). Seven transmembrane receptors: a brief personal retrospective. *Biochim Biophys Acta* 1768(4):748-755.

11. Rosenbaum DM, Rasmussen SG & Kobilka BK (2009). The structure and function of G-protein-coupled receptors. *Nature* 459(7245):356-363.

12. Dorsam RT & Gutkind JS (2007). G-protein-coupled receptors and cancer. *Nat Rev Cancer* 7(2):79-94.

13. Attwood TK & Findlay JB (1993). Design of a discriminating fingerprint for G-protein-coupled receptors. *Protein Eng* 6(2):167-176.

14. Davies MN, et al. (2007). On the hierarchical classification of G protein-coupled receptors. *Bioinformatics* 23(23):3113-3118.

15. Fredriksson R, Lagerstrom MC, Lundin LG & Schioth HB (2003). The G-protein-coupled receptors in the human genome form five main families. Phylogenetic analysis, paralogon groups, and fingerprints. *Mol Pharmacol* 63(6):1256-1272.

16. Lagerstrom MC & Schioth HB (2008). Structural diversity of G protein-coupled receptors and significance for drug discovery. *Nat Rev Drug Discov* 7(4):339-357.

17. Birnbaumer L & Brown AM (1990). G proteins and the mechanism of action of hormones, neurotransmitters, and autocrine and paracrine regulatory factors. *Am Rev Respir Dis* 141(3 Pt 2):S106-114.

18. Arai K, et al. (1978). Studies on polypeptide-chain-elongation factors from an extreme thermophile, Thermus thermophilus HB8. 1. Purification and some properties of the purified factors. *Eur J Biochem* 92(2):509-519.

19. Higashijima T, Ferguson KM, Sternweis PC, Smigel MD & Gilman AG (1987). Effects of Mg2+ and the beta gamma-subunit complex on the interactions of guanine nucleotides with G proteins. *Journal of Biological Chemistry* 262(2):762-766.

20. Lee E, Taussig R & Gilman AG (1992). The G226A mutant of Gs alpha highlights the requirement for dissociation of G protein subunits. *Journal of Biological Chemistry* 267(2):1212-1218.

21. Birnbaumer L (2007). The discovery of signal transduction by G proteins: a personal account and an overview of the initial findings and contributions that led to our present understanding. *Biochim Biophys Acta* 1768(4):756-771.

22. Jähnichen S (Activation cycle of G-proteins by G-protein-coupled receptors, http://commons.wikimedia.org/wiki/Commons:GNU_Free_Documentation_License_1.2, Wikimedia Commons, the free media repository, http://commons.wikimedia.org/wiki/File:GPCR-Zyklus.png#file.

23. Ishii M & Kurachi Y (2006). Muscarinic acetylcholine receptors. *Curr Pharm Des* 12(28):3573-3581.

24. Riker WF, Jr. & Wescoe WC (1951). The pharmacology of Flaxedil, with observations on certain analogs. *Ann N Y Acad Sci* 54(3):373-394.

25. Peralta EG, et al. (1987). Distinct primary structures, ligand-binding properties and tissue-specific expression of four human muscarinic acetylcholine receptors. *EMBO J* 6(13):3923-3929.

26. Bonner TI, Young AC, Brann MR & Buckley NJ (1988). Cloning and expression of the human and rat m5 muscarinic acetylcholine receptor genes. *Neuron* 1(5):403-410.

27. Wess J (1996). Molecular biology of muscarinic acetylcholine receptors. *Crit Rev Neurobiol* 10(1):69-99.

28. Caulfield MP & Birdsall NJM (1998). International Union of Pharmacology. XVII. Classification of muscarinic acetylcholine receptors. [Review] [146 refs]. *Pharmacol Rev* 50(2):279-290.

29. Nathanson NM (2000). A multiplicity of muscarinic mechanisms: enough signaling pathways to take your breath away. *Proc Natl Acad Sci U S A* 97(12):6245-6247.

30. Lanzafame AA, Christopoulos A & Mitchelson F (2003). Cellular signaling mechanisms for muscarinic acetylcholine receptors. *Receptors Channels* 9(4):241-260.

31. Wess J, Eglen RM & Gautam D (2007). Muscarinic acetylcholine receptors: mutant mice provide new insights for drug development. *Nat Rev Drug Discov* 6(9):721-733.

32. Weber S, et al. (2011). Muscarinic Acetylcholine Receptor M3 Mutation Causes Urinary Bladder Disease and a Prune-Belly-like Syndrome. *Am J Hum Genet* 89(5):668-674.

33. Delaleu N, Immervoll H, Cornelius J & Jonsson R (2008). Biomarker profiles in serum and saliva of experimental Sjogren's syndrome: associations with specific autoimmune manifestations. *Arthritis Res Ther* 10(1):R22.

34. He J, et al. (2012). The role of muscarinic acetylcholine receptor type 3 polypeptide (M3RP205-220) antibody in the saliva of patients with primary Sjogren's syndrome. *Clin Exp Rheumatol* 30(3):322-326.

35. Wess J (2004). Muscarinic acetylcholine receptor knockout mice: novel phenotypes and clinical implications. *Annu Rev Pharmacol Toxicol* 44:423-450.

36. Hulme EC, Lu ZL & Bee MS (2003). Scanning mutagenesis studies of the M1 muscarinic acetylcholine receptor. *Receptors Channels* 9(4):215-228.

37. Taylor PB, J. H. (2006). Muscarinic receptor agonists and antagonists. The Pharmacological Basis of Therapeutics, ed Goodman LS GA, Hardman JG, Gilman AG, Limbird LE, (McGraw–Hill, New York), pp 183–200.

38. Spalding TA, et al. (2002). Discovery of an ectopic activation site on the M(1) muscarinic receptor. *Mol Pharmacol* 61(6):1297-1302.

39. Langmead CJ, et al. (2006). Probing the molecular mechanism of interaction between 4-n-butyl-1-[4-(2-methylphenyl)-4-oxo-1-butyl]-piperidine (AC-42) and the muscarinic M(1) receptor: direct pharmacological evidence that AC-42 is an allosteric agonist. *Mol Pharmacol* 69(1):236-246.

40. Sur C, et al. (2003). N-desmethylclozapine, an allosteric agonist at muscarinic 1 receptor, potentiates N-methyl-D-aspartate receptor activity. *Proc Natl Acad Sci U S A* 100(23):13674-13679.

41. Haga K, et al. (2012). Structure of the human M2 muscarinic acetylcholine receptor bound to an antagonist. *Nature* 482(7386):547-551.

42. Rosenbaum DM, et al. (2011). Structure and function of an irreversible agonist-beta(2) adrenoceptor complex. *Nature* 469(7329):236-240.

43. Xu F, et al. (2011). Structure of an agonist-bound human A2A adenosine receptor. *Science* 332(6027):322-327.

44. Shimamura T, et al. (2011). Structure of the human histamine H1 receptor complex with doxepin. *Nature* 475(7354):65-70.

45. Lebon G, et al. (2011). Agonist-bound adenosine A2A receptor structures reveal common features of GPCR activation. *Nature* 474(7352):521-525.

46. Moukhametzianov R, et al. (2011). Two distinct conformations of helix 6 observed in antagonist-bound structures of β1-adrenergic receptor. *Proc Natl Acad Sci USA* 108(20):8228-8232.

47. Milligan G (2004). G protein-coupled receptor dimerization: function and ligand pharmacology. *Mol Pharmacol* 66(1):1-7.

48. Angers S, Salahpour A & Bouvier M (2002). Dimerization: an emerging concept for G protein-coupled receptor ontogeny and function. *Annu Rev Pharmacol Toxicol* 42:409-435.

49. Wu B, et al. (2010). Structures of the CXCR4 chemokine GPCR with small-molecule and cyclic peptide antagonists. *Science* 330(6007):1066-1071.

50. Manglik A, et al. (2012). Crystal structure of the micro-opioid receptor bound to a morphinan antagonist. *Nature* 485(7398):321-326.

51. Dorsch S, Klotz KN, Engelhardt S, Lohse MJ & Bunemann M (2009). Analysis of receptor oligomerization by FRAP microscopy. *Nat Methods* 6(3):225-230.

52. Maurel D, et al. (2008). Cell-surface protein-protein interaction analysis with time-resolved FRET and snap-tag technologies: application to GPCR oligomerization. *Nat Methods* 5(6):561-567.

53. Albizu L, et al. (2010). Time-resolved FRET between GPCR ligands reveals oligomers in native tissues. *Nat Chem Biol* 6(8):587-594.

54. Raicu V, et al. (2009). Determination of supramolecular structure and spatial distribution of protein complexes in living cells. *Nature Photon* 3(2):107-113.

55. Pisterzi LF, et al. (2010). Oligomeric size of the M2 muscarinic receptor in live cells as determined by quantitative fluorescence resonance energy transfer. *J Biol Chem* 285(22):16723-16738.

56. Canals M, Lopez-Gimenez JF & Milligan G (2009). Cell surface delivery and structural re-organization by pharmacological chaperones of an oligomerization-defective alpha(1b)-adrenoceptor mutant demonstrates membrane targeting of GPCR oligomers. *Biochem J* 417(1):161-172.

57. Kobayashi H, Ogawa K, Yao R, Lichtarge O & Bouvier M (2009). Functional rescue of β1-adrenoceptor dimerization and trafficking by pharmacological chaperones. *Traffic* 10(8):1019-1033.

58. Milligan G (2010). The role of dimerisation in the cellular trafficking of G-protein-coupled receptors. *Curr Opin Pharmacol* 10(1):23-29.

59. Chabre M & le Maire M (2005). Monomeric G-protein-coupled receptor as a functional unit. *Biochemistry* 44(27):9395-9403.

60. Milligan G & Bouvier M (2005). Methods to monitor the quaternary structure of G protein-coupled receptors. *FEBS J* 272(12):2914-2925.

61. Kasai RS, et al. (2011). Full characterization of GPCR monomer-dimer dynamic equilibrium by single molecule imaging. *J Cell Biol* 192(3):463-480.

62. Hern JA, et al. (2010). Formation and dissociation of M1 muscarinic receptor dimers seen by total internal reflection fluorescence imaging of single molecules. *Proc Natl Acad Sci U S A* 107(6):2693-2698.

63. Alvarez-Curto E, Ward RJ, Pediani JD & Milligan G (2010). Ligand regulation of the quaternary organization of cell surface M3 muscarinic acetylcholine receptors analyzed by fluorescence resonance energy transfer (FRET) imaging and homogeneous time-resolved FRET. *J Biol Chem* 285(30):23318-23330.

64. Raicu V (2007). Efficiency of resonance energy transfer in homo-oligomeric complexes of proteins. *J Biol Phys* 33(2):109-127.

65. Raicu V (2010). FRET-based determination of protein complex structure at nanometer length scale in living cells. Nanoscopy and Multidimensional Optical Fluorescence Microscopy, ed Diaspro A (CRC Press, Boca Raton).

66. Griesbeck O, Baird GS, Campbell RE, Zacharias DA & Tsien RY (2001). Reducing the environmental sensitivity of yellow fluorescent protein. Mechanism and applications. *J Biol Chem* 276(31):29188-29194.

67. Rizzo MA, Springer GH, Granada B & Piston DW (2004). An improved cyan fluorescent protein variant useful for FRET. *Nat Biotechnol* 22(4):445-449.

68. Bishara D & Taylor D (2008). Upcoming agents for the treatment of schizophrenia: mechanism of action, efficacy and tolerability. *Drugs* 68(16):2269-2292.

69. Zipfel WR, Williams RM & Webb WW (2003). Nonlinear Magic: Multiphoton Microscopy in the Biosciences. *Nat Biotechnol* 21(11):1369 - 1377.

70. Svoboda K & Yasuda R (2006). Principles of two-photon excitation microscopy and its applications to neuroscience. *Neuron* 50(6):823-839.

71. Denk W, Strickler JH & Webb WW (1990). Two-photon laser scanning fluorescence microscopy. *Science* 248(4951):73-76.

72. Lowe B, et al. (2003). Detecting panic disorder in medical and psychosomatic outpatients: comparative validation of the Hospital Anxiety and Depression Scale, the Patient Health Questionnaire, a screening question, and physicians' diagnosis. *J Psychosom Res* 55(6):515-519.

73. Singh DR & Raicu V (2010). Comparison between Whole Distribution- and Average-Based Approaches to the Determination of Fluorescence Resonance Energy Transfer Efficiency in Ensembles of Proteins in Living Cells. *Biophys J* 98(10):2127-2135.

74. Patowary S, et al. (2013). The muscarinic M3 acetylcholine receptor exists as two differently sized complexes at the plasma membrane. *Biochem J* 452(2):303-312.

75. Singh DR, et al. (2013). Determination of the quaternary structure of a bacterial ATP-binding cassette (ABC) transporter in living cells. *Integr Biol* 5(2):312-323.

76. Stoneman MR, et al. (2012). Quantifying the efficiency of various FRET constructs using OptiMiS (TM). *Biotechniques* 52(3):191-195.

77. Alvarez-Curto E, et al. (2011). Developing chemical genetic approaches to explore G protein-coupled receptor function: validation of the use of a receptor activated solely by synthetic ligand (RASSL). *Mol Pharmacol* 80(6):1033-1046.

78. Guettier JM, et al. (2009). A chemical-genetic approach to study G protein regulation of beta cell function in vivo. *Proc Natl Acad Sci U S A* 106(45):19197-19202.

79. Kuszak AJ, et al. (2009). Purification and functional reconstitution of monomeric μ-opioid receptors: allosteric modulation of agonist binding by Gi2. *J Biol Chem* 284(39):26732-26741.

80. Damian M, Martin A, Mesnier D, Pin JP & Baneres JL (2006). Asymmetric conformational changes in a GPCR dimer controlled by G-proteins. *EMBO J* 25(24):5693-5702.

81. Herrick-Davis K, Grinde E, Lindsley T, Cowan A & Mazurkiewicz JE (2012). Oligomer size of the serotonin 5-hydroxytryptamine 2C (5-HT2C) receptor revealed by fluorescence correlation spectroscopy with photon counting histogram analysis: evidence for homodimers without monomers or tetramers. *J Biol Chem* 287(28):23604-23614.

82. Xu TR, Ward RJ, Pediani JD & Milligan G (2011). The orexin OX(1) receptor exists predominantly as a homodimer in the basal state: potential regulation of receptor organization by both agonist and antagonist ligands. *Biochem J* 439(1):171-183.

83. Fung JJ, et al. (2009). Ligand-regulated oligomerization of β2-adrenoceptors in a model lipid bilayer. *EMBO J* 28(21):3315-3328.

84. Saenz del Burgo LM, G (2011). Ligand regulation of GPCR quaternary structure. G Protein-Coupled Receptors: From Structure to Function, ed Giraldo J, Pin, J.P. (Drug Discovery Series, RSC Publishing, London), pp 111-152.

85. Lopez-Gimenez JF, Canals M, Pediani JD & Milligan G (2007). The α1b-adrenoceptor exists as a higher-order oligomer: effective oligomerization is required for receptor maturation, surface delivery, and function. *Mol Pharmacol* 71(4):1015-1029.

86. Kruse AC, et al. (2012). Structure and dynamics of the M3 muscarinic acetylcholine receptor. *Nature* 482(7386):552-556.

87. Regard JB, Sato IT & Coughlin SR (2008). Anatomical profiling of G protein-coupled receptor expression. *Cell* 135(3):561-571.

Chapter 5 Conclusion and future direction of work

5.1 Conclusion

As described in chapter 3, we tested the spectral FRET method for determination of quaternary structure of proteins using obligate trimers and tetramers. The results showed that the measured average FRET efficiencies of membrane trimers and cytoplasmic tetramers were same as predicted by the kinetic theory of FRET. We further used the method to determine the quaternary structure of M_3Rs in presence and absence of ligands. Our findings revealed that M_3Rs exist as stable dimers at the plasma membrane while a fraction of it forms transient rhombus tetramers without forming any other oligomers. We didn't see any effect of ligand on the proportion of dimers to tetramers. Based on our findings, we proposed a general framework for GPCR oligomerization that reconcile the published experiments reporting different oligomeric size or combinations for different receptors that can be due to different expression levels of the receptors.

5.2 Future direction of research

5.2.1 Monte Carlo simulations to study protein oligomerization

The FRET spectrometric method developed in our lab and described in the previous chapters is a very powerful tool to study protein-protein interaction for very low expression levels of the proteins of interest, ideally single complexes per pixel. However, the limitations of this method were not investigated fully. For instance, it is important to understand that how the expression level of membrane receptors affects the FRET efficiency histogram. In study started very recently, we have used a Monte Carlo

simulation-based approach that uses the FRET theory described previously (1, 2) to generate E_{app} histograms for different numbers of complexes per pixel. The simulated histogram is then compared with the experimental E_{app} histogram to obtain information on the protein oligomerization and concentration. We have applied the method to study oligomerization of M_3R in the intracellular vesicles based on the known results that M_3Rs mostly form rhombus tetramer complexes on the plasma membrane (3).

In the first step of the simulation, a two-dimensional grid (or lattice) was generated in which the complexes were distributed randomly. The average number of complex per cell in the lattice (or pixel in the E_{app} map) was set as a variable. The E_{app} values at each pixel was calculated individually, and an E_{app} histogram was generated by binning pixels of same E_{app} value (with bin interval = 0.01 in the scale of 1) and plotting them against E_{app}. Based on the simulation results, we observed that the shape and size of the E_{app} histogram changed with the number of complex per pixel (N_{com}).

(i) If $N_{com} \leq 1$, the E_{app} histograms were broad with distinct narrow peaks as predicted by the rhombus tetramer model as shown in Fig. 5.1 (a). The pair-wise FRET efficiency, characterizing the energy transfer in a single donor and acceptor pair (E_p) that determines simultaneously the positions of the five Gaussian peaks of rhombus tetramer model was taken as 0.4. The peak positions of simulated histogram were at 0.27, 0.40, 0.49, 0.57, and 0.67 that were also the peak positions predicted by the rhombus tetramer model for $E_p = 0.4$.

(ii) For $1 < N_{com} \leq 5$, the simulated histograms were usually broad showing continuous distributions of FRET efficiencies and some extra peaks apart from the peaks

predicted by the model. Fig 4.1 (b) shows E_{app} histograms N_{com} = 3 where several peaks appear along with the five peaks predicted by the model with E_p = 0.4.

(iii) For, N_{com} >10, the E_{app} histogram collapses to a single and narrow peak, termed as *"*histogram collapse*"* as shown in Fig 4.1 (c) (for N_{com} = 20). This was due to the mixture of more than a single type of complexes at every pixel giving an average E_{app} value. If the number of complex per pixel is high (>10 as observed from the simulation), the average E_{app} value at each pixel could be similar to the global average value of E_{app} resulting in a single peak. The peak positions in this case, were generally different from that predicted by the model.

After generating the E_{app} histograms at every iteration, the dominant peak position (E_{app} value) of the E_{app} histogram was collected. Thus, a *meta-histogram* was generated using the collected peak positions that represented number of peaks for each E_{app} value (in bin interval of 0.025 in the scale of 1). Since, the *meta-histogram* was obtained from the peak positions in the E_{app} histograms, hence the number and positions of the peaks in the *meta-histogram* also depended on the number of complex per pixels. Similar to the results obtained for E_{app} histogram, the simulated *meta-histogram* resulted in same peak positions as predicted by the model for $N_{com} \leq 1$, however, for $1 < N_{com} \leq 5$, there were certain extra peaks that were not predicted by the model. For N_{com} >10, the *meta-histogram* smeared to a continuous distribution of FRET efficiencies ranging from zero to the highest FRET efficiency predicted by the model.

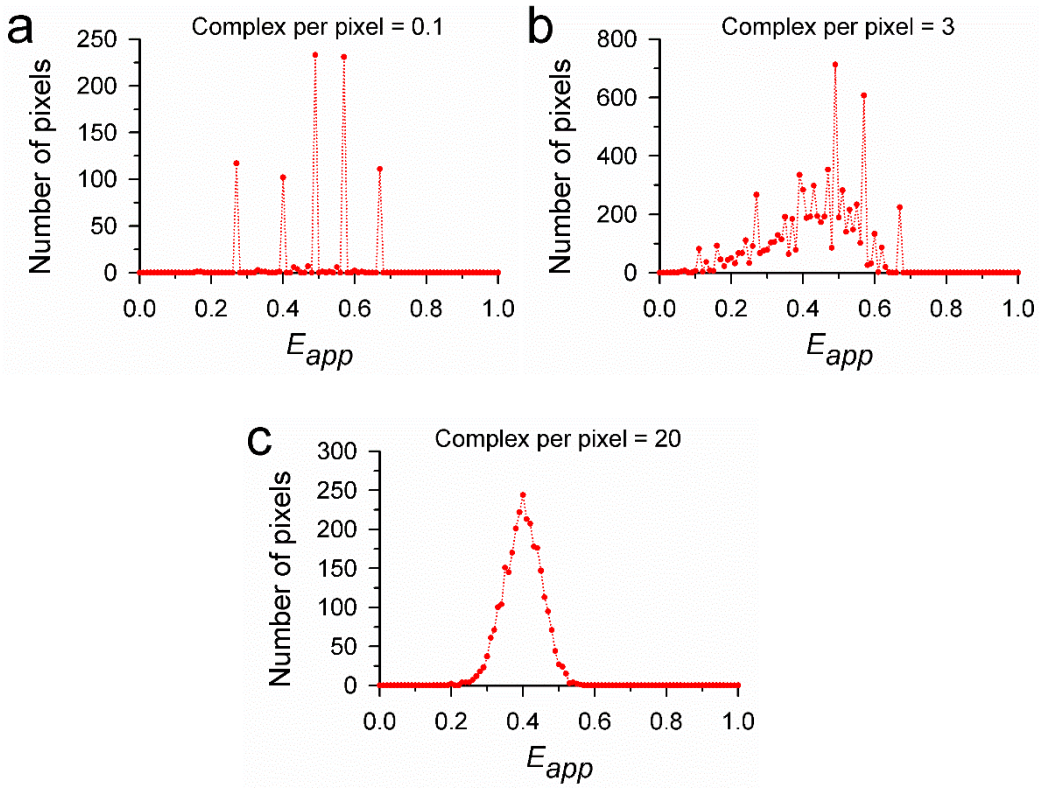

Figure 5.1: Simulated E_{app} histogram of a rhombus tetramer. The pair wise FRET efficiency of a donor-acceptor pair, E_p = 0.4, total number of pixels = 10,000 and number of complex per pixels **(a)** N_{com} = 0.1, **(b)** N_{com} = 3, and **(c)** N_{com} = 20.

Based on the simulated results, we concluded that it is important to have controlled expression of proteins in the systems of study for correct interpretation of the results using the FRET spectrometric method. The current simulation method could not predict the amplitudes of the peaks since the dependence of FRET efficiencies on the fluorophore orientations were not known. Also, the method should be generalized to be applicable for unknown receptors that can exist as differently sized oligomers.

5.2.2 Quaternary structure of M_3R in intracellular vesicles

As described in section 4.2.2, Flp-In™ T-REx™ 293 cells expressing inducible Myc-M_3-Cerulean, and FLAG-M_3-Citrine individually were imaged to obtain the elementary emission spectrum for donor and acceptor respectively. These elementary spectra were used to un-mix the emission spectrum at every pixel of the imaged section of the cell co-expressing inducible Myc-M_3-Cerulean and constitutive FLAG-M_3-Citrine to obtain the donor fluorescence intensity in presence of acceptor (k^{DA}) and acceptor fluorescence intensity in the presence of donors (k^{AD}). Fig. 5.1 (a) shows k^{DA} and k^{AD} images of a representative Flp-In™ T-REx™ 293 cell co-expressing Myc-M_3-Cerulean and FLAG-M_3-Citrine. The images revealed that the intracellular M_3 receptors were localized in what appeared to be individual dot-like structures shown by an arrow in Fig. 5.1 (a)**,** potentially representing endocytic transport vesicles. The average FRET efficiencies of individual dots (i.e., transport vesicle) were calculated from average values of k^{DA} and k^{AD} using equation (3.41), one dot at a time, with $Q^D = 0.62$ (4) and $Q^A = 0.76$ (5). E_{app} histograms (Fig. 5.1(c)) were generated by binning the E_{app} values for all individual dots collected from cells subjected to different doxycycline concentrations (0.1, 1.0, 10.0 and 100.0 ng mL^{-1}) according to their value (bin size, 0.025) and plotting the number of dots in each bin against E_{app}.

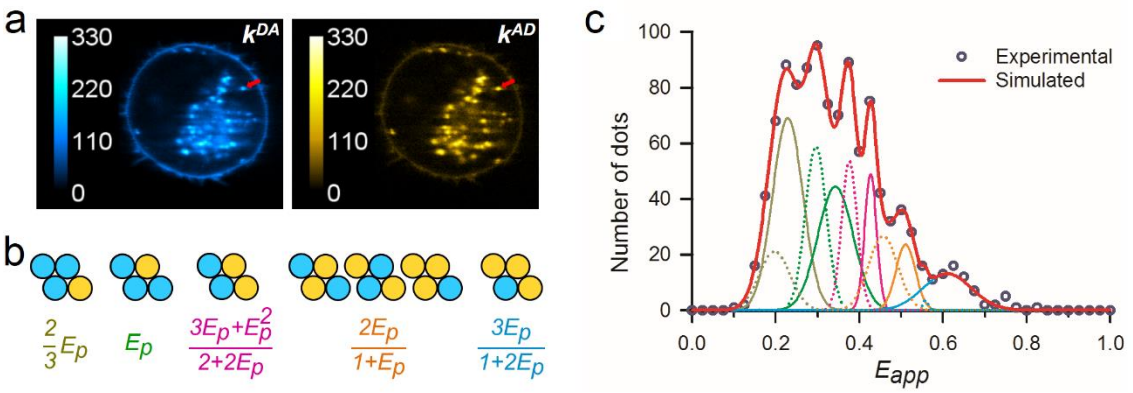

Figure 5.2: Spectral FRET analysis of Flp-In™ T-REx™ 293 cells expressing Myc-M_3R-Cerulean (inducible) and FLAG-M_3R-Citrine (constitutive). **(a)** Photomicrograph of a representative cell showing donor fluorescence intensity in presence of acceptors (k^{DA}) and acceptor fluorescence intensity in presence of donors (k^{AD}). The arrows in each image point to one of the many dot-like structures (potentially transport vesicles) seen within the cytoplasm. **(b)** Possible configurations of donor and acceptors within a rhombus tetramers model predicting five distinct peaks in an apparent FRET efficiency histogram (E_{app}) expressed in terms of pair-wise FRET efficiency E_p. **(c)** Cumulative histogram of apparent FRET efficiencies (E_{app}) calculated from the E_{app} of individual dots. The experimental data (circles) were fitted with two sub-populations of rhombus tetramer model (thick solid lines), each characterized by a single E_p. Thin dotted lines, simulation using E_p = 0.294 and thin solid lines, simulations using E_p = 0.343.

The E_{app} histogram for intracellular complexes was fitted using various models of oligomers with different sizes and geometries (1, 6). The pair-wise FRET efficiency, E_p was used as a fitting parameter which determines the positions of Gaussian peaks in the experimental data. Fig. 4.1 (c) shows the result of simulation using two subpopulations of rhombus tetramer model illustrated in Fig. 4.1 (b). For comparison the experimental E_{app} histogram was also fitted using (i) a general parallelogram tetramer model (ii) mixer of dimers and free donors model, (iii) dimer only model and, (iv) a hexamer model; but based on the lowest fitting residual (see equation 4.3) we propose a combination of two sub-populations of rhombus tetramers as the most likely quaternary structure for the M_3R within intracellular vesicles.

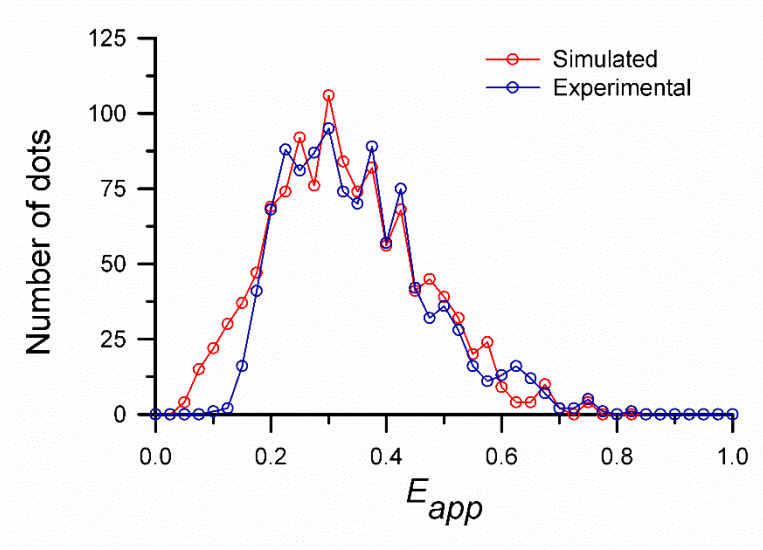

Figure 5.3: Simulation of E_{app} histogram of dots in intracellular vesicles using a rhombus tetramer model using E_p = 0.5 and N_{com} = 5 for total of 1200 dots (transport vesicles).

However, our results could not provide convincing evidence for the presence of two different states of M_3Rs inside the vesicles, which contrasts with the presence of a single state at the plasma membrane. Therefore, we decided to use Monte Carlo simulation method (described in section 5.1) to further investigate whether the appearance of extra peaks in the E_{app} histogram other than the predicted peak positions by a single state is the artifact of presence of more than single complexes inside the vesicles. Fig 5.3 shows the simulation of the experimental E_{app} histogram of dots or vesicles using a rhombus tetramer model as shown in Fig 5.2 (b). The number of complex per dot used to simulate the experimental histogram was 5, and E_p = 0.5. The simulated results showed that the appearance of the peaks in the E_{app} histogram other than the predicted peaks by a rhombus tetramer model was due to the coexistence of more than one complex in the vesicles. However, we were unable to simulate the amplitudes of the peaks in the experimental E_{app} histogram due to the lack of certain information in the method such as

the variation of FRET efficiency due to fluorophore's orientations and the presence of dimers along with the tetramers in certain vesicles.

5.2.3 Quaternary structure of human secretin receptors

Human Secretin receptors (h-SecRs) are members of class B GPCRs and are known to form homo- and hetero-oligomers (7-10), though there are inadequate evidences of existence of secretin receptors as higher order oligomers than dimers. Using FRET spectrometry, we have recently begun to investigate the oligomerization of wild type human secretin receptor (wt-hSecR) and a mutant form of the receptor (mut-hSecR). The mut-hSecR was made to prevent oligomerization by modifying the interacting sites of the wt-hSecR (SecR G243A, I247A) (11). The plasmids DNA used for this study were made in Miller lab, Mayo clinic and is described elsewhere (12). The protocol for sample preparation and imaging is described in section 3.3. In short, wt-hSecR and mut-hSecR tagged with GFP_2 (donor) and YFP (acceptor) were transfected transiently to CHO cells that were cultured overnight. For both wt-, and mut-hSecR, three types of samples were prepared: (i) cells expressing wt/mut-hSecR-GFP_2 to obtain donor spectrum, (ii) cells expressing wt/mut-hSecR-YFP to obtain acceptor spectrum, and (iii) cells expressing both wt-hSecR-GFP_2 and wt-hSecR-YFP or mut-hSecR-GFP_2 and mut-hSecR-YFP to study interaction between receptors. A total of 2 µg plasmids DNA diluted in OptiMEM medium was added to the cells to transfect with single plasmids DNA and 1 µg of plasmids DNA from each plasmid was added to the cells to transfect with double plasmids. A mock or untransfected sample was also prepared to use as a reference for auto-fluorescence.

The cells were imaged using optical micro-spectroscope (OptiMiS) and E_{app} histogram was obtained for individual cell as described in sections 3.4 - 3.6. Of all the cells co-expressing wt-hSecR-GFP_2 and wt-hSecR-YFP or mut-hSecR-GFP_2 and mut-hSecR-YFP, roughly 60% exhibited either a single narrow peak or multiple dominant peaks in the E_{app} histogram while about 40% cells showed either a broad peak or no distinct peak in their E_{app} histograms. The peak positions of the ~ 60% cells showing either single or multiple dominant peaks were collected, binned (bin interval = 0.02), and number of cells *vs.* apparent FRET efficiencies were plotted to generate the *meta-histogram*. Histograms of ~ 40% cells showing single broad peak were not included in the meta-hisotgram.

Based on the various models used to simulate the *meta-histogram* of hSecRs, we found that both wt-, and mut-hSecRs mostly existed as monomers and dimers. Also, the probability of presence of higher order oligomers could not be neglected. The E_{app} peak positions predicted by dimer and free donor model were calculated using equation,

$$E_{app} = \frac{n}{k} E_d, \tag{5.1}$$

where *k* being the number of donor per pixels and *n* takes integral values ranging from 1 to *k* and E_d, the FRET efficiency of a dimer (13). The number of energy donors per pixel which was set as a fitting parameter in a dimer and free donor model was found to be 12 indicating that there could be maximum of 12x2=24 receptors per pixel (including both D- and A-tagged receptors) for both wt- and mut-hSecR. We also estimated the average

number of receptors per pixel using known concentration of GFP_2 protein solution (see Appendix B), which was found to be 58 and 67 for wt- and mut-hSecR, respectively. The disagreement between the number of receptors per pixel obtained from the two methods could be due to the presence of dimers formed by acceptor only fluorophores or presence of higher order oligomers along with dimers and monomers, information of which could not be extracted from the *meta-histogram*. In order to confirm this hypothesis, further experiments with controlled low expression level of receptors are needed to perform. For very low expression level of receptors (close to single complex per pixel), the E_{app} histogram is expected to show distinct peaks (see simulation results described in section 5.1). The presence of mostly single complex per pixel should show a single peak in the *meta-hisotgram* of the dimer-free donor model as described in equation (5.1). Thus, the presence of tetramers or higher order oligomers will show extra peaks in the *meta-histogram* other than the peak predicted for dimer. Hence, a parallel comparison of the number and positions of peaks in the *meta-histograms* for both low and high expression level of receptors can reveal the existence of higher order oligomers.

References:

1. Raicu V, et al. (2009). Determination of supramolecular structure and spatial distribution of protein complexes in living cells. *Nature Photon* 3(2):107-113.

2. Raicu V (2007). Efficiency of resonance energy transfer in homo-oligomeric complexes of proteins. *J Biol Phys* 33(2):109-127.

3. Patowary S, et al. (2013). The muscarinic M3 acetylcholine receptor exists as two differently sized complexes at the plasma membrane. *Biochem J* 452(2):303-312.

4. Rizzo MA, Springer GH, Granada B & Piston DW (2004). An improved cyan fluorescent protein variant useful for FRET. *Nat Biotechnol* 22(4):445-449.

5. Griesbeck O, Baird GS, Campbell RE, Zacharias DA & Tsien RY (2001). Reducing the environmental sensitivity of yellow fluorescent protein. Mechanism and applications. *J Biol Chem* 276(31):29188-29194.

6. Raicu V (2010). FRET-based determination of protein complex structure at nanometer length scale in living cells. Nanoscopy and Multidimensional Optical Fluorescence Microscopy, ed Diaspro A (CRC Press, Boca Raton).

7. Harikumar KG, Ball AM, Sexton PM & Miller LJ (2010). Importance of lipid-exposed residues in transmembrane segment four for family B calcitonin receptor homo-dimerization. *Regul Pept* 164(2-3):113-119.

8. Harikumar KG, Happs RM & Miller LJ (2008). Dimerization in the absence of higher-order oligomerization of the G protein-coupled secretin receptor. *Biochim Biophys Acta* 1778(11):2555-2563.

9. Harikumar KG, Morfis MM, Sexton PM & Miller LJ (2008). Pattern of intra-family hetero-oligomerization involving the G-protein-coupled secretin receptor. *J Mol Neurosci* 36(1-3):279-285.

10. Gao F, et al. (2009). Functional importance of a structurally distinct homodimeric complex of the family B G protein-coupled secretin receptor. *Mol Pharmacol* 76(2):264-274.

11. Harikumar KG, Pinon DI & Miller LJ (2007). Transmembrane segment IV contributes a functionally important interface for oligomerization of the Class II G protein-coupled secretin receptor. *J Biol Chem* 282(42):30363-30372.

12. Siddiqui S, Cong WN, Daimon CM, Martin B & Maudsley S (2013). BRET Biosensor Analysis of Receptor Tyrosine Kinase Functionality. *Front Endocrinol (Lausanne)* 4:46.

13. Raicu V, Singh DR (2013). FRET Spectrometry: A New Tool for the Determination of Protein Quaternary Structure in Living Cells. *Biophys J* 105(9):1937-1945.

Appendix A

A.1. Determination of FRET efficiency from intensity based measurements

In a mixture of donors (D) and acceptors (A), three different types of dimers can form: DD, DA and AA. Donors and acceptors can also remain as monomer. Therefore the emission intensity of donor in presence of acceptors when the donor is excited with an excitation wavelength of λ_{ex} can be expressed as (1):

$$F^{DA}(\lambda_{ex}) = \Gamma^{ex,D}\{[D]Q^{D} + [DD]Q^{D} + [DA]Q^{DA}\} \quad \text{(A.1)}$$

Using equation (3.10) and knowing that excitation rate constant of donor in absence of FRET is independent of FRET i.e., $\Gamma^{ex,D} = \Gamma^{ex,DA}$, above equation can be written as:

$$F^{DA}(\lambda_{ex}) = \Gamma^{ex,D}[D]_{T}Q^{D} - \Gamma^{ex,D}[DA]Q^{D}E \quad \text{(A.2)}$$

Similarly, acceptor intensity can be expressed as:

$$F^{AD}(\lambda_{ex}) = \Gamma^{ex,A}\{[A]Q^{A} + [AA]Q^{A}\} + \Gamma^{ex,AD}[AD]Q^{A} \quad \text{(A.3)}$$

Since probability of acceptor excitation in presence of donor increases because of another pathway to transfer donor excitation energy via dipole-dipole coupling, therefore the rate of excitation of acceptor in presence of FRET can be defined as:

$$\Gamma^{ex,AD} = \Gamma^{ex,A} + \Gamma^{ex,D} E \tag{A.4}$$

Thus using equations (3.10) and (I.4), the acceptor intensity can be written as:

$$F^{AD}(\lambda_{ex}) = \Gamma^{ex,A}[A]_T Q^A + \Gamma^{ex,D}[DA] Q^A E \tag{A.5}$$

where $[D]$, $[A]$, $[DA]$, $[DD]$, and $[AA]$ are concentrations of free donors, acceptors, donors forming dimers with acceptors, donor only, and acceptor only dimers respectively and $[D]_T$ and $[A]_T$ are the total concentrations of donor and acceptors respectively. For a mixture of oligomers of size n with μ_{oligo} as total concentration of oligomers and *k* as the number of donors in oligomer; the total concentrations of donors and acceptors can be expressed as:

$$[D]_T = [D] + \mu_{oligo} n P_D = [D] + \mu_{oligo} \sum_{k=1}^{n} k \binom{n}{k} P_D^k \, P_A^{n-k} \tag{A.6}$$

$$[A]_T = [A] + \mu_{oligo} n P_A = [A] + \mu_{oligo} \sum_{k=0}^{n-1} (n-k) \binom{n}{k} P_D^k \, P_A^{n-k} \tag{A.7}$$

where $P_D = \frac{[D]_D + [D]_A}{[D]_D + [D]_A + [A]_D + [A]_A}$ and $P_A = \frac{[A]_D + [A]_A}{[D]_D + [D]_A + [A]_D + [A]_A}$ are the probabilities of donor and acceptor concentrations respectively in the oligomers while $[D]$, $[D]_A$, and $[D]_D$ are the concentrations of free donors, donors forming complexes with acceptor, and donors only complexes respectively; $[A]$, $[A]_D$, and $[A]_A$ are concentration of free

acceptors, acceptors forming complexes with donors, and acceptors only complexes. Considering similar approach as in equations (A.2) and (A.5) the emission intensities of donor and acceptor for the complex can thus be expressed as:

$$F_n^{DA}(\lambda_{ex}) = \Gamma^{ex,D}\left\{[D]Q^D + \mu_{oligo}\sum_{k=1}^{n}\sum_{q} P_D^k\, P_A^{n-k}\sum_{i=1}^{k} Q_{i,k,n,q}^{DA}\right\} \tag{A.8}$$

$$F_n^{AD}(\lambda_{ex}) = Q^A\left\{\Gamma^{ex,A}[A] + \mu_{oligo}\sum_{k=0}^{n-1}\sum_{q} P_D^k\, P_A^{n-k}\sum_{j=1}^{n-k} \Gamma_{j,k,q}^{ex,AD}\right\} \tag{A.9}$$

Using equation (3.10) with (A.6) and (A.7) above equations can be written as:

$$F_n^{DA}(\lambda_{ex}) = \Gamma^{ex,D}Q^D\left\{[D]_T - \mu_{oligo}\sum_{k=1}^{n-1}\sum_{q}\binom{n}{k} P_D^k\, P_A^{n-k}\sum_{i=1}^{k} E_{i,k,n,q}\right\} \tag{A.10}$$

$$F_n^{AD}(\lambda_{ex}) = Q^A\left\{\Gamma^{ex,A}[A]_T + \Gamma^{ex,D}\mu_{oligo}\sum_{k=1}^{n-1}\sum_{q}\binom{n}{k} P_D^k\, P_A^{n-k}\sum_{i=1}^{k} E_{i,k,n,q}\right\} \tag{A.11}$$

Table A.1: Measured and predicted E_{app} of VCVV for various sets of experiments

Day	1	2	3	4	5	6	7	8	9
Measured E_{app}	0.78	0.69	0.79	0.81	0.78	0.87	0.83	0.81	0.80
Predicted E_{app}	0.74	0.78	0.77	0.79	0.78	0.80	0.78	0.77	0.76

Table A.2: Measured and predicted E_{app} for cytoplasmic tetramers for different expression level

log F^D	ACVA	VCAA	ACAV	VCVV-measured	VCVV-predicted
3.5 - 4.0	0.49 ± 0.02	0.55 ± 0.05	0.35 ± 0.02	0.76 ± 0.05	0.73 ± 0.04
4.0 - 4.2	0.48 ± 0.04	0.58 ± 0.03	0.41 ± 0.04	0.80 ± 0.04	0.75 ± 0.03
4.2 - 4.4	0.52 ± 0.04	0.61 ± 0.02	0.45 ± 0.04	0.81 ± 0.04	0.79 ± 0.03
4.4 - 4.6	0.53 ± 0.04	0.64 ± 0.01	0.47 ± 0.03	0.84 ± 0.03	0.79 ± 0.02
4.6 - 4.8	0.55 ± 0.03	0.66 ± 0.01	0.52 ± 0.03	0.87 ± 0.02	0.81 ± 0.02
4.8 – 5.5	0.60 ± 0.02	0.69 ± 0.00	0.55 ± 0.00	0.91 ± 0.00	0.83 ± 0.01

A.2. Investigation of excess in FRET efficiencies of VCVV with expression level

The difference in measured and predicted Eapp (ΔE_{app}) of VCVV for range of expression level as shown in Table A.2 is listed in Table A.3. The error for ΔE_{app} is calculated using following equation:

$$Error = \Delta E_1 + \Delta E_2 \tag{A.12}$$

where $\Delta E_1$and ΔE_2 are errors for measured E_{app} and predicted E_{app} of VCVV respectively.

Table A.3: ΔE_{app} of VCVV and their errors for different expression level

$\log F^D$	ΔE_{app}	Error
3.5 - 4.0	0.03	0.09
4.0 - 4.2	0.05	0.07
4.2 - 4.4	0.03	0.07
4.4 - 4.6	0.05	0.05
4.6 - 4.8	0.06	0.04
4.8 – 5.5	0.07	0.01

Appendix B

B.1 Estimation of receptors concentration:

To calculate the number of receptors per pixel of hSecRs, we used the known concentrations of GFP_2 protein solution that was obtained as a generous gift from Lucigen Corporation, WI, USA. The GFP_2 stock solution at concentration of 137 µM were diluted in deionized water to prepare seven different concentrations: 100, 50, 75, 25, 10, 5 and 2.5 µM. A 30µL of each solution was taken in a Petri dish with 0.13 mm glass bottom coverslip for imaging. The fluorescence intensities of GFP_2 solution at a particular concentration was calculated by integrating the measured emission spectrum for that concentration. Fig. (B.1) shows fluorescence intensity *vs.* concentration graph of the GFP_2 protein solution where closed circles and solid line are the data points and their linear fitting respectively. As described in section 4.2.2.8, fluorescence of the donor in absence of acceptor (F^D) for hSecR can be calculated using the k^{DA} and k^{AD} values determined from spectral unmixing. We calculated the average F^D value per pixel for each cell used in the *meta-histogram* both for wt- and mut-hSecRs. Under the same experimental conditions for GFP_2 solution that was used for wt-, and mut-hSecR, equation (4.1) becomes:

$$C_x = C_s \frac{F^x}{F^s}, \tag{B.1}$$

where '*x*' and '*s*'stands for hSecRs and GFP_2 solution respectively. Thus, using any point on the straight ling in Fig. B.1 for known concentration (C_s) and fluorescence intensity

(F^S) along with the calculated values of average F^D value per pixel and size of a pixel (2), the average number of receptors expressed per pixels can be calculated.

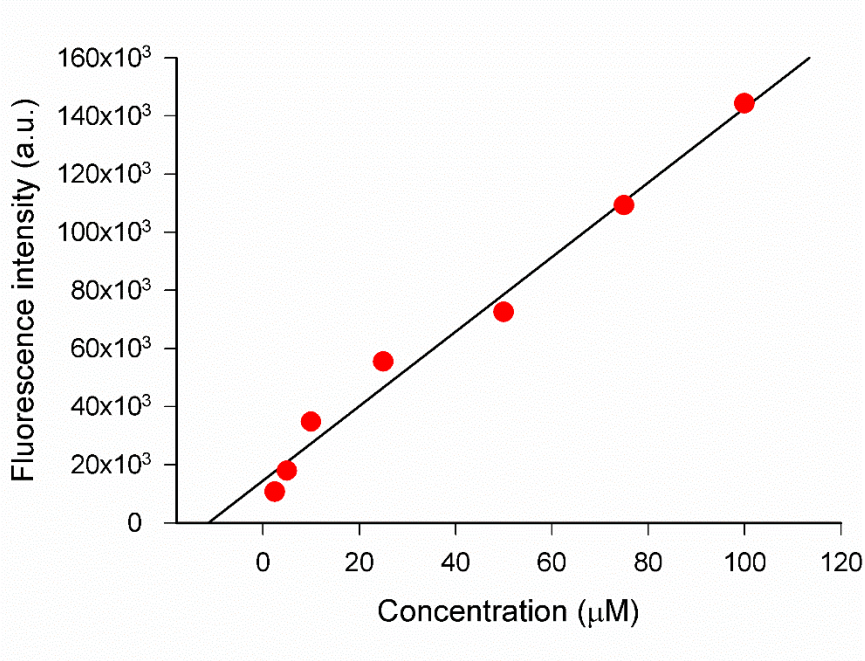

Figure B.1: Intensity *vs.* concentration graph of GFP_2 protein solution. Closed circles are the experimental data point and solid line is the linear fitting of the experimental data point.

Referrences:

1. Raicu V (2007). Efficiency of resonance energy transfer in homo-oligomeric complexes of proteins. *J Biol Phys* 33(2):109-127.

2. Biener G, et al. (2013). Development and experimental testing of an optical microscopic technique incorporating true line-scan excitation. *Int J Mol Sci (under review)*.

Curriculum Vitae

Suparna Patowary
E-mail: Patowary@uwm.edu, monankita@gmail.com

Formal Education

- Sep 2008 – Dec 2013: PhD, Department of Physics, University of Wisconsin Milwaukee.
  Dissertation title: Protein Association in Living Cells Using FRET Spectrometry: Application to G-Protein Coupled Receptors

- July 2004 – May 2006: M.S, Physics, Indian Institute of Technology (IIT), Guwahati, India

- July 2001 – Dec 2004: B.S, Physics, Cotton College, Guwahati, India

Academic Awards and Achievements

- David Lichtman Memorial Scholarship for *outstanding performance in experimental physics*: Physics Department, University of Wisconsin, Milwaukee (July 2013)

- Graduate Student Travel Award: Graduate School, University of Wisconsin, Milwaukee (multiple times during 2010-2013)

- Chancellor's Graduate Student Award: Graduate School, University of Wisconsin, Milwaukee (multiple times during 2008-2013)

- Departmental Travel Award: Physics Department, University of Wisconsin, Milwaukee (April, 2013)

- Diploma in Radiological Physics (DIRP): All-India second rank (conducted by Bhaba Atomic Research Center, Mumbai, India)

Research Experience

- 2010-2012: Experimental verification of Förster theory of resonance energy transfer for multimeric complexes using optical micro-spectroscopy (OptiMiS); under Prof. Valericã Raicu, Physics department, UWM, USA

- 2011-2013: Quaternary structure determination of G-Protein coupled receptors (GPCRs) using spectrally resolved Förster resonance energy transfer method and Monte-Carlo simulations; under Prof. Valericã Raicu, Physics Department, UWM, USA

- 2005-2006: Solar Neutrino Problem; under Dr. Poulose Poulose, Associate Professor, IITG, India

Teaching Experience

- Fall 2008-Summer 2009, Spring 2010: Physics 108 (Laboratory for Physics in Everyday Life), Physics Department, UWM

- Fall 2009: Physics 121 (General Physics Laboratory), Physics Department, UWM

Publications

Journals

1. **S Patowary**, L F Pisterzi, J D Holz, J A Oliver, J W Wells and V Raicu. Experimental verification of Förster Resonance Energy Transfer (FRET) theory using optical micro-spectroscopy (OptiMiS) and fluorescence reference standards, (under preparation)

2. **S Patowary**, E Alvarez-Curto, T R Xu, J D Holz, J A Oliver, G Milligan and V Raicu. The muscarinic M_3 acetylcholine receptor exists as two differently sized complexes at the plasma membrane, *Biochem. J.* 452 (2013) 303–312

3. D R Singh, M M Mohammad, **S Patowary**, M R Stoneman, J A Oliver, L Movileanu and V Raicu. Determination of the quaternary structure of a bacterial ATP-binding cassette (ABC) transporter in living cells, *Integr. Biol.* 5 (2013) 312-323

4. M R Stoneman, **S Patowary**, D R Singh, L Komarova, L G Westrick, J A Oliver, and V Raicu. Quantifying the efficiency of various FRET constructs using OptiMiS™. *BioTechniques* 52 (2012) 191–195

5. M R Stoneman**, S Patowary**, M T Roesch, D R Singh, V Strogolov, J A Oliver, V Raicu. Determination of the Stoichiometry, structure, and distribution in living cells of protein complexes from analysis of single-molecular complexes, *Multiphoton Microscopy in the Biomedical Sciences X, Proceedings of SPIE*, 7569 (2010), 756913-1 – 756913-8

Contributed Conference Presentations

1. **S Patowary**, E Alvarez-Curto, T R Xu, J D Holz, J A Oliver, G Milligan and V Raicu**.** Probing the stoichiometry and geometry of M3 acetylcholine receptors at the plasma membrane, poster presentation at *Biophysical Society Annual Meeting, 2013,* Philadelphia, PA, USA

2. **S Patowary**, E Alvarez-Curto, J A Oliver, G Milligan and V Raicu. Quaternary structure determination of the M3 muscarinic acetylcholine receptors based on spectral-FRET, poster presentation at *Biophysical Society Annual Meeting, 2012,* San diego, CA, USA

3. **S Patowary**, L F Pisterzi, M R Stoneman, V Strogolov, J A Oliver, J W Wells and v Raicu. Accurate FRET measurements and testing of the theory for multimeric complexes using reference fluorescence standards, poster presentation at *Biophysical Society Annual Meeting*, 2011, Baltimore, MD, USA

4. **S Patowary**, L F Pisterzi, M R Stoneman, V Strogolov, J A Oliver, J W Wells and V Raicu. Experimental testing of the FRET theory for multimeric complexes using reference fluorescence standards, poster presentation at *FRET at 65-One Day Symposium*, University of Virginia, Charlottesville, VA, 2011

5. M R Stoneman, **S Patowary**, M Roesch, M Dey and V Raicu. In vivo monitoring of agonist-induced relative movements between G-protein coupled receptor segments in oligomeric complexes using spectrally resolved FRET. poster presentation at *Biophysical Society Annual Meeting,* 2011, Baltimore, MD, USA